
**A 1 km sea-ice concentration dataset from merged thermal
infrared and microwave radiometer satellite observations:
More than the sum of its parts**

Vom Fachbereich für Physik und Elektrotechnik
der Universität Bremen

zur Erlangung des akademischen Grades eines
Doktors der Naturwissenschaften (Dr. rer. nat.)
vorgelegte Dissertation

von
M. Sc.
Valentin Simon Ludwig

Verteidigung der Dissertation

16. Dezember 2020

1. Gutachter: Dr. Gunnar Spreen
2. Gutachter: Dr. Leif Toudal Pedersen

Abstract

We present a merged sea-ice concentration dataset at 1 km resolution which combines the benefits of thermal infrared and passive microwave radiometer sea-ice concentration retrievals. The merged dataset is superior to the thermal infrared sea-ice concentration derived from Moderate Resolution Imaging Spectroradiometer (MODIS) measurements in that it is spatially continuous and has no bias towards a well-established passive microwave sea-ice concentration dataset, namely the ARTIST Sea Ice (ASI) 89 GHz sea-ice concentration. At the same time, it outperforms ASI sea-ice concentration at 5 km resolution due to its finer spatial resolution of 1 km and an enhanced potential for lead retrieval.

We extend a previously published thermal-infrared based MODIS sea-ice concentration algorithm by better spatial coverage and a smoother ice tie-point field which removes physically implausible sharp gradients. The root mean square deviation (RMSD) between sea-ice concentration derived by the old and the new version for 997 MODIS granules is 2–4 % between February and mid May 2019 and goes up to 14 % by the end of May. An ice tie-point of 266.5 K is derived as upper limit for meaningful sea-ice concentration retrieval. The MODIS sea-ice concentration is merged with ASI sea-ice concentration on swath level by tuning it to preserve the ASI mean on a scale of 5 km, while keeping the fine spatial resolution of 1 km of the MODIS data. Cloudy pixels are set to the ASI sea-ice concentration.

The merged, MODIS and ASI sea-ice concentration is evaluated against a reference dataset derived from 66 Sentinel-2 reflectance scenes at 10 m resolution between February and May 2019. The mean of all merged, MODIS and reference sea-ice concentration scenes is 93.1 %, 92.8 % and 94.4 %, respectively. The RMSDs between the datasets are 5.0 % (merged vs. MODIS), 4.9 % (merged vs. reference) and 3.8 % (MODIS vs. reference).

The benefit of the finer resolution for lead retrieval is demonstrated by calculating the open-water extent (area covered by at least 15 % of water), which is expected to be higher for more finely resolved data. In an example scene, it is 771 km² for the merged dataset and thus much closer to the reference data (878 km²) than the ASI open-water extent (182 km²). In a case where an unscreened cloud and high ice-surface temperatures deteriorate the MODIS sea-ice concentration, the merging reduces the RMSD with respect to the reference data from 23.5 % (MODIS vs. reference) to 9.3 % (merged vs. reference).

The advantage of the merged dataset over the single-sensor datasets is further demonstrated by monitoring a polynya which opened north of Greenland in February 2018, at an untypical time and region. During the opening phase, the fine spatial resolution yields an open-water extent of the merged data which is up to 60 % higher than that of the ASI data, indicative of the newly forming leads. The advantage of the finer resolution is most pronounced during the opening and closing of the polynya. Additionally, the merged dataset allows continuous monitoring of the event, which is not possible with MODIS data.

Contents

Abstract	i
1. Introduction	1
2. Theory of Sea-Ice Remote Sensing	7
2.1. Remote sensing	7
2.2. Sea ice	12
3. Data	21
3.1. Input data for merged dataset	21
3.2. Reflectance data for reference sea-ice concentration	25
3.3. Other sea-ice concentration data	26
3.4. Sentinel-1 mosaics and reanalysis data	29
3.5. Sea-ice thickness data	30
4. Methods	33
4.1. MODIS sea-ice concentration	33
4.2. Merged sea-ice concentration	36
4.3. Uncertainty estimates	39
4.4. Evaluation	41
5. MODIS sea-ice concentration	45
5.1. Improvement of ice tie-point retrieval	45
5.2. Cloud mask	49
5.3. Tie-point variability	51
5.4. Ice tie-point threshold	55
5.5. Comparison to ASI SIC	58
5.6. Discussion	60
6. Merged sea-ice concentration	63
6.1. Introduction of the datasets	63
6.2. Benefits of merged dataset	72
6.3. Limitations of merged dataset	79
6.4. Uncertainty estimates	86
6.5. Discussion	89

7. Case study: The 2018 North Greenland Polynya	93
7.1. Temporal evolution	93
7.2. Intercomparison of sea-ice concentration datasets	97
7.3. Environmental conditions	101
7.4. Processes	107
7.5. Discussion	109
8. Summary & Conclusions	115
9. Outlook	123
A. Appendix	125
List of acronyms	125

1. Introduction

Until the 20th century, little has been known about the Arctic to European scientists due to its remoteness and hostility. First cartographic expeditions took place in the 16th century (Lainema and Nurminen, 2009). While those and later endeavours like Sir John Franklin's fatally ended Northwest Passage expedition in 1845 and Fridtjof Nansen's pioneering Fram expedition in 1893-1896 (Nansen, 1902) are the first accounts of European Arctic research, our current knowledge of the processes in the Arctic has greatly advanced since the start of the satellite era. The first space-borne image of sea ice was taken as early as 1960 (Shokr and Kaleschke, 2012). Since 1972, visible and thermal infrared imagery is available continuously from the Landsat satellites. Passive microwave measurements were first taken in 1971 and are available continuously since 1978 (see Fig. 1.2). Since the first awareness-raising summer sea-ice extent minimum in 2007, the Arctic has come to public attention as one of the hot-spots of anthropogenic climate change. The sea-ice extent has been declining steadily, reaching its all-time low in 2012 and the second lowest minimum in 2020. The long-term declining trend is visualised in Fig. 1.1.

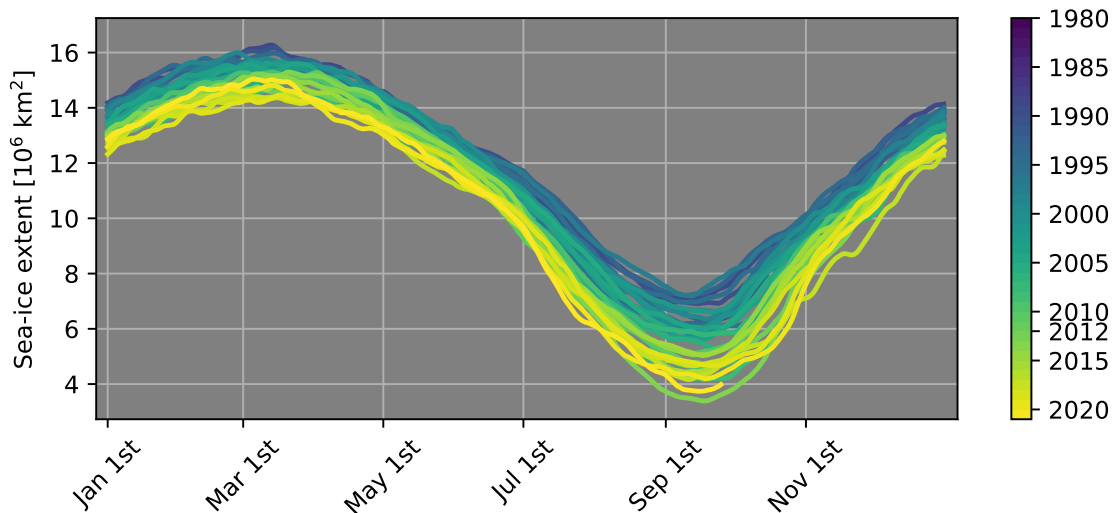


Figure 1.1.: Sea-ice extent timeseries between 1979 and 2020, ending on September 24, 2020. Based on the NSIDC Climate Data Record (Cavalieri et al., 1996) until 2019 and the NSIDC Near-Real-Time sea-ice concentration (Maslanik and Stroeve, 1999) for 2020.

The retreating sea ice changes the local fauna (Kovacs et al., 2011; Pongracz et al., 2017; Campana et al., 2020), increases biological activity (Assmy et al., 2017), makes the Arctic sea ways more accessible (Melia et al., 2016; Chen et al., 2020) and releases heat and moisture to the atmosphere (Boisvert and Stroeve, 2015; Danielson et al., 2020). These changes have immediate and significant consequences for the Arctic climate system itself, but what happens in the Arctic does not stay in the Arctic. It warms faster than the mid-latitudes, a process which has become known as Arctic Amplification. The exact mechanisms are subject to debate, but observational studies largely agree that Arctic Amplification changes mid-latitude weather patterns and some argue that it increases the frequency of extreme events (Cohen et al., 2014; Coumou et al., 2018; Vavrus, 2018; Cohen et al., 2019).

The Arctic Amplification is in part driven by the retreating sea ice (Dai et al., 2019). The large-scale, continuous monitoring of this retreat is possible since 1978 via space-borne radiometers which measure electromagnetic radiation emitted by the Earth at microwave frequencies between 22 GHz and 37 GHz. Since 1987, measurements at higher frequencies (85, 89 and 91 GHz) are available and since 2001, the 6.9 and 10.6 GHz frequencies are covered. A temporal overview of a selection of radiometers is given in Fig. 1.2. The passive microwave radiometer used in this study is the Advanced Microwave Scanning Radiometer 2 (AMSR2).

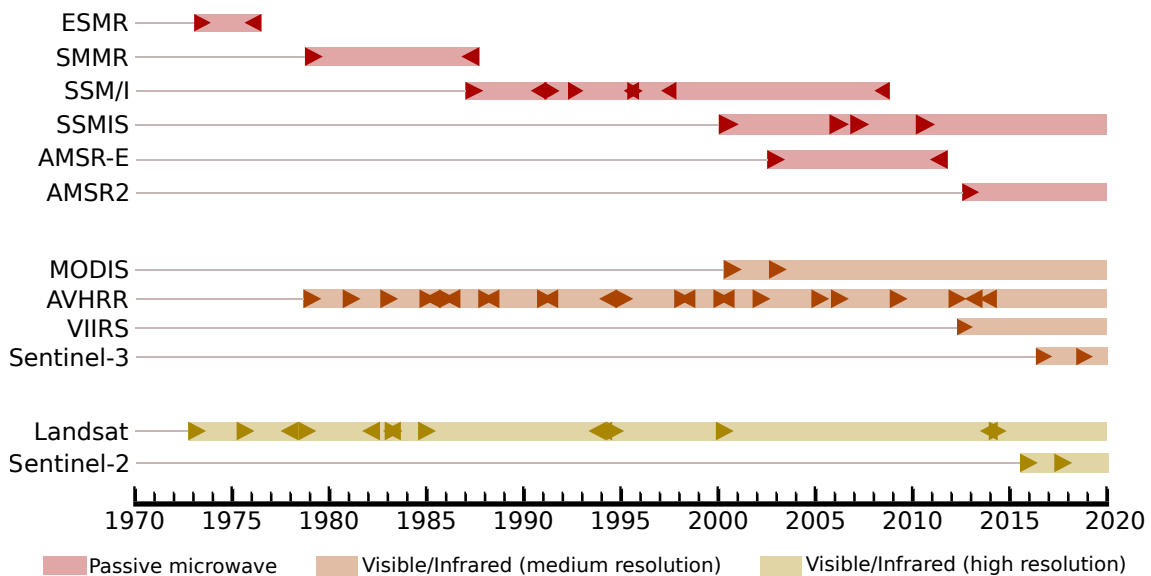


Figure 1.2.: Timeline of passive microwave and visible/infrared radiometers. Triangles pointing right and left denote the start and stop of the radiometer’s lifetime, respectively. Note that most radiometers were launched on several satellites, indicated by multiple triangles in one row. The radiometers aboard Landsat, Sentinel-2 and Sentinel-3 are referred to by the satellites’ names. „Medium resolution“ means resolutions between 250 m and 4 km, „high resolution“ means resolutions between 10 m and 100 m. This Figure shows a selection of radiometers which are of relevance for this study.

1. Introduction

An important sea-ice parameter which directly impacts most of the above-mentioned changes is the surface fraction of sea ice in a given area, the sea-ice concentration. „Given area“ mostly means one grid cell/pixel or one satellite footprint. The sea-ice concentration can be retrieved from passive microwave data by deriving reference surface signatures (tie-points) for pixels which are covered only by ice and for pixels which are covered only by water and then interpolating linearly for values between the tie-points. The early algorithms like Bootstrap (Comiso, 1986, 1995) and NASA Team (Cavalieri et al., 1984) use the gradient ratio (difference between two frequency channels, divided by their sum) or the polarisation ratio (difference between vertical and horizontal polarisation of the same channel, divided by their sum) of the 18, 23 and 37 GHz frequencies. Hybrid algorithms like OSI SAF (Lavergne et al., 2019) or SICCI (Ivanova et al., 2015) use weighted averages of other algorithms with the weight depending on the sea-ice concentration magnitude. At these frequencies, the atmosphere is virtually transparent, so that data can be retrieved almost independently of the weather conditions. This makes these algorithms the backbone of the sea-ice extent climatologies, one of which is shown in Figure 1.1. A downside, however, is their comparably coarse spatial resolution. The resolutions in the instantaneous field of view range from 50 km at 19 GHz to 25 km at 37 GHz for the Special Sensor Microwave Imager (SSM/I) radiometer.

Finer resolutions down to 5 km are possible using the 89 GHz channels of the Advanced Microwave Scanning Radiometer for Earth Observation (AMSR-E) and AMSR2 instruments, but weather filters or atmospheric correction need to be employed due to the atmospheric contribution by water vapour and liquid water path (Spreen et al., 2008; Lu et al., 2018). In this thesis, the Arctic Radiation and Turbulence Study Sea Ice (ASI) algorithm applied to AMSR2 measurements as presented by Spreen et al. (2008) is used. It was introduced for SSM/I data by Kaleschke et al. (2001) and applied to AMSR-E by Spreen et al. (2008). ASI uses a third-degree polynomial to obtain the sea-ice concentration from the difference between horizontal and vertical polarisation at 89 GHz. It is often used on a 6.25 km or a 3.125 km grid. Beitsch et al. (2014) show the benefits of interpolating the ASI sea-ice concentration onto a 3.125 km grid during a fracture event in the Beaufort Sea 2013.

Such fracture events cause leads, linear cracks in the ice. Although only covering 1–2% of the central Arctic in winter, they are responsible for more than 70% of the upward heat flux (Marcq and Weiss, 2012). Leads can be observed by the passive microwave algorithms described above as reduced sea-ice concentration, but only at a comparably coarse resolution and if the ice which grows in them is thinner than approximately 10 cm and not covered by fresh snow (Shokr and Kaleschke, 2012; Heygster et al., 2014).

Leads are more readily retrieved by switching from passive microwave to thermal infrared observations. An overview about medium- and high-resolution radiometers operating between the visible and infrared spectrum (400 nm–14 μ m) is given in Fig. 1.2. In this thesis, ice-surface temperatures retrieved from Moderate Resolution Imaging Spectroradiometer (MODIS) data are used. The large temperature contrast between the warm lead

and the cold ice surface and the fine resolutions of down to 750–1000 m make the thermal infrared spectrum well-suited for lead retrieval. Willmes and Heinemann (2015) assume that leads are represented by the high end of the ice-surface temperature anomaly histogram and employ different thresholds for the lead retrieval. The inverse of the lead area fraction in a certain area can be interpreted as sea-ice concentration, assuming that open water only occurs in leads. This assumption is reasonable in the Central Arctic, away from the ice edge and in the absence of polynyas (non-linearly shaped openings in the ice (World Meteorological Organisation, 1970)). Another approach for sea-ice concentration retrieval from ice-surface temperatures is presented by Lindsay and Rothrock (1995) and Drüe and Heinemann (2004). They introduce the concept of „potential open water“. Potential open water is the fraction of water which would need to be present in a grid cell in order to yield the ice-surface temperature measured by the radiometer, assuming that the pixel only contains open water and ice which is thick enough to prevent oceanic heat flux. Its inverse is the sea-ice concentration. Here, the water tie-point is the freezing point of sea water and the ice tie-point is derived from the local ice-surface temperature anomaly. This allows sea-ice concentration retrieval at 1 km resolution, however the true sea-ice concentration is underestimated if more than one ice-thickness class is present in the region used for the tie-point retrieval. Furthermore, the surface is obscured by clouds in the thermal infrared spectrum, so that the sea-ice concentration field is not continuous. In summary, sea-ice concentration can be retrieved from passive microwave data at the correct magnitude and independently of cloud coverage, but is limited to spatial resolutions of 5 km and coarser. Thermal infrared sea-ice concentration, on the other hand, has finer spatial resolutions and an enhanced potential for lead retrieval, but is limited to cloud-free scenes and is more susceptible to ice thickness, often leading to an underestimation of the true sea-ice concentration.

In this thesis, the best of the two products is used to create a merged sea-ice concentration dataset. The merged sea-ice concentration combines the fine spatial resolution of the thermal infrared MODIS sea-ice concentration with the continuous coverage and more correct magnitude of the passive microwave sea-ice concentration. An example in which the merged sea-ice concentration is compared to passive microwave sea-ice concentration data with coarser resolution and a fine-resolution Synthetic Aperture Radar (SAR) image for reference is shown in Fig 1.3.

1. Introduction

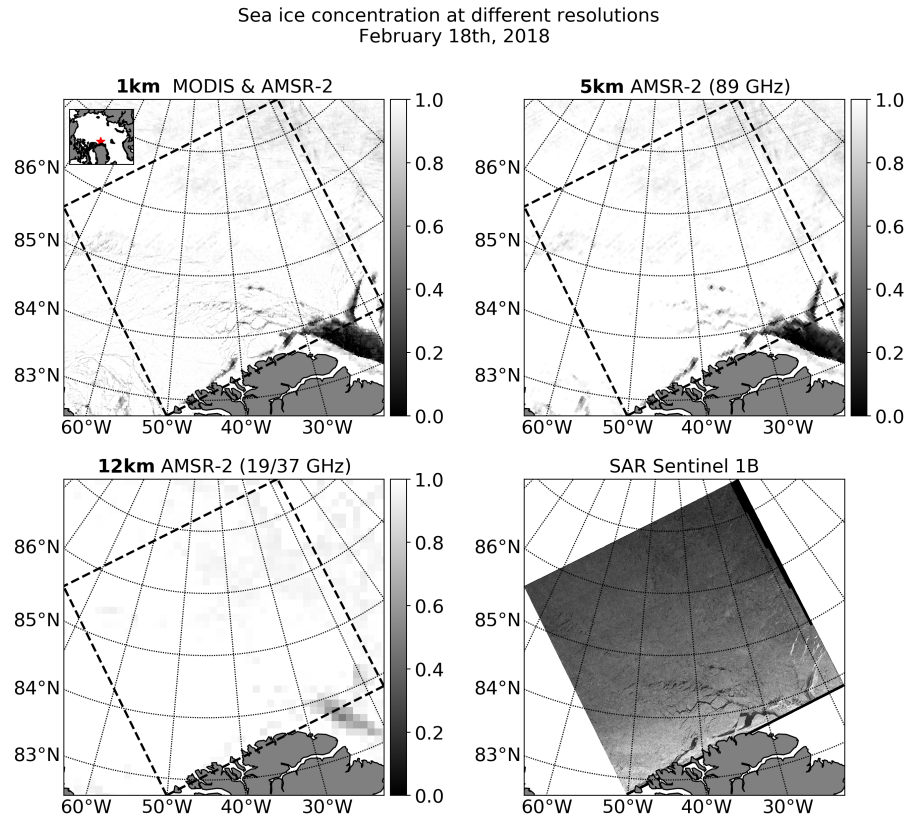


Figure 1.3.: Sea-ice concentration during February 2018, when a large area of water opened north of Greenland (Ludwig et al., 2019). The upper left shows the product presented in this thesis. The upper right and lower left show coarser-resolution passive microwave algorithms. The lower right shows a Sentinel-1B radar image, where sea ice appears bright and open water appears dark. The inset in the upper left shows the location of the scene. This is a slightly modified version of a Figure published as Ludwig and Spreen (2018).

The following aims are formulated:

1. Implement and improve the MODIS sea-ice concentration retrieval of Drüe and Heinemann (2004)
2. Develop and implement a procedure to merge MODIS and ASI sea-ice concentration
3. Evaluate the merged, MODIS and ASI sea-ice concentration against independently derived reference sea-ice concentration
4. Derive uncertainty estimates for the merged and MODIS sea-ice concentration
5. Apply the merged sea-ice concentration dataset in a case study

This thesis is structured as follows: The necessary principles of remote sensing and sea-ice physics are introduced in chapter 2. Subsequently, chapter 3 presents the data which are used. The methods employed for the improved MODIS SIC retrieval, the merging procedure, the uncertainty formulation and the implementation of the operational merged sea-ice concentration processing chain are described in chapter 4. Chapter 5 is dedicated to the improved MODIS sea-ice concentration. Furthermore, an ice-surface temperature threshold is derived above which meaningful sea-ice concentration cannot be derived anymore. The next step, and the core of this thesis, is the merging of the MODIS sea-ice concentration with the ASI sea-ice concentration. The results are the topic of chapter 6, which compares the merged, MODIS, and ASI sea-ice concentration to independently derived reference sea-ice concentration datasets. Also, uncertainty estimates for the merged, MODIS, and ASI sea-ice concentration are presented. Parts of chapter 5 and chapter 6 are published in Ludwig et al. (2020). In the last Results chapter, chapter 7, the merged sea-ice concentration dataset is applied to monitor the formation of a polynya which opened in February 2018 north of Greenland. Furthermore, the drivers and consequences of the polynya are analysed. This chapter is published in Ludwig et al. (2019). Each of the Results chapters contains a discussion of the findings, comprising the implication of the findings and placing them into the context of literature. The most important steps and the conclusions are presented in chapter 8. Finally, chapter 9 gives directions for further research.

The single parts of this thesis will be referred to as chapters (chapter x), sections (section x.x), subsections (subsection x.x.x) and paragraphs (bold heading, without numbering).

2. Theory of Sea-Ice Remote Sensing

This chapter provides the theoretical background of the work which is presented in this dissertation. The first part, section 2.1, describes the fundamentals of remote sensing. The second part, section 2.2, describes the growth of sea ice, as well as the physical processes and parameters which influence the signal acquired by remote sensing.

2.1. Remote sensing

Remote sensing is the science of investigating an object without being in physical contact with it. In Earth science, it is commonly used for surveying larger regions in comparably short time. Remote sensing measurements are acquired either actively or passively. For passive measurements, the radiometer measures radiation emitted by the object of interest. For active measurements, radiation is emitted by the instrument itself and the reflected and/or scattered radiation is measured.

Remote sensing measurements are acquired from air-borne platforms, such as airplanes or helicopters or from space-borne platforms, namely satellites. Most satellites operate at altitudes between 700 and 900 km (polar-orbiting satellites) or at 35,786 km (geostationary satellites). The data used in this thesis are acquired by polar-orbiting satellites. Airborne measurements are only used for the sea-ice thickness retrieval described in subsection 3.5.4, their acquisition is described there. Geostationary satellites are less often used for sea-ice remote sensing because the large zenith angles degrade the effective spatial resolution, which makes them unsuitable for latitudes north of approximately 70 °N (Jin et al., 2020). Their high temporal resolution, however, is an advantage as it allows almost real-time sea-ice tracking with measurement intervals between 10 and 30 minutes (Jin et al., 2020; Temimi et al., 2011).

On board the satellites, radiometers measure electromagnetic radiation emitted or reflected by the object of interest. This section deals with the theory of electromagnetic radiation and its transfer from the Earth's surface through the atmosphere to the radiometer. The subsections 2.1.1 and 2.1.2 follow the description in Ulaby et al. (2014), where an extensive overview over passive and active microwave systems is given. Subsection 2.1.3 follows Shokr and Sinha (2015).

2.1.1. Black-body radiation

A black-body is an idealised body which perfectly absorbs and emits electromagnetic radiation. Its spectral brightness, B_λ , is given by Planck's radiation law as

$$B_\lambda = \frac{2hc^2}{\lambda^5} \left(\frac{1}{e^{hc/\lambda kT} - 1} \right), \quad (2.1)$$

where B_λ is in $\text{Wm}^{-2}\text{sr}^{-1}\text{Hz}^{-1}$, h is Planck's constant in Js, c is the vacuum velocity of light in ms^{-1} , λ is the wavelength in m, k is Boltzmann's constant in JK^{-1} and T is the black-body temperature in K. The values of the natural constants are given in the appendix. Equation 2.1 gives the spectral brightness for one distinct wavelength λ and one distinct temperature T . The total brightness of a black-body can be derived by integrating equation 2.1 over all wavelengths according to

$$B = \int_0^\infty B_\lambda d\lambda = 2hc^2 \int_0^\infty \left(\frac{1}{\lambda^5(e^{hc/\lambda kT} - 1)} \right) d\lambda. \quad (2.2)$$

Solving this integral yields the Stefan-Boltzmann law, which gives the black-body's brightness as function of its temperature:

$$B = \sigma T^4, \quad (2.3)$$

where B is given in Wm^{-2} and σ is the Stefan-Boltzmann constant in $\text{Wm}^{-2}\text{K}^{-4}$. For each temperature, the maximal radiation is emitted at a different wavelength λ_{max} . Warmer bodies have their radiation maxima at shorter wavelengths. The exact dependence is given by Wien's displacement law:

$$\lambda_{max} = \frac{2.879 \times 10^{-3}}{T}. \quad (2.4)$$

For many remote sensing applications, Planck's radiation law does not need to be considered in its full complexity, but can be approximated. The two approximations of Planck's law which are relevant for this thesis are the Wien radiation law and the Rayleigh-Jeans approximation. The Wien radiation law holds for small wavelengths/high frequencies where the assumption $hc/\lambda kT \gg 1$ is valid. This reduces Planck's radiation law (equation 2.1) to

$$B_\lambda = \frac{2hc^2}{\lambda^5} e^{-hc/\lambda kT}. \quad (2.5)$$

For a body at a physical temperature of 250 K, Wien's radiation law deviates from Planck's radiation law by less than 1% for wavelengths of 12.5 μm and shorter. On the long-wavelength/low-frequency end of the spectrum, the approximation $hc/\lambda kT \ll 1$ simplifies equation 2.1 to

$$B_\lambda = \frac{2ckT}{\lambda^4}, \quad (2.6)$$

where B_λ is the spectral black-body brightness. This simplification is known as Rayleigh-Jeans law or Rayleigh-Jeans approximation. Planck's law along with the two approximations is shown in Figure 2.1. Assuming a body with the same physical temperature as above, 250 K, the Rayleigh-Jeans approximation deviates from Planck's radiation law by less than 1% for frequencies below about 100 GHz. It is apparent from Figure 2.1 that the channels used for passive microwave sea-ice concentration algorithms are within the regime of the Rayleigh-Jeans law. The thermal infrared channels used for the ice-surface temperature retrieval are within the regime of Wien's radiation law.

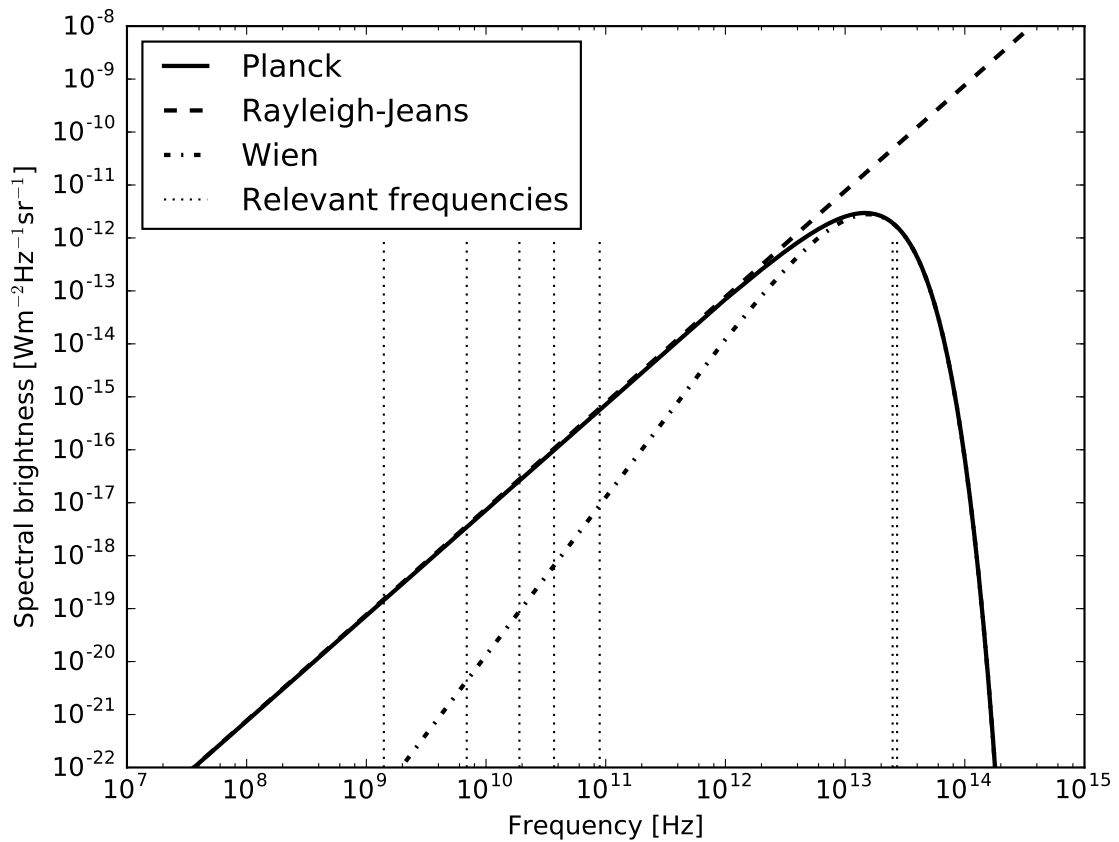


Figure 2.1.: Planck's radiation law (solid) with the Rayleigh-Jeans law (dashed) and Wien's radiation law (dash-dotted) for a body at a physical temperature of 250 K. The faint dotted lines indicate the frequencies which are relevant for the sea-ice concentration retrieval in the microwave spectrum (1.4, 6.9, 19, 37 and 89 GHz) and the ice-surface temperature retrieval in the thermal infrared spectrum (24.9 THz or 11.0 μm and 27.2 THz or 12.0 μm).

2.1.2. Grey-body radiation

The black-body concept is convenient for developing the theory described in subsection 2.1.1, but it is an idealised concept and blackbodies do not occur in nature. Real bodies are normally referred to as grey bodies. They emit and absorb less radiation than a

black-body would. If we consider the brightness of a black-body, B_{bb} , using the Rayleigh-Jeans approximation in equation 2.6, we can define a possibly direction-dependent grey-body brightness

$$B_{gb}(\theta, \phi) = \frac{2ck}{\lambda^4} T_b(\theta, \phi) \Delta\lambda, \quad (2.7)$$

where the zenith angle θ and the azimuthal angle ϕ denote the angular direction dependence and $\Delta\lambda$ is a narrow wavelength interval. The quantity $T_b(\theta, \phi)$ is called brightness temperature. It is the radiometric temperature of the grey body and equivalent to the physical temperature which a black body would need to have to emit/absorb the same amount of radiation as the grey body. The ratio of the grey-body brightness temperature and the corresponding black-body physical temperature is called emissivity ϵ :

$$\epsilon(\theta, \phi) = \frac{B_{gb}(\theta, \phi)}{B_{bb}} = \frac{T_b(\theta, \phi)}{T}, \quad (2.8)$$

where T is the grey body's physical temperature in K and the emissivity is dimensionless. A blackbody's physical and radiometric temperature are identical since a blackbody's emissivity is 1 by definition. A grey body will always have an emissivity smaller than 1.

2.1.3. Radiative transfer

So far, we have discussed the fundamentals of electromagnetic radiation, but neglected the transfer of radiation from the Earth's surface to the satellite. The atmosphere interacts with the signal by absorption, scattering and emission.

The brightness temperature T_b measured by a downward-looking space-borne radiometer comprises the surface signal, the up- and downwelling atmospheric radiation and the galactic contribution from free space. The contributions are represented by the first, second, third and fourth term in the radiative transfer equation

$$T_b = \epsilon_s T_s e^{-\tau} + T_a(1 - e^{-\tau}) + T_a(1 - \epsilon_s)(1 - e^{-\tau})e^{-\tau} + T_{sp}(1 - \epsilon_s)e^{-2\tau}, \quad (2.9)$$

respectively. Here, ϵ_s and T_s are the surface emissivity and physical temperature integrated over the emitting layer of the ground, respectively, τ is the atmospheric opacity and T_a is the effective physical temperature of the emitting layer of the atmosphere. This is a simplified form of a radiative transfer equation, assuming constant temperature and atmospheric attenuation profiles. Another simplification is to neglect the galactic contribution (fourth term in equation 2.9). In this term, T_{sp} is the reflected space radiation. It is given as 2.7 K by Shokr and Sinha (2015), which makes the galactic contribution negligibly small compared to the magnitude of the other three contributions. In the third term, we assume that the part of the downwelling atmospheric radiation which is not absorbed is reflected. Kirchhoff's law states that the absorptivity equals the emissivity, so that the sum of emissivity and reflectivity is 1 and we can express the reflectivity by

$1 - \epsilon_s$. The first two quantities on the right-hand side of equation 2.9, $\epsilon_s T_s$, are the surface signal which we use to infer the sea-ice concentration. The other terms, $e^{-\tau}$ in the first term and the complete second and third term, represent the atmospheric contribution which, for our purposes, contaminates the surface signal and needs to be corrected for. Atmospheric correction is more important in the thermal infrared spectrum than in the microwave spectrum, but cannot be neglected completely in the latter.

Microwave spectrum

Higher microwave frequencies like the 89 GHz frequency used in this study are affected by volume scattering, e. g. by cloud water droplets or rain as their diameter is comparable to the wavelength of approximately $3 \mu\text{m}$. The two gases with significant absorption bands in the microwave spectrum are oxygen at 50-70 GHz and at 118.75 GHz and water vapour at 22.235 GHz and 183.31 GHz. The frequency channels for microwave sea-ice concentration (SIC) retrieval algorithms are typically chosen such that the atmospheric absorption is small. However, as Fig. 2.2 shows, the continuum absorption of water vapour at the 89 GHz frequency used in this study is significant and even stronger than in the 22.235 GHz absorption band. This renders the need for atmospheric correction as proposed by Lu et al. (2018) or weather filters over open ocean as employed by Spreen et al. (2008).

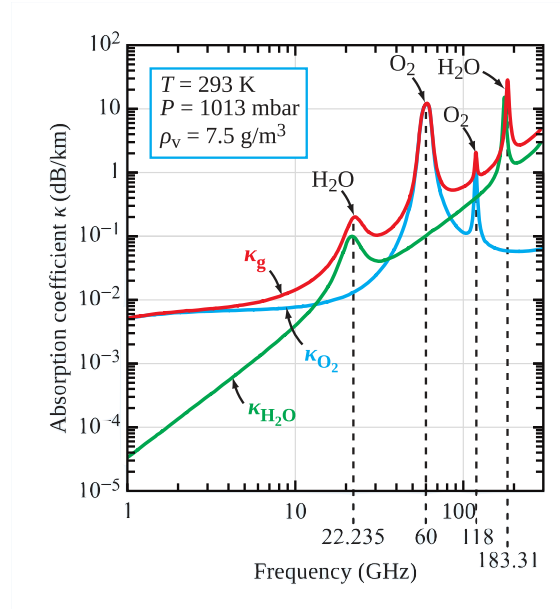


Figure 2.2.: Absorption spectra of oxygen (blue), water vapour (green) and their sum (red) at sea level. Taken from Ulaby et al. (2014) (Fig. 8-7 therein).

Thermal infrared

Ozone, water vapour and carbon dioxide absorption make the atmosphere opaque over large parts of the thermal infrared spectrum. There are, however, two atmospheric win-

dows at 3–5 μm and 8–14 μm (see Fig. 2.3). The latter is used for the retrieval of the ice-surface temperature product which is used in this thesis. Volume scattering is relevant in the thermal infrared spectrum, although it is less pronounced than in the visible and near-infrared spectrum. The type of scattering depends on the wavelength and the size of the scattering particles. If the wavelength is much larger than the scattering particles, Rayleigh scattering occurs. It is inversely proportional to the fourth power of the wavelength and thus much more effective in the visible spectrum than in the thermal infrared spectrum. Scatterers whose diameter is comparable to the wavelength, i.e., smoke or dust, cause Mie scattering. Finally, non-selective scattering occurs if the diameter of the scatterer is much larger than the wavelength.

Clouds and fog absorb and emit thermal infrared radiation and therefore mask the underlying surface. Reliable cloud masking is thus indispensable for working with thermal infrared data. For multi-spectral instruments like MODIS, information from the visible and thermal infrared bands can be used for cloud masking. Visible tests are based on the reflectance contrast between the surface and the cloud and thus not applicable over sea ice. Furthermore, sunlight is required for these tests, limiting their usefulness for sea-ice remote sensing to summer conditions. Therefore cloud masks over sea ice in winter are often only based on infrared measurements and thus less reliable than in mid-latitudes.

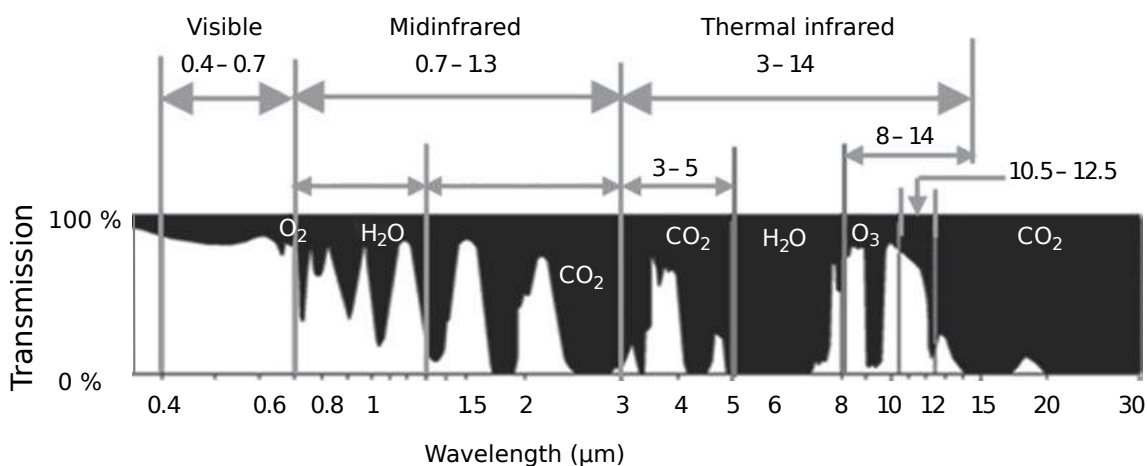


Figure 2.3.: Atmospheric absorption of different gases in the visible and thermal infrared spectrum. Taken and modified from Shokr and Sinha (2015) (Fig. 7.36 therein).

2.2. Sea ice

This section is dedicated to the description of sea-ice growth and the radiative properties of sea ice, snow and ocean water in the microwave and thermal infrared spectrum. It follows Shokr and Sinha (2015) if not stated otherwise.

2.2.1. Sea-ice growth

Sea ice starts forming as soon as the ocean temperature falls beneath the freezing point. The freezing point depends on the salinity and can be as high as -1.09°C in the marginal seas where the salinity goes down to 20 (Zatsepin et al., 2010), but is between -1.76°C and -1.87°C for typical Arctic salinities between 32 and 34 (calculated after Millero and Leung (1976) assuming standard sea-level pressure). Salinity values are normally given without unit. Salinity is typically measured as the weight of the salts dissolved in one kilogram of seawater, thus a salinity of 32 means that one kilogram of seawater contains 32 grams of salt.

Ice growth can be subdivided into three phases: initial nucleation, lateral growth and vertical growth. During the nucleation phase, sea ice crystals form around small ice nuclei. After developing to discoids of 2-3 mm initially, they grow anisotropically, assuming a star-like crystal shape. At some point, the arms of the stellar crystals break off and turn into needle-shaped crystals which are suspended vertically in the water, so-called frazil ice. Once these frazil needles start freezing together, the lateral growth phase starts.

Frazil needles can form grease ice, a slushy layer on the ocean surface which dampens the waves. At this point and under calm conditions, the formation of nilas starts. Nilas is an elastic and continuous sheet of sea ice which is 1-2 cm thick under calm conditions. Typically, wind would break the nilas into sheets which are up to tens of meters wide. If wind and waves prevent the formation of nilas, the frazil ice needles will be compressed and freeze together, forming round disks called pancake ice with diameters which are typically not much larger than 1 m. Large pancakes may again be broken by waves or form cake ice. At this stage, the sea ice cannot grow horizontally any more and grows purely vertically. In the vertical growth phase, sea ice grows by freezing from below (congelation ice). Ice with a thickness between 10 cm and 30 cm is called young ice. Ice thicker than that is referred to as thin, medium and thick first-year ice if it is thicker than 0.3 m, 0.7 m and 1.2 m, respectively. Thermodynamical growth is limited because the sea-ice cover insulates the warm ocean from the cold atmosphere, even more so if it is covered by snow. The factors which favor or impede thermodynamical ice growth are discussed below. Besides the fact that thicker and snow-covered ice grows more slowly, thermodynamical ice growth is limited to the cold months and the ice starts to melt once the air temperatures are above the freezing point. If the ice survives the melting season, it is referred to as multi-year ice. An empirical formulation which parameterises the thermodynamical sea-ice growth as a function of so-called freezing degree days is given by Lebedev (1938):

$$h = 1.33 \times FDD^{0.58}, \quad (2.10)$$

where h is the sea-ice thickness in cm and FDD are freezing degree days. Freezing degree days are a measure of how long it has been how cold. They are calculated as the deviation

of the daily mean air temperature from 0 °C summed over a certain time, where positive air temperatures are counted negatively and negative ones are counted positively. Two days with daily mean air temperatures of -5 °C and -3 °C are thus equivalent to eight freezing degree days. Figure 2.4 shows how thermodynamic growth looks when employing equation 2.10.

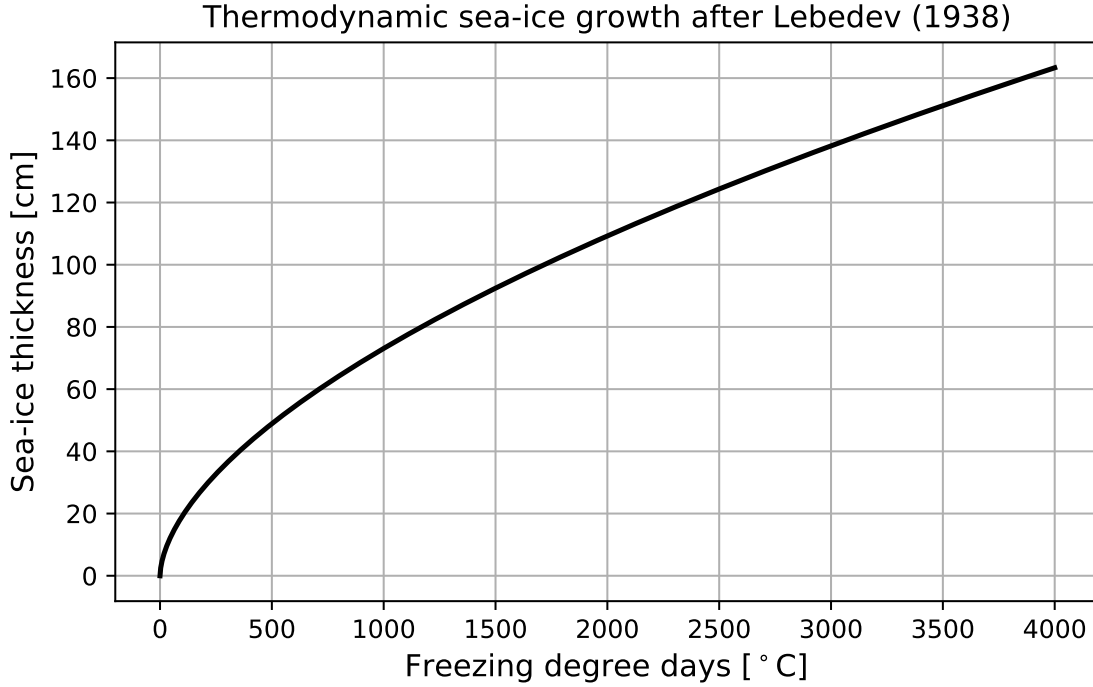


Figure 2.4.: Sea-ice thickness calculated employing the empirical formulation of Lebedev (1938).

The parameterisation of Lebedev (1938) is a simplifying assumption which neglects sea-ice dynamics, sea-ice surface conditions and snow cover. In general, the ice will start to grow thermodynamically as soon as the air temperature falls beneath the freezing point and continue to grow until the heat loss to the atmosphere at the surface equals the heat gain by the ocean at the bottom. In terms of heat fluxes, this is formulated in the equation

$$\frac{dh_i}{dt} = \frac{F_c - F_w}{\rho_i L_i}, \quad (2.11)$$

with the ice growth rate dh_i/dt , the conductive heat flux through the ice and snow F_c , the heat flux from the warm ocean to the colder ice F_w , the latent heat of freezing of water L_i , and the ice density ρ_i , defining upward fluxes as positive. If the above-mentioned thermal equilibrium condition is reached, F_c and F_w in equation 2.11 are equal and dh_i/dt is zero. If F_c is larger than F_w , the cooling from the atmosphere supersedes the warming from the bottom and the ice grows. Consequently, if F_w is larger than F_c , the warming from

the ocean dominates and the ice melts. According to Shokr and Sinha (2015), the oceanic heat flux F_w can often be neglected as it is comparably small, therefore we focus on the description of the conductive heat flux F_c . It is given by

$$F_c = -\frac{T_a - T_w}{\left(\frac{1}{k} + \frac{h_i}{k_i} + \frac{h_s}{k_s}\right)}, \quad (2.12)$$

where T_a and T_w are the air and water temperature, respectively, k is the effective heat transfer coefficient between the air and the surface and h_i , h_s , k_i , and k_s are the ice thickness, the snow depth and the thermal conductivities of ice and snow, respectively. From the numerator in equation 2.12, we infer that large vertical temperature gradients cause a large conductive heat flux and thus rapid ice growth/melt, depending on the sign. Note that „large“ here and in the following refers to the absolute value of the heat flux. Furthermore, large ice thicknesses and snow depths increase the denominator in equation 2.12, thus decreasing the conductive heat flux and slowing down ice growth/melt. This reflects that the ice growth declines nonlinearly with time, assuming that the other contributors in the equations 2.11 and 2.12 are constant. Lastly, we learn from equation 2.12 that small thermal conductivities of ice and snow decrease the absolute value of the conductive heat flux and thus slow down the ice growth. The thermal conductivity is inversely related to the capacity of the material to act as insulator. In Fig. 2.5, we compare the effect of the ice thickness, the snow depth and the thermal conductivities of ice and snow by varying one of the parameters by the ranges given in the caption of Fig. 2.5 while keeping the others constant (mind the logarithmic scaling). Also, note that the magnitude of the conductive heat flux is not necessarily representative since we neglect the heat transfer coefficient ($1/k$ equal 0 in equation 2.12) since the purpose of this Figure is to demonstrate the relative impact of variations in the ice and snow parameters for the conductive heat flux and thus the ice growth. Also, the 1 m that we take as upper limit for the snow depth is larger than the largest snow depth reported by, e. g., Rostosky et al. (2018), which is about 50 cm.

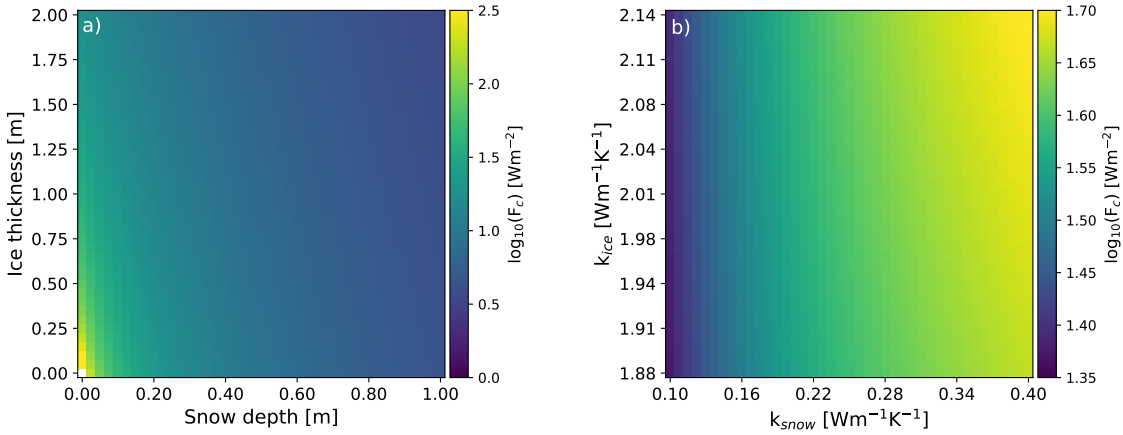


Figure 2.5.: Conductive heat flux through the ice and snow calculated from equation 2.12, neglecting the effective heat transfer coefficient. We assume $T_a = -30^\circ\text{C}$, $T_w = -1.86^\circ\text{C}$, $h_i = 0.5\text{ m}$, $k_i = 2\text{ Wm}^{-1}\text{K}^{-1}$, $h_s = 0.05\text{ m}$, and $k_s = 0.25\text{ Wm}^{-1}\text{K}^{-1}$. a) shows the logarithm to the base 10 of the conductive heat flux, varying the ice thickness h_i between 0 m and 2 m and the snow depth h_s between 0 m and 1 m. The thermal conductivities k_i and k_s are kept at the values given above. b) shows almost the same, but varying the thermal conductivity of ice between $1.88\text{ Wm}^{-1}\text{K}^{-1}$ and $2.14\text{ Wm}^{-1}\text{K}^{-1}$ and the thermal conductivity of snow k_s between $0.10\text{ Wm}^{-1}\text{K}^{-1}$ and $0.40\text{ Wm}^{-1}\text{K}^{-1}$. The ice thickness h_i and the snow depth h_s are kept constant. Mind the different colour scale compared to a). The ranges for k_i and k_s are taken from Shokr and Sinha (2015).

Fig. 2.5 a shows that the conductive heat flux is more sensitive to the snow depth than to the ice thickness. However, the sensitivity towards the snow depth decreases quickly after the first centimeters of snow have fallen. The sensitivity to ice thickness declines less quickly. Furthermore, the conductive heat flux hardly depends on the thermal conductivity of the ice (see Fig. 2.5 b), but does depend on the thermal conductivity of the snow, which in turn depends on the snow type. Since the sensitivity towards snow depth decreases quickly, the thermal conductivity is more important than the snow depth after the first centimeters of snow have fallen. When the snow gets compacted and/or wet, i. e., the snow density and/or its water content increase, its thermal conductivity increases. Shokr and Sinha (2015) exemplify this by giving ice thicknesses which would have the same insulation effect as 5 cm of different snow types. 3.20 m of ice would be needed for the same insulation effect as 5 cm of fresh soft snow with a low density. Only about 0.27 m of ice would be needed for the same insulation effect as 5 cm snow if the snow is hard and packed, i. e., has a higher density. This also influences the surface temperature: If the ice and snow are thick enough to mask the ocean signal, i. e., thermal equilibrium is reached, we expect the surface temperature to directly follow the surface air temperature. Until thermal equilibrium is reached, the surface temperature is influenced by the warming from the ocean. This influence is more pronounced for freshly grown, thin ice than for thicker

ice and more pronounced for bare than for snow-covered ice. As for the overall growth rate, we expect the influence of the snow depth on the surface temperature to be stronger than the influence of the ice thickness.

Apart from thermodynamical growth, the ice thickness changes due to sea-ice dynamics when a floe breaks apart or collides with another floe and the floes are shifted upon each other (rafting) or pile up against each other, forming pressure ridges and keels (ridging). This causes ice thicknesses which are far larger than what would be acquired by thermodynamic growth and is reflected in the high end of the Arctic-wide ice thickness distribution.

2.2.2. Radiative properties of sea ice, snow and ocean

The passive microwave surface emission is mainly dominated by emissivity variations. While there is a large contrast between the emissivities of first-year and multi-year ice at 89 GHz, the polarisation difference is small for all sea-ice types (see Fig. 2.6). One of the properties which strongly influence the emissivity in the microwave regime is the sea-ice salinity. When sea water freezes, most of the salt which it contains is expelled. After this rapid initial desalination, the rest of the salt remains entrapped in small inclusions with highly saline water, so-called brine-pockets. With time, most of the brine will drain towards the ice-water interface under the influence of gravity, leaving behind a network of brine channels (Notz and Worster, 2009). A smaller part of the brine may diffuse towards the surface (Shokr and Sinha, 2015). In the melt season, draining melt ponds can flush the remaining brine out of the sea ice, making multi-year ice less saline and more porous than first-year ice. Apart from brine, sea ice also contains air in form of air bubbles or drained brine channels, making it a heterogeneous mixture of liquid brine, air and sea ice. The relative volume fractions of these three components (ice, air and brine) determine the permittivity. It is dominated by the brine content as the permittivity of brine is much higher than that of sea ice and air. Temperature influences the brine content and thus indirectly the permittivity of sea ice. Under decreasing temperatures, the brine partly freezes and the salinity in the remaining brine increases. In fact, the brine salinity can be expressed as function of temperature only (Ulaby et al., 2014). The salinity, and thus the permittivity, differs between sea-ice types as indicated above, generally decreasing with increasing sea-ice thickness, from bulk values of 14 for sea ice thinner than 10 cm to 0.5 for sea ice thicker than 2 m.

The emission at the surface is the integral of the emission of the emitting layer. The depth of the emitting layer depends on the ice type, snow cover and frequency. It is smaller for higher frequencies. For multi-year ice at 89 GHz, it is on the order of centimeters and for first-year ice on the order of millimeters. The emitting layer depth of the snow layer decreases once snow metamorphism or melt start. Shokr and Sinha (2015) do not give distinct values for 89 GHz, but report that the emitting layer depth at 37 GHz decreases

from 1.1 m for dry snow to 3.5 cm for a volumetric water content of 2%. As the emitting layer depth decreases with increasing frequency, we expect that 89 GHz values are lower than this. The surface signal at 89 GHz thus mainly comes from the snow pack. Only in dry, fresh snow the emitting layer depth is almost 1 m, i. e., larger than what one would typically expect as snow depth and the surface signal thus comes from the ice.

Fig. 2.6 shows that radiation emitted by the ocean is more polarised than radiation emitted by the sea ice. This is employed for SIC retrieval at 89 GHz. The polarisation difference is largest for a calm ocean surface. A rough ocean surface will alter the antenna signal as the atmospheric radiation is not only reflected specularly, but also scattered, according to e. g. the Bragg approximation for rough surfaces. Surface roughness depolarises the radiation emitted by the ocean because the horizontal polarisation increases, while the vertical polarisation is less affected. Foam on the ocean increases the emission, but affects both polarisations similarly.

In the thermal infrared spectrum, snow, sea ice and ocean act almost as blackbodies with emissivities of around 0.96. Therefore, the measured brightness temperature mainly depends on the physical surface temperature. Small variations in the physical surface temperature cause large variations in the emitted radiation. This is a consequence of equation 2.3, which states that the emitted radiation is proportional to the fourth power of the surface temperature. The temperature contrast between sea ice and ocean is thus well-suited for sea-ice concentration retrieval. However, the temperature also depends on the sea-ice thickness, the snow depth and the properties of the sea ice and the snow, as described in subsection 2.2.1. It is therefore not always possible to distinguish sea-ice/snow thickness and sea-ice concentration in thermal infrared measurements. In other words, a pixel with 80% of thick, snow-covered sea ice and 20% open water may have the same surface temperature as a pixel with 100% coverage of thinner, bare sea ice.

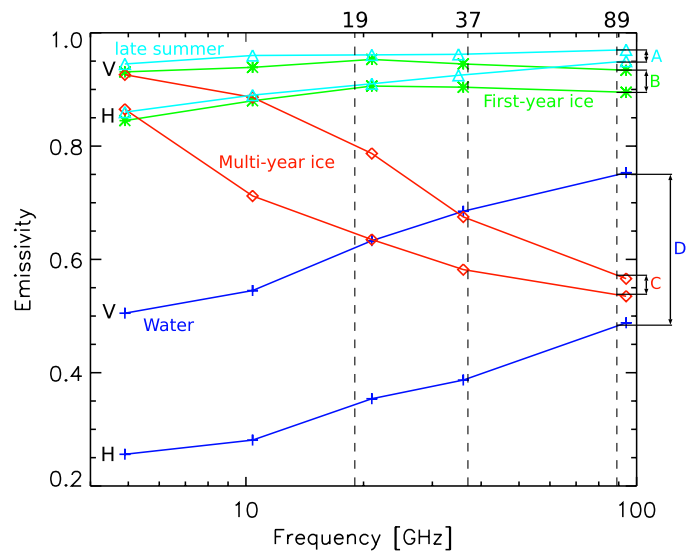


Figure 2.6.: Microwave emissivities of different surface types at vertical (V) and horizontal (H) polarisation. The stars, diamonds and crosses show measurements of Farrelly et al. (1983), the triangles show measurements of Onstott et al. (1987). Measurements were taken at an incidence angle of 50° . Figure taken from Spreen et al. (2008) (Fig. 1 therein).

3. Data

This chapter starts with a description of the input data for the merged sea-ice concentration product which is the primary outcome of this thesis in section 3.1. The subsections 3.1.1 and 3.1.2 first describe the instruments (MODIS and AMSR2, respectively), the datasets themselves (ice-surface temperature and sea-ice concentration, respectively) and then the specific subsets of data which were used for the thesis. It concludes with a description of the orbital constellation of the Aqua and Global Change Observation Mission–Water 1 (GCOM-W1) satellites. The sections 3.2 and 3.3 present the reflectance data used for the reference sea-ice concentration datasets and the other sea-ice concentration datasets, respectively. The Sentinel-1 mosaics and the reanalysis data used for the case study are described in the sections 3.4. Finally, section 3.5 presents the sea-ice thickness data used in this thesis.

3.1. Input data for merged dataset

3.1.1. MODIS data

The MODIS instrument

The MODIS instrument is carried by National Aeronautics and Space Administration (NASA)’s Terra and Aqua satellites, launched in 1999 and 2002, respectively. MODIS is a push-broom sensor with scan angles of $\pm 55^\circ$ and a swath width of 2330 km which operates in the visible and infrared wavelength regime. It provides measurements in 36 wavelength bands centered at wavelengths between 645 nm and 14.235 μm . The bands have spatial resolutions at nadir between 250 m with bands 1 and 2, 500 m with bands 3–7 and 1000 m with bands 8–36. Detailed information about the primary usage of the single bands is given on the homepage of NASA’s Goddard Space Flight Center (GSFC) (GSFC, 2020b). Their actual spatial resolution decreases with increasing scan angle and goes down to 4.8 km across-track \times 2 km along-track at either edge of the swath for the 1000 m bands and proportionally for the 500 m and 250 m bands (Masuoka et al., 1998).

Ice-surface temperatures

The MYD29 ice-surface temperature product used in this thesis is based on brightness temperatures of band 31 (centered at 11.03 μm) and band 32 (centered at 12.02 μm). A

split-window technique is used by Hall et al. (2004) to derive the ice-surface temperature by applying the regression model

$$IST = a + bT_{31} + c(T_{31} - T_{32}) + d[(T_{31} - T_{32})(\sec \theta - 1)], \quad (3.1)$$

where IST is the ice-surface temperature, T_{31} and T_{32} are the brightness temperatures of the bands 31 and 32, respectively, θ is the sensor scan angle and a , b , c and d are regression coefficients given on the product’s homepage (NSIDC, 2020b). The algorithm and processing have been developed at Goddard Space Flight Center (Hall and Riggs, 2015), the data are operationally provided by the NSIDC via an HTTPS server (NSIDC, 2020a). The MYD29 data are swath data sliced into granules with 1 km grid spacing which cover roughly 5 minutes. Each granule has a spatial dimension of 2030 km by 1354 km. Further details on the MYD29 product are given in Hall et al. (2004) and in the Algorithm Theoretical Basis Document (ATBD) (GSFC, 2020c).

Cloud mask

Cloud screening is typically a compromise between a conservative approach, where the number of available surface pixels is maximised at the expense of erroneously taking cloud pixels for surface pixels, and a strict approach, where the confidence that the pixels treated as cloud-free are actually cloud-free is maximised, at the expense of erroneously discarding cloud-free pixels.

The MYD35_L2 product (GSFC, 2020a) accounts for this by providing the cloud mask as an 8-byte integer, whose binary representation conveys not only the result cloudy/not cloudy, but also information about the confidence in the cloud masking and the outcome of the single tests. The confidence flags are calculated as combination of the confidence in the outcome of the single tests. ‘Confidence’ means confidence in the pixel being cloud-free. Pixels with a confidence > 0.99 are labeled as ‘confident clear’. The other flags are ‘probably clear’ ($.99 \geq \text{confidence} > 0.95$), ‘probably cloudy’ ($0.95 \geq \text{confidence} > 0.66$), and ‘confident cloudy’ ($0.66 \geq \text{confidence}$). A detailed description of the confidence levels and the single tests is given in Ackerman et al. (2010). The product is available online via Hypertext Transfer Protocol Secure (HTTPS) (LAADS, 2020a).

In the MYD29 product, Hall et al. (2004) apply a conservative cloud mask by masking only those pixels which are labeled as ‘confident cloudy’. We apply a stricter cloud mask by additionally using the MYD35_L2 product and also discarding pixels which are labeled as ‘probably cloudy’ and ‘probably clear’, thus only tolerating pixels which are labeled ‘confident clear’. Additionally, pixels over land, inland water and the open ocean are masked out by both cloud masks.

Usage in this study

997 MODIS granules are downloaded for the development of the MODIS sea-ice concentration and the evaluation of the merged, MODIS and ASI sea-ice concentration in chapters 5 and 6, respectively. These are all granules which intersect with one of the Sentinel-2 scenes described in subsection 3.2.1 on the day of their acquisition. For the results presented in the subsections 5.2–5.4, all of these granules are used. For the results presented in subsection 5.1 and chapter 6, we select the cloud-free MODIS granule with the smallest time-lag, accepting larger time-lags if needed to get cloud-free scenes. No intercomparison is done if there is no cloud-free MODIS granule within two hours of the Sentinel-2 acquisition time. MODIS granules which meet this requirement are available for 66 Sentinel-2 scenes.

For the case study in chapter 7, we download all MODIS granules north of 60°N between February 8, 2018 and March 31, 2018. Data between $45^\circ\text{W}/81^\circ\text{N}$ and $5^\circ\text{W}/85^\circ\text{N}$ in geographical coordinates are used for the analysis.

3.1.2. ASI sea-ice concentration

The AMSR2 instrument

The AMSR2 instrument aboard Japan Aerospace Exploration Agency (JAXA)'s GCOM-W1 (launched in 2012) is a conically scanning passive microwave radiometer with an incidence angle of 55° and a swath width of 1450 km which operates in the microwave frequency regime. It measures horizontally and vertically polarised electromagnetic radiation in seven frequency bands between 6.9 GHz and 89 GHz. The spatial resolutions get finer with increasing frequency, ranging from 35 km by 62 km (6.9 GHz) to 3 km by 5 km (89 GHz) in the instantaneous field of view. Due to the small footprint size of the 89 GHz channels, these channels have two scan lines, A-scan and B-scan, whose measurements are combined to close the gap between the two scan lines. More detailed information about the instrument and the usage of the single bands is given on the instrument's homepage (JAXA, 2020).

Sea-ice concentration

Several algorithms exist to retrieve SIC from the AMSR2 frequency bands (see chapter 1), but in this thesis the ASI algorithm (Kaleschke et al., 2001; Spreen et al., 2008) is used almost exclusively. AMSR2 SIC in this thesis are derived by ASI unless explicitly stated differently.

ASI uses the 89 GHz frequency bands. At this frequency, water polarises more strongly than sea ice. The polarisation difference (difference between the vertical polarisation and

the horizontal polarisation) can thus be used to derive SIC. The third-degree polynomial

$$SIC = 1.64 \times 10^{-5} p^3 - 0.0016 p^2 + 0.0192 p + 0.9710 \quad (3.2)$$

gives the sea-ice concentration SIC as a function of polarisation difference p (Spreen et al., 2008). Due to the enhanced atmospheric influence at 89 GHz, Spreen et al. (2008) apply three weather filters to filter out spurious SIC over the open ocean. Two of them discard pixels with a gradient ratio (difference between two vertically polarised frequencies divided by their sum) above a certain threshold. The third one discards pixels for which the Bootstrap algorithm (see subsection 3.3.1) shows less than 5% SIC. Details are given in Spreen et al. (2008). Over sea ice, the atmospheric influence still persists and can cause larger sea-ice concentration uncertainties. ASI SIC are provided as a daily gridded product at 6.25 km and 3.125 km grid spacing by the University of Bremen (University of Bremen, 2020).

Usage in this study

For the best temporal consistency with the MODIS data, we use swath data processed internally instead of the daily product. They are calculated as half-orbits, combined to orbits and then interpolated to the same projection and grid spacing as the MODIS data. For descending half-orbits (i. e., from the North Pole to the South Pole), we take the time of the first measurement as acquisition time and for ascending half-orbits (i. e., from the South Pole to the North Pole), we take the time of the last measurement as acquisition time. For the intercomparison with the Sentinel-2 SIC, the swath data are resampled to the same Transverse Mercator projection as the Sentinel-2 data, like the MODIS SIC.

For the merged SIC evaluation in chapter 6, the AMSR2 swath pertaining to the closest MODIS granule (see subsection 3.1.1) was selected. For the case study in chapter 7, all AMSR2 swaths between February 8, 2018 and March 31, 2018 are used and gridded to the region between 45° W/81° N and 5° W/85° N in geographic coordinates, analogous to the MODIS SIC. On average, eight matching MODIS and AMSR2 overflights per day are available for this region.

3.1.3. Aqua, GCOM-W1 and the A-Train

Aqua and GCOM-W1 are both part of the A-Train satellite constellation (NASA, 2020). The A-Train is a suite of four satellites which follow each other closely on the same sun-synchronous low-Earth orbit with an inclination of 98°. It was designed to obtain near-simultaneous Earth observation data from different measurements. The flight height is 705 km and 700 km for Aqua and GCOM-W1, respectively. The satellites in the A-Train

cross the equator at 1:30 am/pm local time on their descending (southbound)/ascending (northbound) orbits. The time lag between Aqua and GCOM-W1 is small (4 minutes). This is of paramount importance for merging data, especially at a fine spatial resolution of 1 km and also the reason why we do not use MODIS Terra data, which would have a time lag of 45 minutes.

3.2. Reflectance data for reference sea-ice concentration

3.2.1. Sentinel-2 reflectances

Sentinel-2 reflectances are used for validation. The European Union (EU) Copernicus Sentinel-2A/B satellites have been launched in June 2015 (Sentinel-2A) and March 2017 (Sentinel-2B). They follow a sun-synchronous orbit at 786 km altitude and 10:30 am equator crossing time. Their phase is shifted by 180° . Their payload, the Multi Spectral Instrument (MSI), features 13 bands in the visible and shortwave infrared spectral region and has a swath width of 290 km. To obtain a reference sea-ice concentration dataset, we download 79 cloud-free scenes from the Copernicus open-access hub (ESA, 2020), 66 of which could be used for the evaluation. We make sure that they are cloud-free by checking every scene visually. Figures 3.1, 3.2 and Table 3.1 offer a spatial and temporal overview over the scenes. Scenes with more than two hours time lag towards the next MODIS/AMSR2 overflight are not used for the intercomparison, but included in the thesis because of their possible relevance for other validation studies. The scenes were recorded in the East Siberian, Laptev, Kara, Barents, Beaufort Sea and in the Fram Strait between February 22, 2019 and May 27, 2019. The scenes comprise mainly first-year ice with smaller amounts of young ice. Ice type maps based on Advanced Scatterometer (ASCAT) and AMSR2 data (Shokr et al., 2008; Ye et al., 2016a,b) show some multi-year ice in the East Siberian, Fram Strait and Beaufort Sea (not explicitly shown here). For this study, Level 1 C reflectances at 665 nm (band 4) with a spatial resolution of 10 m have been used. Level 1 C data are top-of-the-atmosphere reflectances which are projected onto a Universal Transverse Mercator projection.

Table 3.1.: Number of Sentinel-2 scenes for the respective region and month. If there is a number in brackets, it gives the number of scenes after discarding Sentinel-2 scenes for which no cloud-free MODIS measurement was available within two hours of the acquisition. Without brackets, all scenes could be used.

Region	Feb	Mar	Apr	May	Total
East Siberian Sea	0	10 (3)	8 (5)	0	18 (8)
Laptev Sea	3	4	2	10	19
Kara Sea	3	7	10	9 (8)	29 (28)
Barents Sea	0	1	0	2	3
Fram Strait	0	1 (0)	2 (1)	1	4 (2)
Beaufort Sea	1	1	2	2	6
All	7	24 (16)	24 (20)	24 (23)	79 (66)

3.2.2. Landsat 8 reflectances

To evaluate our results against other fine-resolution visible observations, we download five scenes of NASA’s Landsat 8 satellite (launched in 2013). The Operational Land Imager (OLI) aboard the Landsat 8 satellite measures at nine spectral bands centered at wavelengths between 0.44 μm and 1.37 μm . We use band 4 reflectances centered at 0.65 μm with a spatial resolution of 30 m. As for the Sentinel-2 data, the scenes were selected manually to ensure that no clouds obstructed the field of view. The scenes are located in the Laptev Sea and were acquired in March and April 2015 and 2016 (see Fig. 3.3).

Furthermore, ten cases were identified in which the ASI SIC underestimated SIC over landfast ice (Wiedemeier and Ludwig, 2017). These cases are between January and April 2015 and located in the East Siberian, Chukchi and Beaufort Seas, north of Greenland close to Nares Strait, in the Canadian Archipelago and in the Baffin Bay (see Fig. 3.3).

3.3. Other sea-ice concentration data

3.3.1. Bootstrap, NASA Team and ECICE sea-ice concentration

Bootstrap (Comiso, 1986, 1995; Comiso et al., 1997), NASA Team (Cavalieri et al., 1984) and Environment Canada’s Ice Concentration Extractor (ECICE) (Shokr et al., 2008; Ye et al., 2016a,b) SIC are only used in one scene in subsection 6.3.3 for comparison to ASI SIC and will therefore be treated very briefly.

Both NASA Team and Bootstrap use the vertical polarisation of the 19 GHz and the 37 GHz frequency channels. NASA Team additionally uses the horizontal polarisation of the 19 GHz channel, Bootstrap uses the 37 GHz horizontal polarisation. The Bootstrap SIC are retrieved from AMSR2 data and are processed internally. The NASA Team SIC are produced from Special Sensor Microwave Imager/Sounder (SSMIS) data and are dis-

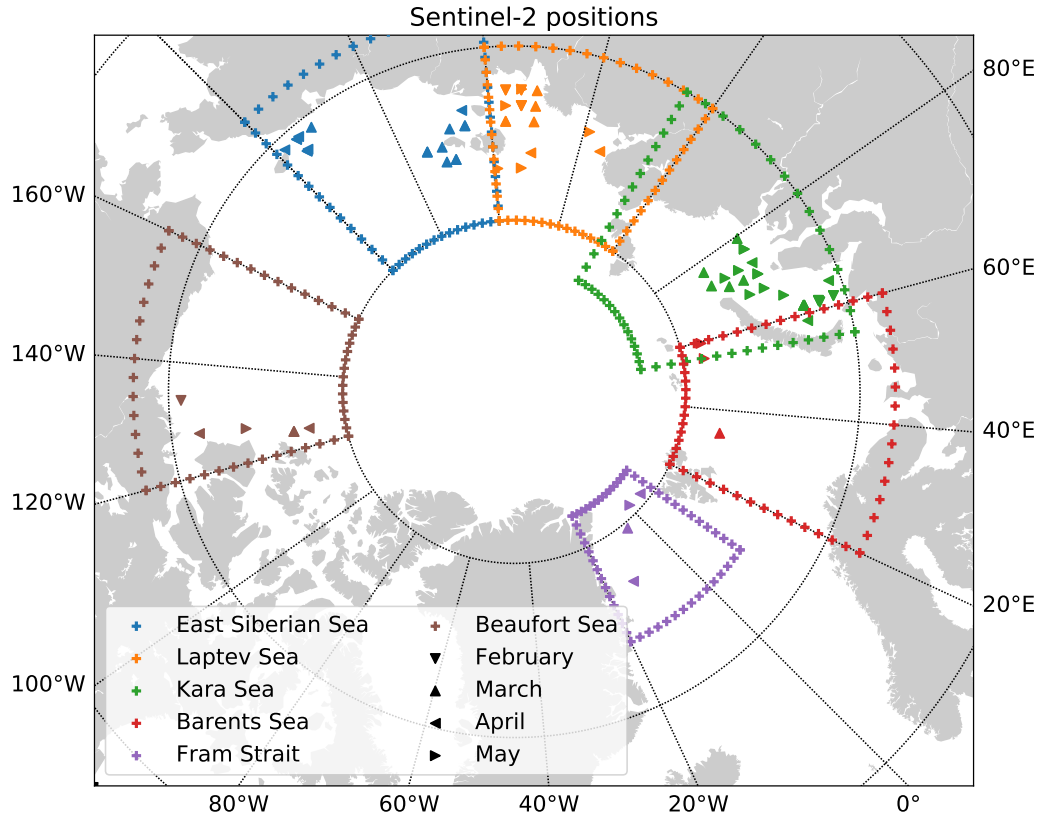


Figure 3.1.: Locations of the Sentinel-2 scenes. The polygons mark the regions which were used for defining the marginal seas. Regions are indicated by colours, Months are indicated by the orientation of the triangles (see legend for details). All in all, 66 scenes were used for the evaluation.

tributed by NSIDC (NSIDC, 2020c). ECICE employs a constrained optimisation scheme using backscatter at 5.3 GHz measured by ASCAT aboard European Organisation for the Exploitation of Meteorological Satellites (EUMETSAT)’s MetOp satellites and AMSR2 horizontally and vertically polarised brightness temperatures at 18 and 37 GHz, the data are also produced internally.

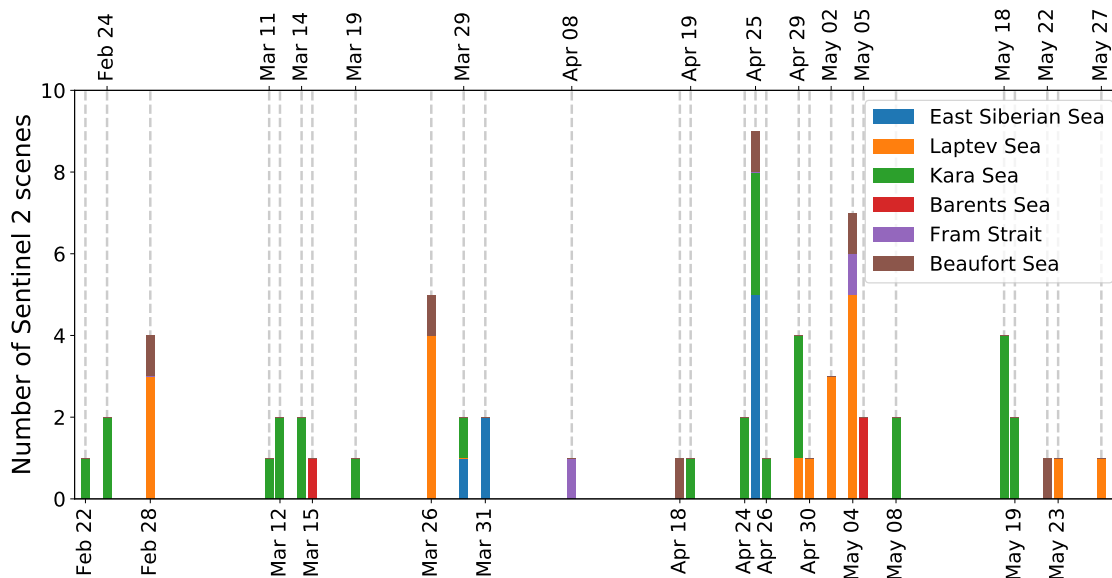


Figure 3.2.: Temporal overview over scenes. The respective dates are given on the x-axis, the spacing is scaled according to the time between the single days. The height of the bars gives the number of scenes. Bars from different regions on the same day are stacked upon each other. The colours of the bars indicate the region.

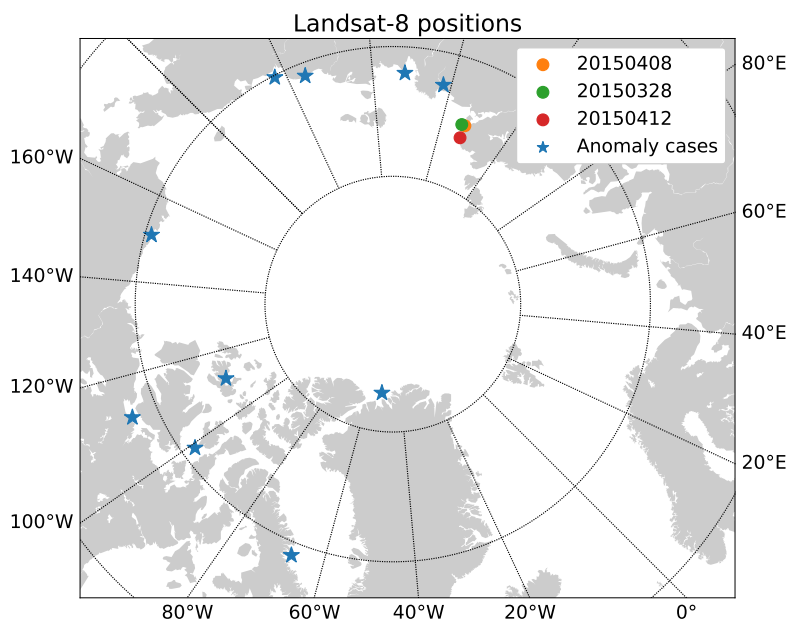


Figure 3.3.: Locations of the Landsat 8 scenes. The scenes which were used for the evaluation are marked by dots, the legend gives the dates. Anomaly cases (marked by stars) are cases where the ASI SIC underestimated SIC over landfast ice. They were acquired between January and April 2015. The exact dates are given in Wiedemeier and Ludwig (2017).

3.3.2. SAR sea-ice concentration

In the case study in chapter 7, we investigate a polynya which opened north of Greenland in February 2018. A polynya is a large, non-linearly shaped opening in the ice. In February and March, the months of our case study, visible data north of Greenland are not available for reference. Therefore, we use lead area fraction of the EU Copernicus Sentinel-1 satellite provided by Dmitrii Murashkin (personal communication). Leads are linear openings in the ice which contain water or thin ice. Binary lead maps are produced by an automatic classification algorithm from Sentinel-1 C-band SAR data at 5.4 GHz (Murashkin et al., 2018). The lead classification algorithm analyses backscatter values and image texture of the surrounding area. The algorithm is trained with small leads with a flat surface (Murashkin et al., 2018).

Sentinel-1 scenes taken in the Extra Wide Swath mode with 40 m pixel size are used. Images taken within one day are combined in lead maps of the Arctic with 80 m resolution. Then the lead area fraction is calculated from these binary maps on a 800 m grid. Finally, the data are resampled to the NSIDC grid with 1 km grid spacing for comparison with the other SIC datasets. Sea-ice concentration is derived by inverting the lead area fraction:

$$\text{SIC}_{LAF} = 1 - LAF, \quad (3.3)$$

where LAF is the lead area fraction. The product is called SAR SIC.

3.3.3. OSI SAF sea-ice concentration

For climatological reference in the case study, we use the OSI-450 SIC Climate Data Record product of the EUMETSAT Ocean and Sea Ice Satellite Application Facility (OSI SAF) which is described in Lavergne et al. (2019) and available from 1979 to 2015 (OSI SAF, 2020d). It uses the coarse-resolution instruments Scanning Multi-channel Microwave Radiometer (SMMR), SSM/I and SSMIS. The data are provided daily since 1987 and every two days before. They are gridded to a Lambert Azimuthal equal area grid, also known as Equal-Area Scalable Earth (EASE) grid 2.0, with a grid spacing of 25 km. For the years 2016–2018, the OSI-430-b SIC product (OSI SAF, 2020c) is used. The time series of both products is consistent at the transition (OSI SAF, 2020a). The climatology comprises the years from 1979 to 2017.

3.4. Sentinel-1 mosaics and reanalysis data

3.4.1. Sentinel-1 mosaics

To check whether the overfrozen polynya which is investigated in chapter 7 is still visible in SAR images, we use Sentinel-1 mosaics provided by Leif Toudal Pedersen (personal communication). Since fall 2014, the Technical University of Denmark has produced Near

Real Time mosaics of Sentinel-1 SAR data as they become available to the Copernicus Marine Environment Monitoring Service (CMEMS). The mosaics cover most of the potentially sea-ice covered areas of the Northern and Southern hemispheres, respectively. They consist of geometrically and radiometrically corrected data from Extra Wide Swath and Interferometric Wide Swath modes of both Sentinel-1A and Sentinel-1B. The radiometric correction includes a correction for the average incidence angle dependence of the sea-ice backscatter. The full mosaics are available online (TU Denmark, 2020).

3.4.2. Sea-ice drift, air temperature and air pressure

The OSI-405 low resolution sea-ice drift product by EUMETSAT OSI SAF (Lavergne et al., 2010) is used in the case study in chapter 7 to find the reason why the polynya opened. It has a grid spacing of 62.5 km, a temporal resolution of two days and is projected to the NSIDC grid. It is distributed by OSI SAF (OSI SAF, 2020b). Sea-ice motion is first derived separately from ASCAT C-band backscatter, AMSR-E/AMSR2 37 GHz, SSM/I 85 GHz and SSMIS 91 GHz brightness temperatures. Then, the single-sensor sea-ice drift vectors are merged by an optimal interpolation scheme.

To assess the environmental conditions during the polynya event, we use 2 m temperature data from the weather station at Cape Morris Jesup operated by the Danish Meteorological Institute. They are sampled in three-hour intervals until 2015 and hourly since 2016. We average the values daily.

Additionally, we use surface air pressure, 10 m wind and 2 m air temperature at a spatial resolution of 0.25 degrees and a temporal resolution of one day from the European Centre for Medium-Range Weather Forecasts Reanalysis 5th Generation (ERA5) reanalysis (ECMWF Copernicus Climate Change Service, 2020). The ERA5 reanalysis is run at the European Centre for Medium-Range Weather Forecasts (ECMWF). It is the fifth generation of reanalyses from ECMWF.

3.5. Sea-ice thickness data

3.5.1. Sea-ice growth from freezing degree days

For the polynya case study in chapter 7, we employ the freezing degree day parameterisation (see also subsection 2.2.1) described by Lebedev (1938) to estimate thermodynamic sea-ice growth in the polynya:

$$SIT = 1.33 \cdot FDD^{0.58} \quad (3.4)$$

where SIT is the sea-ice thickness in cm and FDD are freezing degree days. Freezing degree days are the sum of air temperatures above/below freezing over a given time, where air

temperatures below/above 0°C count positively/negatively:

$$FDD = - \sum_1^{n_{days}} [1 \cdot T_n^{air}], \quad (3.5)$$

where n is the index of the respective day, n_{days} is the total number of days and T_n^{air} is the daily mean air temperature in °C of the respective day. We use the ERA5 2 m air temperature. We will later compare sea-ice thickness from different sources. For a consistent comparison despite the very different grids, we introduce a grid-independent criterion to define the polynya region: We consider only those grid cells where the ERA5 SIC was below 50% at least once during the polynya event. The area of the entire grid cell is considered, not only the ice-covered area, which means that the sea-ice thickness is treated as the mean sea-ice thickness in the entire grid cell. In addition to sea-ice thickness, we calculate the sea-ice volume produced by thermodynamic growth. For this, we multiply the sea-ice thickness with the fixed area of grid cells for which the above-mentioned criterion applies.

3.5.2. Passive microwave sea-ice thickness

Sea-ice thickness up to 50 cm can be derived from 1.4 GHz passive microwave measurements (Huntemann et al., 2014; Patilea et al., 2019). We use the combined sea-ice thickness product of the Soil Moisture and Ocean Salinity (SMOS) and Soil Moisture Active Passive (SMAP) radiometers to evaluate the sea-ice growth from the freezing degree days. The product is disseminated by the University of Bremen (University of Bremen, 2020). It comprises both dynamic and thermodynamic growth. We need to ensure that we consider only those grid cells with thermodynamic sea-ice growth. Therefore, we apply the same criterion as described in subsection 3.5.1, using the ASI SIC as reference.

3.5.3. NAOSIM model

The North Atlantic Arctic Ocean Sea Ice Model (North Atlantic Arctic Ocean Sea Ice Model (NAOSIM), Kauker et al., 2003) has been used to calculate the sea-ice growth and the vertical heat fluxes during the polynya event investigated in chapter 7. The polynya area is defined as described in subsection 3.5.1. In contrast to the version described by Kauker et al. (2003), the present version uses a modified atmospheric forcing data set consisting of 10 m-wind velocity, 2 m-air temperature, 2 m-specific humidity, total precipitation, and downward solar and thermal radiation. For the period from 1979 to 2010 the forcing is taken from the National Center for Environmental Prediction (NCEP) Climate Forecast System Reanalysis (NCEP-CFSR) (Saha et al., 2010) and for the period from 2011 onwards from the NCEP Climate Forecast System version 2 (CFSv2) (Saha et al., 2014). For more details about NAOSIM the reader is referred to Kauker et al. (2003) and

to Sumata et al. (2019a,b). NAOSIM data have been provided by Frank Kauker (personal communication).

3.5.4. Airborne sea-ice thickness profiles

We use data provided by Christian Haas (personal communication) of an Airborne Electromagnetic (AEM) sea-ice thickness survey carried out over the southeastern region of the refrozen polynya on March 30 and 31, 2018, i. e., roughly five weeks after the polynya had begun to refreeze (see subsection 7.4. Surveys were carried out with a DC-3/Basler BT67 aircraft (Haas et al., 2010), and were processed as described by Haas et al. (2009). AEM data have an accuracy of ± 0.1 m over level ice but can underestimate the thickness of pressure ridge keels by up to 50% due to the large footprint of the AEM measurements of up to 45 m over which an average sea-ice thickness estimate is retrieved (Haas and Jochmann, 2003). Accuracy was confirmed by a sufficiently large number of small open leads with sea-ice thickness of zero meters. AEM measurements obtain the total, ice plus snow thickness. Visual observations during the flights showed that the snow on the young first-year ice of the polynya was less than 0.05 m thick and can be neglected for the purpose of this study. All measurements over small patches of multi-year ice embedded in the polynya have been removed from the data set. The results therefore represent the thickness of 5 weeks old first-year ice in those specific environmental conditions.

4. Methods

We start this chapter by describing the MODIS sea-ice concentration retrieval algorithm and the improvements which we made in section 4.1. Subsequently, the merging of MODIS and ASI sea-ice concentration is described. The formulation of the uncertainty estimates is the topic of section 4.3. Finally, we describe how we constructed the reference sea-ice concentration datasets and how we calculate the open-water extent in section 4.4.

4.1. MODIS sea-ice concentration

The MODIS SIC are derived from ice-surface temperatures. For the retrieval, accurate knowledge of the tie-points, in the thermal infrared spectrum also referred to as background temperatures, is crucial. The tie-points are the temperatures which a pixel would have if it were covered completely by open water (water tie-point) or completely by sea ice (ice tie-point). The choice of the open water tie-point is straightforward: we assume that the open water is constantly at the freezing point of salt water, -1.8°C . If it would be colder, the water would freeze to sea ice until thermal equilibrium is reached. If it would be warmer, it would melt the surrounding sea ice and thereby cool down to the freezing point. However, until equilibrium is reached also other water temperatures can be observed, which is part of the water tie-point uncertainty. The validity of assuming a constant freezing point is evaluated in subsection 5.3.

Defining an ice tie-point is much more challenging since the ice-surface temperature follows the surface air temperature and thus exhibits large spatial and temporal variability. The relation between surface air temperature and ice-surface temperature is influenced by the sea-ice thickness and the thickness of the snow on top of the sea ice, which both dampen the heat flux from the warm ocean to the cold air. Therefore, the ice-surface temperature follows the air temperature more closely for thicker and snow-covered ice. This makes the choice of a fixed, Arctic-wide ice tie-point impossible. The methodology to estimate the ice tie-point based on the local ice-surface temperature distribution has been developed for Advanced Very High Resolution Radiometer (AVHRR) thermal infrared measurements by Lindsay and Rothrock (1995) and applied to MODIS data by Drüe and Heinemann (2004). We first describe the approach by Drüe and Heinemann (2004) and subsequently our improvements published in Ludwig et al. (2019, 2020).

To account for the local variability of the ice-surface temperature, each pixel is assigned its own ice tie-point (Drüe and Heinemann, 2004). To retrieve this ice tie-point, the ice-

surface temperature field is split into cells of 48 pixels by 48 pixels. Only linear ice-surface temperature variation is assumed within these cells. Each cell is split into 3 by 3 subcells of 16 pixels by 16 pixels. Within a subcell, negligible ice-surface temperature variations are assumed. In the next step, the 25th percentile of the ice-surface temperature field in the subcell is selected as preliminary ice tie-point, so that there are 9 preliminary ice tie-point values per cell. The choice of percentile may seem random, but Lindsay and Rothrock (1995) showed that it does not significantly impact the result. Once the preliminary ice tie-points are determined, a linear regression with two variables is performed within the cell to express the ice tie-point as function of the x/y position within the cell:

$$tp_{ice}(x, y) = ax + by + c, \quad (4.1)$$

where tp_{ice} is the ice tie-point, a , b and c are the coefficients from the regression and x and y are the indices of the respective pixel within the cell. Subcells are discarded entirely if more than 70 % of the pixels have been covered by clouds, and cells are discarded entirely if more than four subcells have been discarded entirely. Drüe and Heinemann (2005) investigate the sensitivity of the retrieval towards the choice of the open water tie-point, the required fraction of cloud-free pixels within one subcell, the required number of valid subcells in one cell and the percentile for the estimation of the temporary ice tie-points. They confirm that the initial settings are a reasonable choice. So far, the approach directly follows Drüe and Heinemann (2004).

In Drüe and Heinemann (2004), the cells are shifted by 48 pixels once the calculation is done, so that each pixel is covered once. At the edges of the 48-km-by-48-km box, the regression coefficients change abruptly, thus sudden, physically implausible gradients are introduced into the ice tie-point and subsequently the sea-ice concentration field. We improve the method by decreasing the stepsize to 1 km, i. e., one pixel. Afterwards, the calculation is repeated. This way, an ensemble of up to 48 ice tie-points is available per pixel, depending on the cloud coverage of the surrounding pixels. A smaller number of possible ice tie-point values may occur if the pixel is located in a discarded cell or subcell in only some of the 48 iterations. On average, 37 possible ice tie-points were available for each pixel. More than 10 possible ice tie-point values were available for 99.5 % of the pixels. Therefore, we do not set a lower threshold for the number of possible ice tie-point values. The mean of all possible ice tie-point values is then selected as ice tie-point. This yields a much smoother ice tie-point field, as will be presented in section 5.1. Additionally, we can use the standard deviation of all possible ice tie-point values as estimate for the uncertainty of the ice tie-point, as will be described in section 5.3. The ice tie-point retrieval is illustrated in Fig. 4.1.

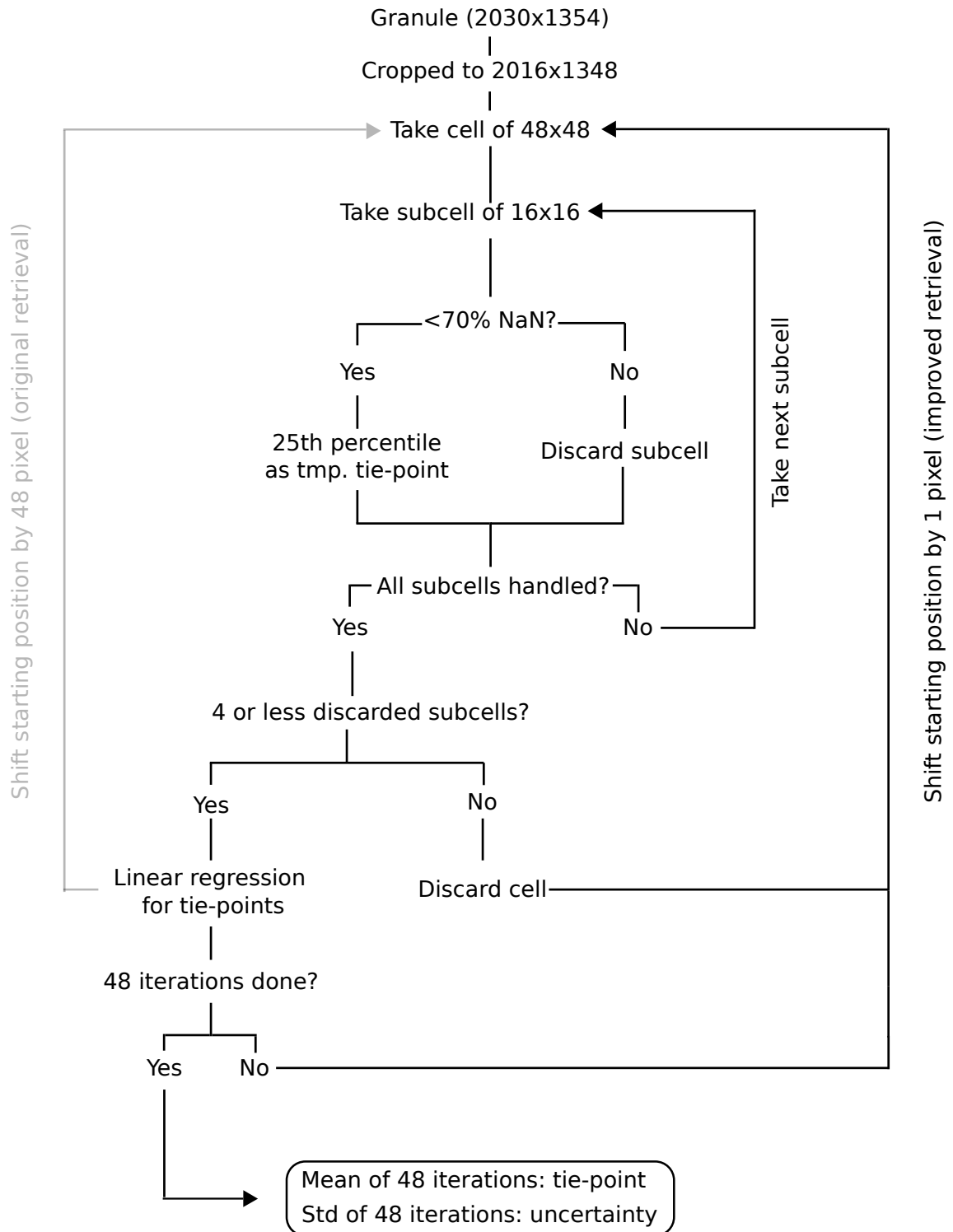


Figure 4.1.: Flowchart which illustrates the MODIS ice tie-point retrieval. The order of steps goes from top to bottom, unless indicated differently by arrows. The dimensions for a granule, a cell and a subcell are given in pixels, i. e., 2030x1354 means 2030 pixels by 1354 pixels.

Once the ice tie-point values for each pixel are determined, the ice-surface temperatures are converted to SIC by linear interpolation:

$$\text{SIC} = \begin{cases} 1 & \text{if } IST < tp_{ice} \\ \frac{IST - tp_{water}}{tp_{ice} - tp_{water}} & \text{if } tp_{ice} < IST < tp_{water} \\ 0 & \text{if } IST > tp_{water}, \end{cases} \quad (4.2)$$

where IST , tp_{ice} and tp_{water} are the observed ice-surface temperature and the ice and water tie-point, respectively. No SIC retrieval is performed in the current version of our retrieval if the ice tie-point exceeds 270 K. This initially chosen threshold is a conservative threshold, i. e., it allows to keep many pixels at the expense of large uncertainties due to the small dynamic range (see subsection 4.3.1 for the calculation of the uncertainties). A new threshold, which is a compromise between keeping as many pixels as possible and reducing the uncertainties as far as possible is derived in section 5.4.

The SIC calculation is performed on granule level. The granules are gridded to a polar stereographic grid with the latitude of true scale at 70°N, also known as the NSIDC grid (NSIDC, 2020d). The MYD03 geolocation product (LAADS, 2020b) at 1 km resolution is used for the gridding. Subsequently, granules pertaining to one swath are combined. The part of the swath above 60°N typically comprises four or five granules. We take the starting time of the last granule as acquisition time of the swath.

For the intercomparison with the Sentinel-2 SIC, the closest MODIS granules are resampled to the same Transverse Mercator projection and region as the Sentinel-2 SIC. The same has been done for intercomparison with the Landsat 8 SIC in subsection 6.2.2.

4.2. Merged sea-ice concentration

Having combined the gridded MODIS granules to one overflight, we select the corresponding AMSR2 overflight. As both platforms, Aqua and GCOM-W1, are part of the A-Train (see subsection 3.1.3), the time lag is on the order of minutes. Our central assumption for the merging is that the MODIS SIC capture the variability at 1 km resolution correctly, but underestimate the SIC if more than one ice thickness class is present in the 48-km-by-48-km region used for the tie-point retrieval. Furthermore, their availability is limited by the presence of clouds. The ASI SIC, on the other hand, are not as sensitive to thin ice and are thus closer to the right magnitude at a spatial scale of 5 km and are available independently of cloud coverage. We thus tune the mean of the MODIS SIC in an area of 5 km by 5 km (corresponding roughly to one AMSR2 footprint at 89 GHz) to match the mean of the ASI SIC.

First, the ASI swath data are resampled to a grid cell size of 1 km. Then, the difference between the mean MODIS SIC and the mean ASI SIC in a cell of 5 km by 5 km is calculated:

$$\Delta_{\text{SIC},5\text{ km}} = \text{SIC}_{\text{MODIS},5\text{ km}} - \text{SIC}_{\text{ASI},5\text{ km}}, \quad (4.3)$$

where $\text{SIC}_{\text{MODIS},5\text{ km}}$ and $\text{SIC}_{\text{ASI},5\text{ km}}$ are the mean MODIS and ASI SIC in the respective 5 km-by-5 km cell and $\Delta_{\text{SIC},5\text{ km}}$ is their difference. This difference is now added to each MODIS pixel in this box such that the mean within the box matches the mean of the ASI pixels. In the final step, the cloud gaps are filled by the respective ASI pixels:

$$\text{SIC}_{\text{merged},i,j} = \begin{cases} \text{SIC}_{\text{MODIS},i,j} + \Delta_{\text{SIC},5\text{ km}} & \text{if } \text{SIC}_{\text{MODIS},i,j} \text{ available} \\ \text{SIC}_{\text{ASI},i,j} & \text{if } \text{SIC}_{\text{MODIS},i,j} \text{ not available} \end{cases} \quad (4.4)$$

A scheme to illustrate the merging procedure is shown in Figure 4.2.

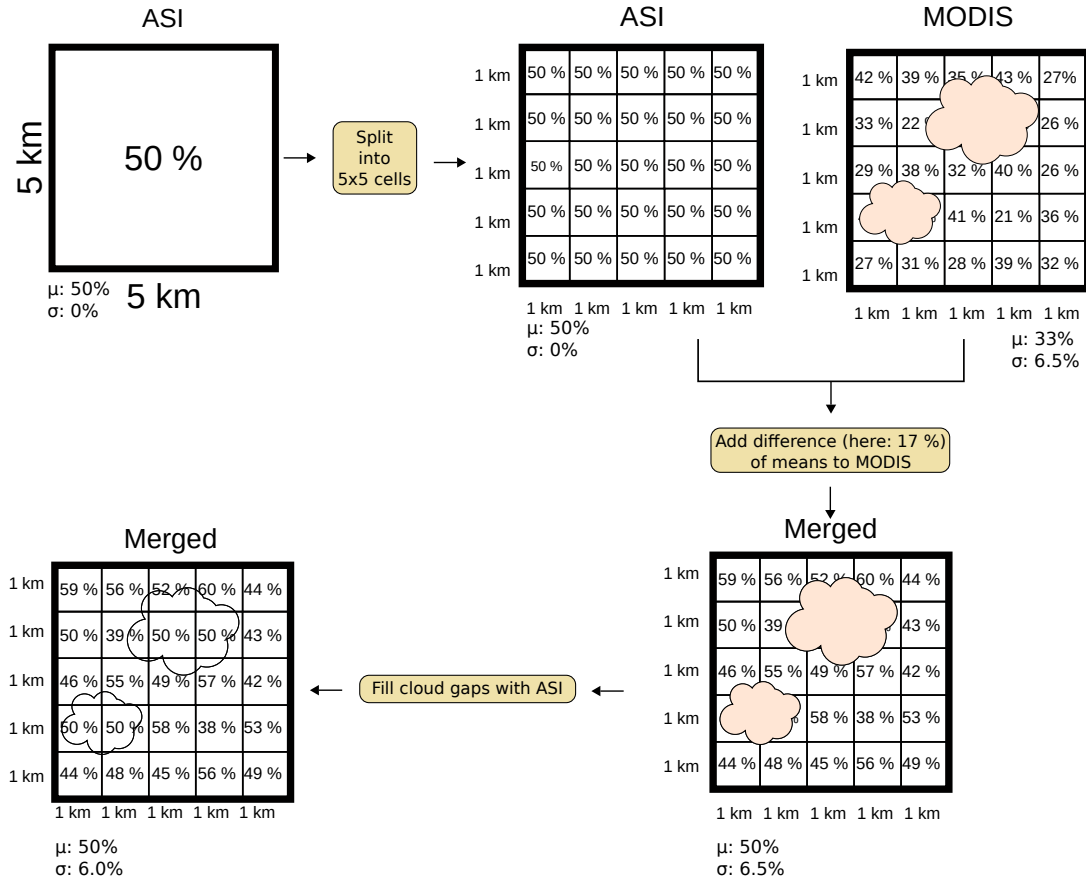


Figure 4.2.: Flowchart to illustrate the merging procedure. The % values give the SIC which the respective dataset sees in the respective grid cell, but they serve just for illustration and are not actually measured data. The mean and standard deviation in each 5 km-by-5 km grid cell are denoted by μ and σ , respectively.

A similar approach has been used by Gao et al. (2010). Other than them, we shift the 5 km-by-5 km box by 1 pixel before the calculation is repeated for each pixel in the box. The mean is selected as merged SIC value. This mitigates the inaccuracy of choosing arbitrary starting positions for the merging, in analogy to the approach which we chose for the ice tie-point retrieval in section 4.1. If the mean ASI SIC in the 5 km-by-5 km cell is close to 0 % or 100 %, the merged SIC at single pixels can be below 0 % or above 100 %. These pixels are set to 0 % and 100 % in the end. In that case the original ASI mean SIC is not completely preserved.

4.2.1. Operational implementation

The merged SIC dataset is produced operationally between October and May since October 2019. A subset of the Arctic-wide dataset is sent operationally to RV Polarstern during the Multidisciplinary drifting Observatory for the Study of Arctic Climate (MOSAiC) expedition (Alfred-Wegener-Institute, 2020). To find the optimal starting time for the processing, the upload time of the MODIS data was monitored for one month (not shown here). Both ice-surface temperature and geolocation were typically uploaded by 07:30 pm Central European Time (CET) on the day after acquisition, with some exceptions when the data were only uploaded by 10 pm CET. To make sure that the data are available, 10:55 pm CET is chosen as starting time. The time is chosen before 11 pm to avoid problems introduced by the change from winter to summer time and vice versa.

First, Extensible Markup Language (XML) files which pertain to the ice-surface temperature granules are downloaded from NSIDC. They contain information about the corner coordinates of the corresponding MODIS granules. These are read out and used to create a list with the filenames of all MODIS granules which are north of 60°N. Next, the Hierarchical Data Format 4 (HDF4) files containing these MODIS granules are downloaded, together with the geolocation data. Next, the ice tie-point calculation is started. Subsequently, the MODIS SIC is calculated on granule level. The granules are now gridded to the NSIDC grid, granules of one swath are combined.

ASI SIC are produced operationally by a separate, already implemented processing chain which saves the swath data. These data are gridded to the NSIDC grid and subsequently merged with the MODIS SIC as described in section 4.2. Finally, the daily mean of the merged SIC data is saved as Network Common Data Form 4 (NetCDF4) file and as geotiff file. The data are available for download and interactive viewing on our research group's website (University of Bremen, 2020). A second NetCDF4 file including the daily mean of the MODIS and ASI SIC, the pixel-wise standard deviation of all overflights for all three datasets, the number of available measurements for each pixel for all three datasets, and the number of cases where MODIS and ASI SIC are available is saved internally and will be made available publicly in future, together with the uncertainty estimates derived in section 4.3 and presented in section 6.4. A flow chart which visualises the processing

chain is shown in Fig. 4.3. The software for the processing chain is available and maintained in a git repository at <https://gitlab.seaice.physik.uni-bremen.de/vludwig/cronjob-for-merged-sea-ice-concentration> (last access October 7, 2020).

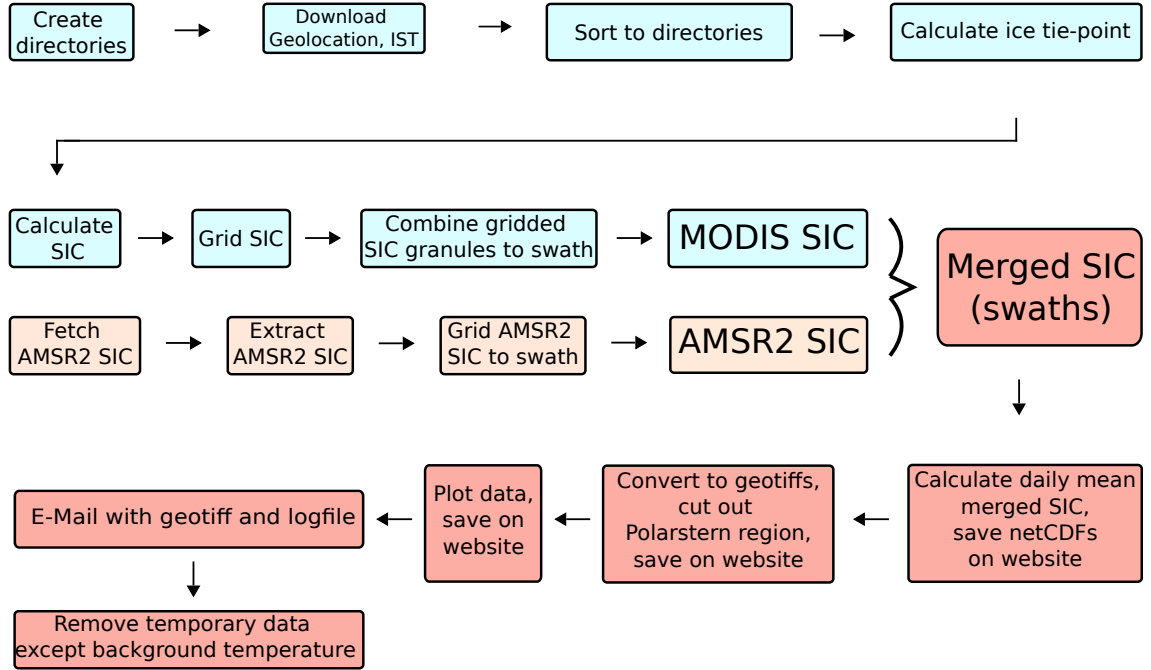


Figure 4.3.: Flowchart of operationally implemented processing chain.

4.3. Uncertainty estimates

4.3.1. MODIS sea-ice concentration uncertainty

Several uncertainty-afflicted parameters enter the MODIS sea-ice concentration retrieval. Their individual uncertainties all contribute to the uncertainty of the MODIS sea-ice concentration. The MODIS sea-ice concentration uncertainty, $\sigma_{SIC_{MODIS}}$ is, given by Gaussian error propagation applied to equation 4.2:

$$\sigma_{SIC_{MODIS}} = \sqrt{Unc_{IST} + Unc_{tp_{water}} + Unc_{tp_{ice}}} \quad (4.5)$$

with the respective uncertainty contributions

$$Unc_{IST} = \left(\frac{1}{tp_{ice} - tp_{water}} \right)^2 \sigma_{IST}^2 \quad (4.6)$$

$$Unc_{tp_{water}} = \left(\frac{IST - tp_{ice}}{(tp_{ice} - tp_{water})^2} \right)^2 \sigma_{tp_{water}}^2 \quad (4.7)$$

$$Unc_{tp_{ice}} = \left(\frac{tp_{water} - IST}{(tp_{ice} - tp_{water})^2} \right)^2 \sigma_{tp_{ice}}^2 \quad (4.8)$$

Here, we assume that $\sigma_{tp_{water}}$ and σ_{IST} , the respective uncertainties of tp_{water} and IST , are equal to the measurement uncertainty of the MODIS ice-surface temperature which amounts to 1.3 K (Hall et al., 2004). The effect of salinity variations on tp_{water} is negligible, as will be shown in section 5.3. For $\sigma_{tp_{ice}}$, we assume that it is equal to the standard deviation of the 48 iterations done for the retrieval of ice tie-point in section 4.1. It is typically between 0.1 and 0.6 K (see Fig. 5.6 d).

4.3.2. Merged sea-ice concentration uncertainty

If MODIS data are available, the first case in equation 4.4 needs to be considered and the merged sea-ice concentration at the pixel with the coordinates (i,j) is given by:

$$SIC_{merged_{i,j}} = SIC_{MODIS_{i,j}} + SIC_{ASI_{5km}} - SIC_{MODIS_{5km}} \quad (4.9)$$

$SIC_{MODIS_{i,j}}$ and $SIC_{MODIS_{5km}}$ are two samples of the same dataset, only that $SIC_{MODIS_{5km}}$ is the average MODIS SIC in the 5 by 5 km around the pixel at the coordinates (i,j). We thus consider equation 4.9 as a linear combination of the MODIS and ASI SIC and calculate the uncertainty as

$$\sigma_{SIC_{merged}} = \sqrt{Unc_{MODIS} + Unc_{ASI}} \times \frac{1}{\sqrt{2}} \quad (4.10)$$

with the respective uncertainty contributions

$$Unc_{MODIS} = \sigma_{SIC_{MODIS}}^2 \quad (4.11)$$

$$Unc_{ASI} = \sigma_{SIC_{ASI}}^2. \quad (4.12)$$

Since SIC_{MODIS} and SIC_{ASI} are retrieved from different wavelength regimes and by different approaches, we consider them as independent observations of the same quantity and thus scale the uncertainty by $\sqrt{2}$.

Now, we need the uncertainty of the ASI sea-ice concentration. This uncertainty is adopted from Spreen et al. (2008) and expressed as a function of the sea-ice concentration (see Fig. 4.4). If MODIS data are not available for the merging, the uncertainty is equal to the ASI SIC uncertainty.

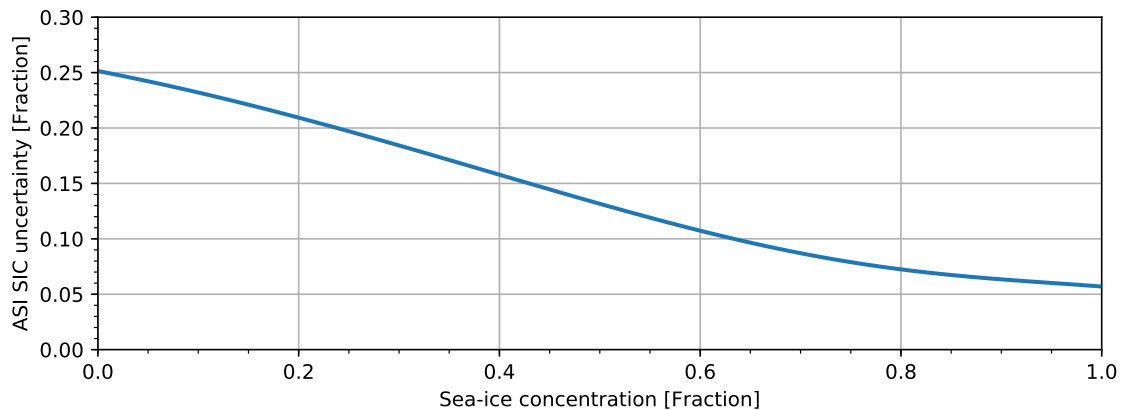


Figure 4.4.: Uncertainty of the ASI SIC as derived by Spreen et al. (2008).

4.4. Evaluation

4.4.1. Sentinel-2 and Landsat 8 sea-ice concentration

For the evaluation, a reference SIC dataset based on Sentinel-2 and Landsat 8 reflectances has been constructed. We classify the Sentinel-2 reflectances according to their frequency of occurrence shown in Fig. 4.5 a (see below). The three bands from the visible spectrum (bands 2, 3, 4) are investigated. We evaluate histograms of all 3 bands (red/665 nm, green/560 nm, blue/490 nm) for all 79 Sentinel-2 scenes. They show no notable difference for our purpose, all three bands enable a clear distinction between the thin and thick ice classes if both classes are present and a clear distinction between ice and water if only thick ice is present. We decide to use band 4 (red/665 nm).

The reflectances are classified into three classes: open water, thin ice and thick ice. Since the ice peaks differ from scene to scene (Fig. 4.5 a), we select specific thresholds for each scene instead of using a global threshold for all scenes. If there were two peaks at the high end of the reflectance spectrum, both were treated as ice. A distinction between thin and thick ice is possible for 50 scenes, i. e., 63%. In theory, a sea-ice concentration product should retrieve ice as ice, regardless of its thickness. However, the ice thickness still influences the sea-ice concentration retrieval from passive microwave data (Wiebe et al., 2009) and thermal infrared data (Ludwig et al., 2019, 2020) and for a number of applications, e. g. the ocean-atmosphere heat flux, the ice thickness is relevant.

We create two reference SIC datasets: One for which the thin ice class is treated as ice and one for which it is treated as water. The SIC dataset where the thin ice is treated as water is called thick-ice SIC as it comprises only thick ice. Consequently, the SIC dataset for which also thin ice is treated as ice is called thin-ice dataset as it comprises thin and thick ice.

The resolution of the binarised ice/water maps is 10 m and the desired resolution of the SIC dataset is 1 km. Thus, we assume that one SIC pixel (1 km) comprises 100 by 100

reflectance pixels. We select each pixel in the SIC array and assign it with the average of the surrounding 100 by 100 reflectance pixels, assuming that the SIC pixel is in the center of the box. In this way, we obtain a SIC dataset at 1 km resolution from the 10 m reflectance dataset.

The Landsat 8 reference SIC are calculated in a similar manner as the Sentinel-2 reference SIC, except that we do not construct a thick-ice dataset. The central wavelength of the red band of Landsat 8 is 655 nm. The histograms for the Landsat 8 reference SIC are shown in Fig. 4.5 b. The pixel size of a Landsat 8 pixel is 30 m, so that one SIC pixel comprises 33 by 33 reflectance pixels.

4.4.2. Open water extent

We want to show the benefits of the higher resolution of the merged SIC compared to the ASI SIC. The mean SIC for both datasets is identical by definition. However, the finer resolution of the merged product results in sharper gradients, e. g. at the edges of leads. To show this effect, we calculate the open water extent for both datasets. It is defined as the area covered by all pixels which have at least 15 % open water. Due to its finer spatial resolution, the merged SIC are expected to have a higher open water extent than the ASI SIC.

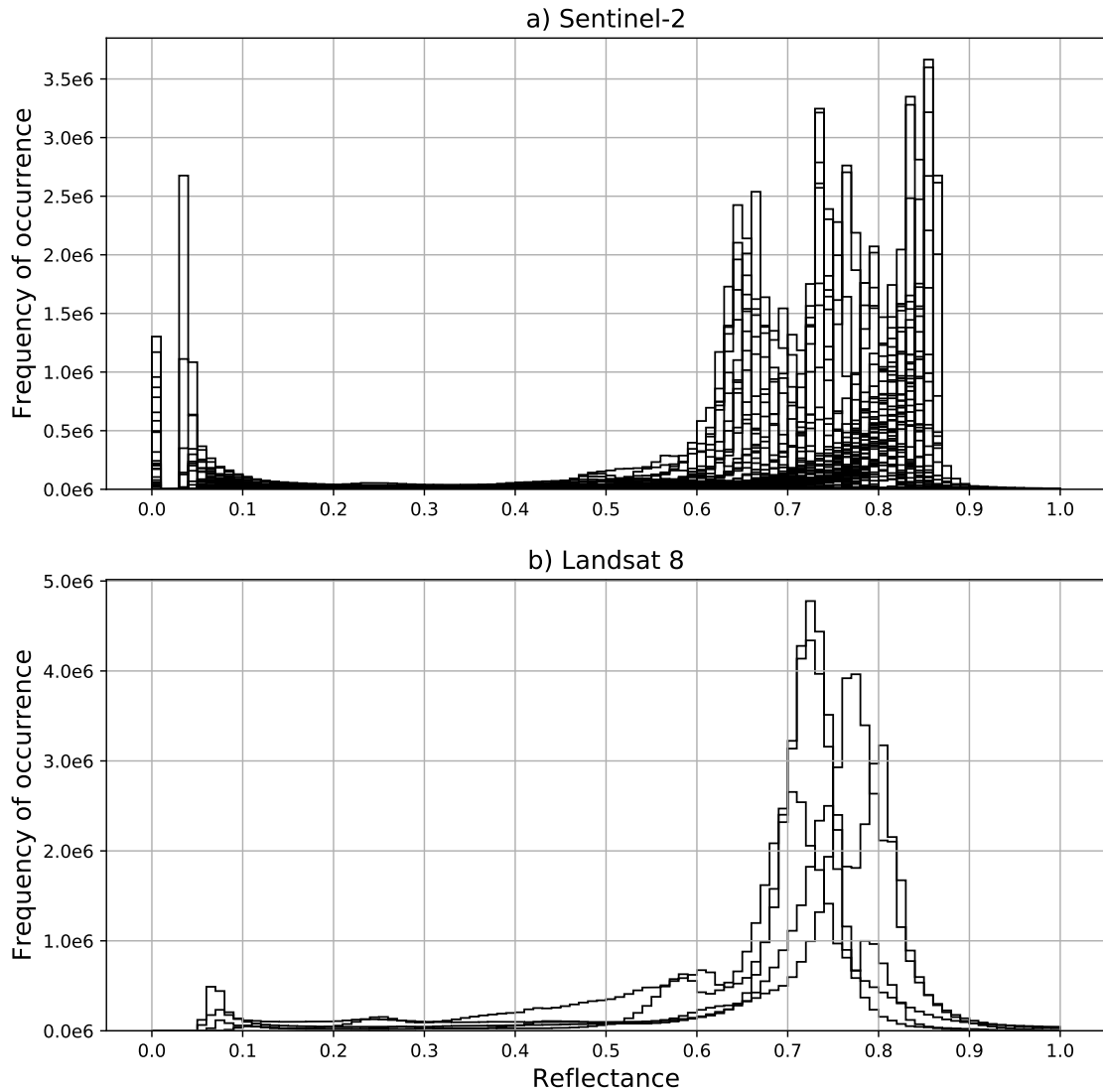


Figure 4.5.: Frequency distributions of the reflectances used for constructing the reference SIC datasets. a) All 79 Sentinel-2 scenes. The band shown is band 4 (red/665 nm). b) All 5 Landsat 8 scenes. The band shown is band 4 (red/655 nm). The x-axis shows the reflectances with a binsize of 0.01 for both panels, the y-axis gives the frequency of occurrence in absolute values.

5. MODIS sea-ice concentration

The main difference between the MODIS sea-ice concentration in our study and Drüe and Heinemann (2004), where the MODIS sea-ice concentration was first presented, is the smoother ice tie-point field. As described in section 4.1, the ice tie-point is calculated 48 times for each pixel and the average is adopted as final ice tie-point. This chapter presents the smoother ice tie-point field and the effect which this has on the MODIS sea-ice concentration. Furthermore, we compare the strict cloud mask which we apply in our study to the more conservative cloud mask which is applied in the original version of the MODIS ice-surface temperature product. Last, we derive an ice tie-point threshold for meaningful sea-ice concentration retrieval and briefly compare MODIS to ASI sea-ice concentration. The results are discussed in section 5.6. Parts of this chapter, namely the sections 5.2–5.4, are published in Ludwig et al. (2020).

5.1. Improvement of ice tie-point retrieval

The MODIS ice tie-point is retrieved based on the ice-surface temperature variability within a region of 48 km by 48 km. A set of coefficients is derived by linear regression to assign each pixel within this region its own ice tie-point. In the original publication, Drüe and Heinemann (2004) shift the region by 48 km and retrieve the next set of coefficients. We choose a smaller stepsize of 1 km before repeating the calculations, so that each pixel is covered 48 times. Depending on cloud cover, this yields up to 48 possible tie-points per pixel, the mean of which is selected as final ice tie-point (see section 4.1).

Figure 5.1 shows the tie-points retrieved with a stepsize of 48 km as in Drüe and Heinemann (2004), compared to the tie-points retrieved with a stepsize of 1 km. When choosing a stepsize of 48 km, the coefficients for the linear regression change abruptly after shifting the box used for the tie-point retrieval. This introduces sharp edges in the tie-point field, so that the 48-km-by-48-km box is clearly visible in Fig. 5.1 b. Since the ice tie-point is linearly converted to sea-ice concentration and the water tie-point is fixed, these sharp transitions propagate directly into the MODIS sea-ice concentration (see Fig. 5.1 d, e). The sharp edges are smoothed by our approach. Figure 5.1 c and f show that this yields a much smoother ice tie-point and sea-ice concentration field. The difference map in Fig. 5.1 e shows that the differences between the two approaches are up to $\pm 5\%$ sea-ice concentration in this example.

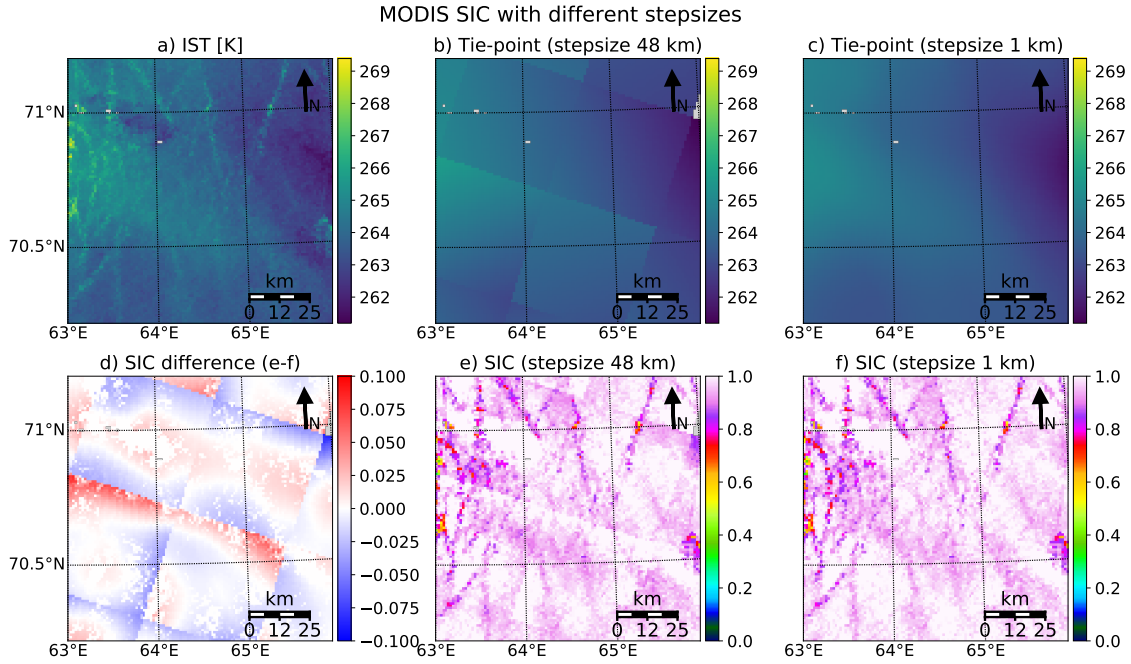


Figure 5.1.: MODIS sea-ice concentration with different ice tie-point fields in a scene in the Kara Sea on April 29, 2019 at 07:20 am (UTC). a) Ice-surface temperature field which is converted into sea-ice concentration. b) Ice tie-points calculated with a stepsize of 48 km. c) Ice tie-points calculated with a stepsize of 1 km. d) Difference between the sea-ice concentration retrieved with the ice tie-points of panels b and c. e) sea-ice concentration based on the ice tie-points from panel b. f) sea-ice concentration based on the ice tie-points from panel c.

To assess this further, we analysed 66 selected MODIS granules (see section 3.1.1 to see how they were selected). In Fig. 5.2, we show the differences between neighbouring pixels, sorted by ascending difference for different stepsizes. They have been normalised to the largest difference of the stepsize 48 km. For the majority of the pixels (approximately 95%), the difference does not depend on the stepsize. This is expected as only the differences at the edge between two adjacent boxes change, i. e., only every 48th pixel for a stepsize of 48 km. However, for the highest approximately 5%, the differences decrease with smaller stepsizes. Also, Fig. 5.2 shows that the coverage (number of pixels for which an ice tie-point has been retrieved) increases for smaller stepsizes. The reason is that a certain amount of cloud-free pixels must be present within the 48-km-by-48-km box (see section 4.1), otherwise no tie-point is retrieved for the entire box. Shifting the region with a smaller stepsize increases the likelihood that a pixel lies within a region with sufficient cloud-free pixels at least once and thus increases the coverage of the ice tie-point field. The coverage increases most strongly between the stepsizes 48 and 24 km and not as pronounced for the other stepsizes. For 12 km, 6 km and 1 km, the coverage is almost identical. The curve for the stepsize 1 km increases most steeply towards the end, which

5. MODIS sea-ice concentration 5.1. Improvement of ice tie-point retrieval

means that it has the smallest amount of large pixel-to-pixel differences, even though the largest difference is smaller for the stepsize of 12 km. There is another argument for choosing 1 km as final stepsize. The standard deviation of all possible tie-points for one pixel will later be used as an estimate for the tie-point uncertainty. For this, an ensemble of up to 48 possible tie-points (stepsize 1 km) is expected to be a more representative estimate than an ensemble of 8 (stepsize 6 km) or 4 (stepsize 12 km) possible tie-points. We thus decide for 1 km as stepsize for the ice tie-point retrieval.

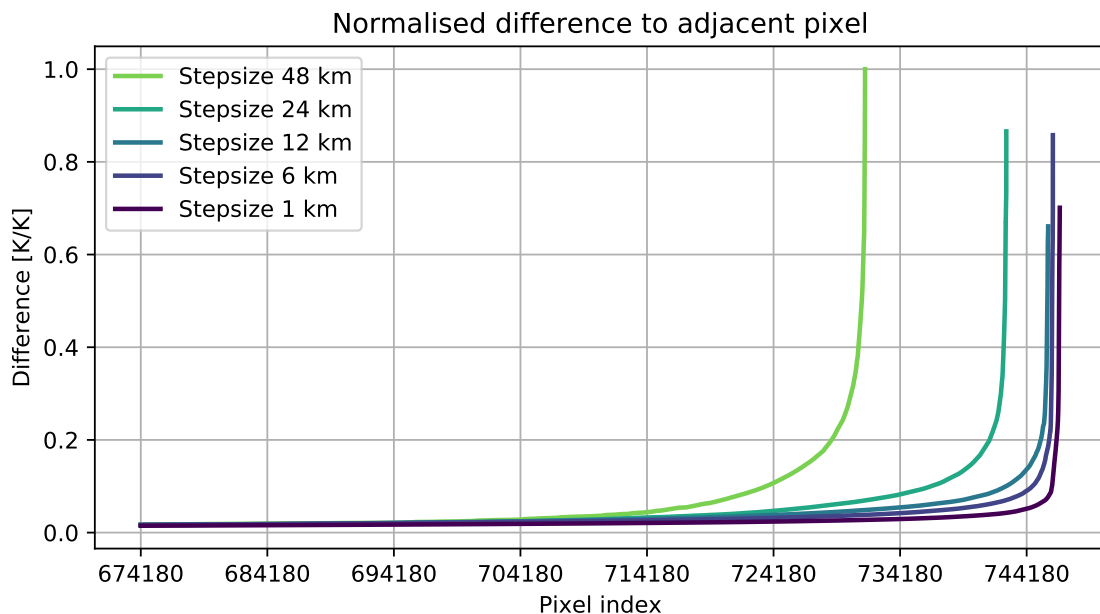


Figure 5.2.: Difference between adjacent pixels for the ice tie-points of 66 MODIS granules, sorted by ascending difference. The MODIS granules are selected as described in subsection 3.1.1. The x-axis gives the index of the pixel in the sorted array, starting at the 90th percentile of the cloud-free pixels. The y-axis gives the difference, normalised by the magnitude of the differences with a stepsize of 48 km. The curves show the differences for different stepsizes (see legend for details).

To quantify how much choosing a smaller stepsize impacts the final sea-ice concentration, we calculate the root mean square deviation (RMSD) between the sea-ice concentration retrieved with a stepsize of 48 km and the sea-ice concentration retrieved with a stepsize of 1 km and show the result in Fig. 5.3. We see in Fig. 5.3 a that the RMSD is beneath 2% except for one occasion if the ice tie-point is smaller than 260 K. It increases up to 4% for ice tie-points beneath 268 K and can be more than 14% for ice tie-points above 268 K. We will show in section 5.3 that the ice tie-point increases between mid March and May (see Fig. 5.6). This also means that the RMSD increases with time, as is shown in Fig. 5.3 b. The cases with RMSDs beneath 2% are all before April 18, with one exception.

5.1. Improvement of ice tie-point retrieval 5. MODIS sea-ice concentration

Afterwards they increase to up to 4% until May 18. The RMSDs with higher values (up to 14%) are all after May 18. We explain the increase of the RMSD's with time by the decreasing dynamic range, i. e., the ice tie-point and the water tie-point are closer together in spring. This makes the sea-ice concentration more susceptible to small ice tie-point variations.

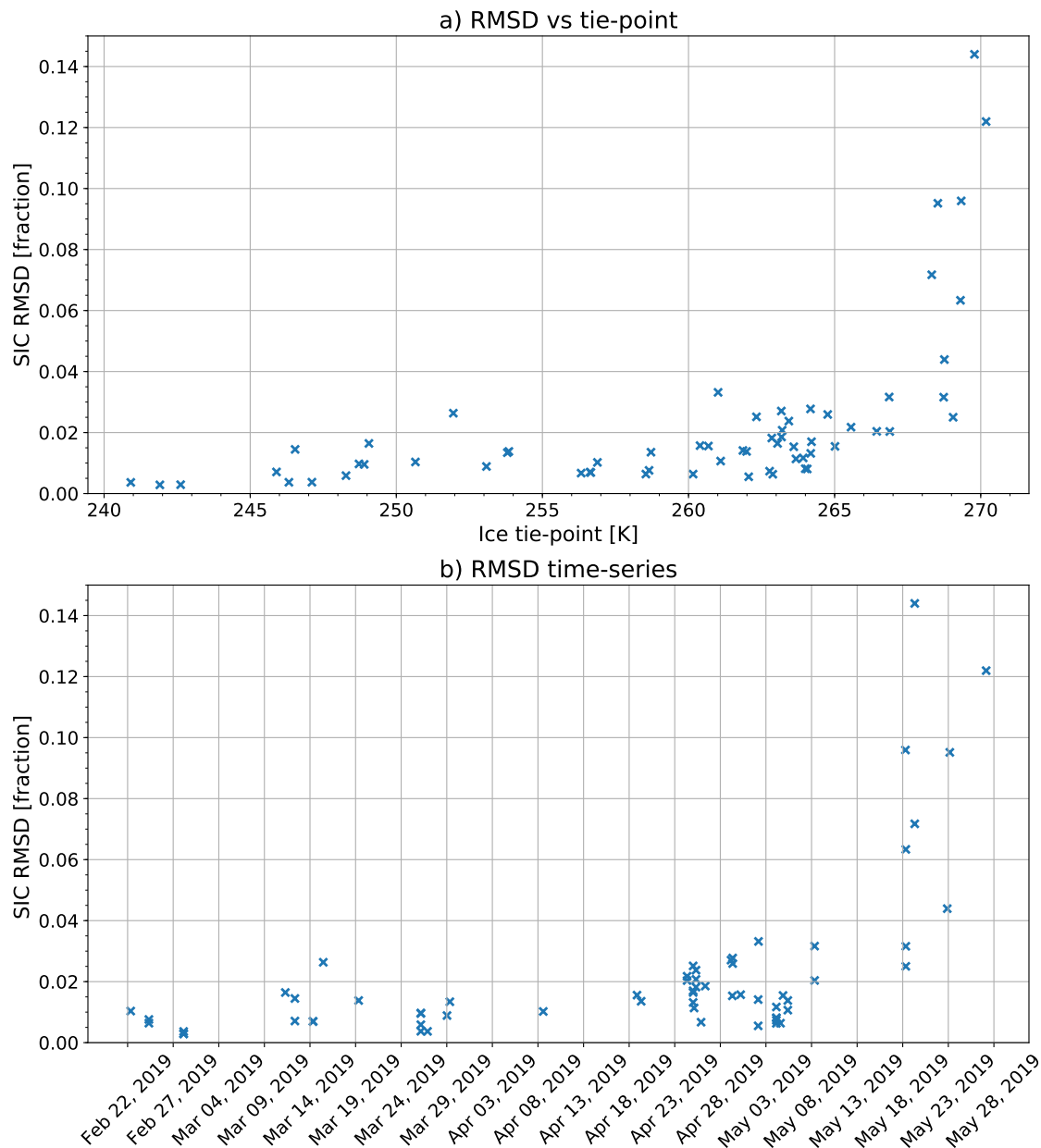


Figure 5.3.: RMSD between sea-ice concentration retrieved with a stepsize of 48 km and a stepsize of 1 km. a) Plot of the RMSD versus the ice tie-point. b) Timeseries of the RMSD. The MODIS granules have been selected as described in subsection 3.1.1.

5.2. Cloud mask

When creating the MODIS ice tie-point timeseries presented in Fig. 5.4, we noticed that a small number of clear-sky pixels often coincides with a high ice tie-point (not explicitly shown). We explain this partly by the clear sky allowing direct heat loss from the surface to the Universe, while clouds reflect the longwave radiation, thus keeping the surface warmer. Furthermore, there is enhanced evaporation and thus more fog and convective clouds under higher temperatures. The ice and water still might be visible through such semi-transparent clouds.

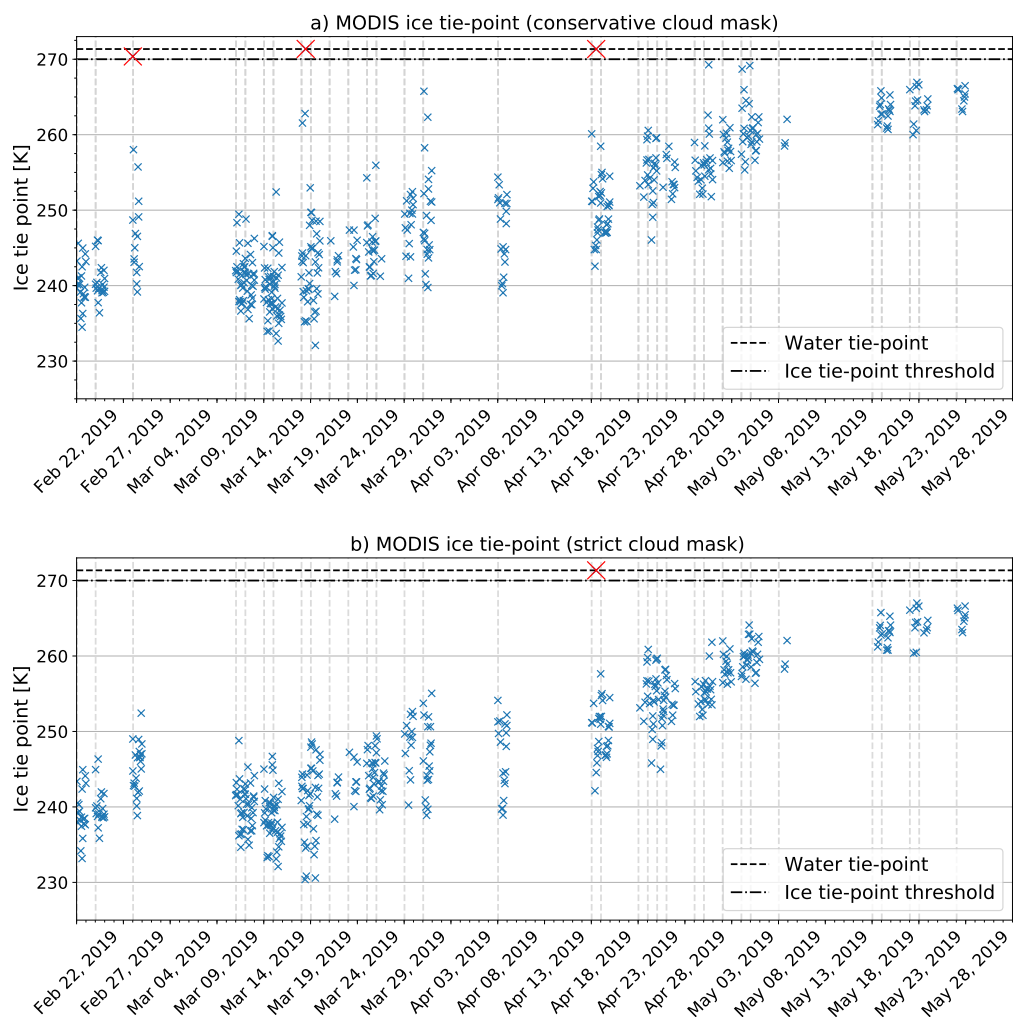


Figure 5.4.: Timeseries of the ice tie-point when applying the conservative cloud mask (panel a)) and the strict cloud mask (panel b)). The x-axis shows the date, the vertical lines mark the days with Sentinel-2 scenes. The dashed horizontal line shows the water tie-point. The dash-dotted line gives the threshold above which no sea-ice concentration is retrieved in the current version of our retrieval. The red crosses mark the granules above this threshold.

High ice tie-points are problematic for the retrieval because they decrease the dynamic range and thus increase the susceptibility to small ice-surface temperature variations. These cloud and fog features often also are patchy and thus the high ice tie-point is not representative for a larger area. We therefore omit granules with less than 20 % clear-sky pixels for this part of our study. This leaves us with 478 of the originally 997 granules (see subsection 3.1.1) which amounts to 47 %. Since the discarded granules are mostly cloud-covered anyway, we only discard 20 % of the cloud-free pixels. Using the conservative cloud masking (see subsection 3.1.1) would result in 519 available granules (52 %) and also 20 % of discarded pixels. The effect of the stricter cloud mask is presented in Fig. 5.4. The time series of the strictly masked data shows less outliers than that of the conservatively masked data. This happens because the high spikes in the conservatively masked time series occur when most of the granule is cloud-covered, as described above. Then, a small number of additionally discarded pixels is enough to violate the criteria which must be met for the tie-point retrieval to be performed (see section 4.1). For example, the high tie-point on April 18th (red cross in Fig. 5.4 b) occurs when the retrieval is performed in only one iteration. This also explains why the standard deviation is 0 for this granule (see Fig. 5.6 d).

Generally, the number of discarded pixels increases with time (see Fig. 5.5 a). The amount of pixels which are only discarded by the strict cloud mask, however, decreases with time (see Fig. 5.5 b). In February and early March, the number of pixels discarded by the strict cloud mask is up to twice as high as the number of pixels discarded by the conservative cloud mask. In fact, all cases in which more than 20 % are discarded additionally are in February and March, with only one exception. In February, on average 66.4 % of a MODIS granule are discarded when applying the conservative cloud mask, while 74.0 % of a granule are discarded on average if the strict cloud masking is applied (not explicitly shown). This corresponds to a relative increase of 11.5 % when applying the stricter cloud mask. In May, on average 81.9 % of the MODIS granules are covered by clouds when applying the conservative cloud mask and 83.7 % when applying the strict cloud mask, which means a relative increase of 1.8 % by using the stricter cloud mask. We explain this by the limited presence of low, thick clouds in the early months of the year (Taylor et al., 2019; Yu et al., 2019). Therefore, the cloud cover is dominated by the presence of thin high clouds whose seasonal cycle is less pronounced (Eastman and Warren, 2010). These are more challenging to detect and thus more likely to be flagged 'probably clear' or 'probably cloudy'. These flags are discarded by the stricter cloud mask, but not by the conservative cloud mask. Furthermore, there are more clouds in summer than in winter (see Fig. 5.5 a), so that it is more likely that large parts of the granule are covered by clouds and there is not much room for discarding pixels additionally. We judge the number of discarded pixels as an acceptable trade-off for the reduced variability and outliers and thus adopt the stricter cloud mask.

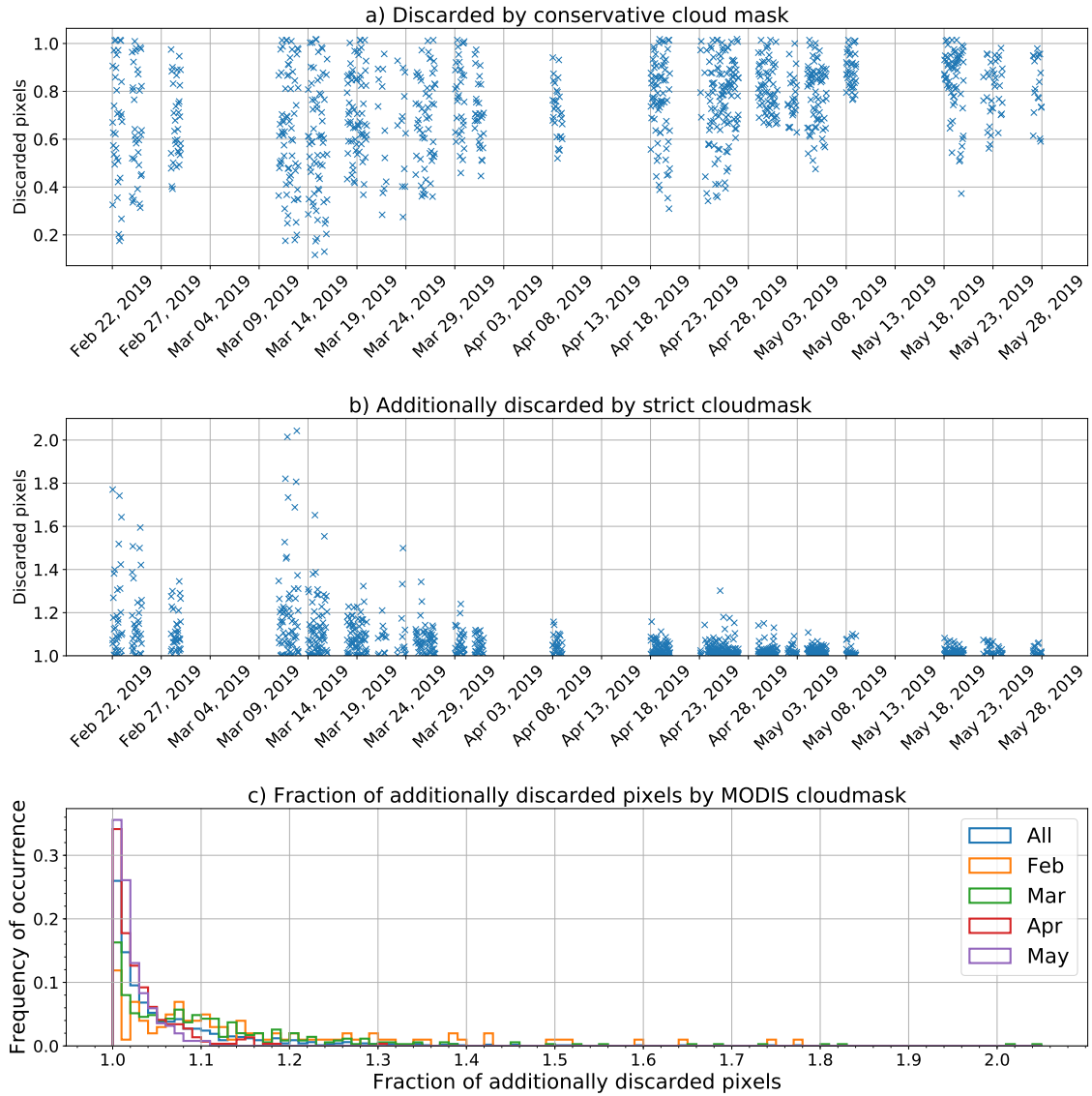


Figure 5.5.: Comparison of strict and conservative cloud mask. a) shows how many pixels are discarded by the conservative cloud mask. b) shows a time series of the additionally discarded pixels, i. e., the number of pixels discarded by the strict cloud mask divided by the number of pixels discarded by the strict cloud mask. c) shows a histogram of the fraction of additionally discarded pixels. The histogram has been normalised such that the bins add up to 1 for each month. We show one histogram for each month and one for all months together (see legend for details). All 997 available MODIS granules have been used.

5.3. Tie-point variability

In this section, we briefly assess the validity of the assumption of a constant freezing point which we use as water tie-point. Afterwards, we focus on the analysis of the variability of

the ice tie-point.

Our retrieval assumes a constant freezing point, but in reality the freezing point varies depending on salinity. To assess the influence on this, we calculate the MODIS sea-ice concentration with freezing points of -1.09°C , which would correspond to a salinity of 20 and -1.87°C , which would correspond to a salinity of 34, using the parameterisation of Millero and Leung (1976). The average difference for all granules is 0.5%, which we judge as acceptable (see section 5.6 for further discussion).

In Fig. 5.6, we show the variability of the ice tie-point. This is done by analysing the variation of the up to 48 possible and on average 37 ice tie-point values per pixel (see section 4.1). Ice tie-points on the same day but for different overflights typically differ by 10 K but up to 20 K. This reflects the daily cycle and the spatial variability of the ice-surface temperature. Furthermore, more than one region is covered on some days (see Fig. 3.2). Adjacent granules differ by up to 10 K, which we attribute partly to spatial variability, but mainly to the different cloud cover. Even if the ice-surface temperature distribution in two adjacent granules would be identical, the mean ice-surface temperature would differ depending on which part of the respective granule is obscured by clouds.

The difference between minimal and maximal ice tie-point within one 48-km-by-48-km region is between 1 K and 2 K in February and March and slightly decreases until the end of May. We interpret this as a combination of two effects. The first is that under rising temperatures the temperature variability in our 48-km-by-48-km region is smaller than in winter. The second factor is the increased cloud cover. Since more pixels are cloud-covered in April and May, the requirements for the tie-point retrieval to be performed (see section 4.1) are violated more often, thus less of the 48 iterations actually yield a possible tie-point and therefore there is a smaller difference between minimal and maximal tie-point.

To assess the influence on our retrieval, we next look into the differences normalised to the dynamic range. This is more meaningful for our purpose since the same difference between minimal and maximal ice tie-point has a larger influence at smaller dynamic ranges and vice versa. Because the ice tie-point increases in May, the normalised difference (see Fig. 5.6 c) increases from 5% to 20% and more of the dynamic range at the end of May. This is consistent with the assumption that the retrieval yields less reliable results in summer when the ice surface temperature approaches the freezing point. We will see later in subsection 6.4.1 that the decreasing dynamic range causes the uncertainties to increase in May. This also follows from the formulation of the uncertainty estimates in the equations 4.6–4.8, where the dynamic range is the denominator of each MODIS sea-ice concentration uncertainty contributor. The mean normalised difference between the minimum and maximum tie-point for all months is 0.08. This means that choosing an arbitrary starting point for the linear regression like it is done in the original retrieval (Drüe and Heinemann, 2004) changes the resulting final ice tie-point by on average 8%. This is an upper limit of the introduced inaccuracy since it is the difference between the minimum

and maximum ice tie-point. The standard deviation of the 48 iterations gives a more representative estimate of the actual inaccuracy between the two retrievals. The mean standard deviation of all 478 granules is 0.33 K. Normalised with respect to the dynamic range, this amounts to 1.7% of the dynamic range. While the ice tie-point increases in April and May, the standard deviation in these months is lower than in February and May. We interpret this as a consequence of smaller temperature variation within the 48 km-by-48 km box used for the tie-point retrieval as the temperature approaches the freezing point. This is also consistent with the decrease of the maximal difference towards the end of the time series (see Fig. 5.6 b).

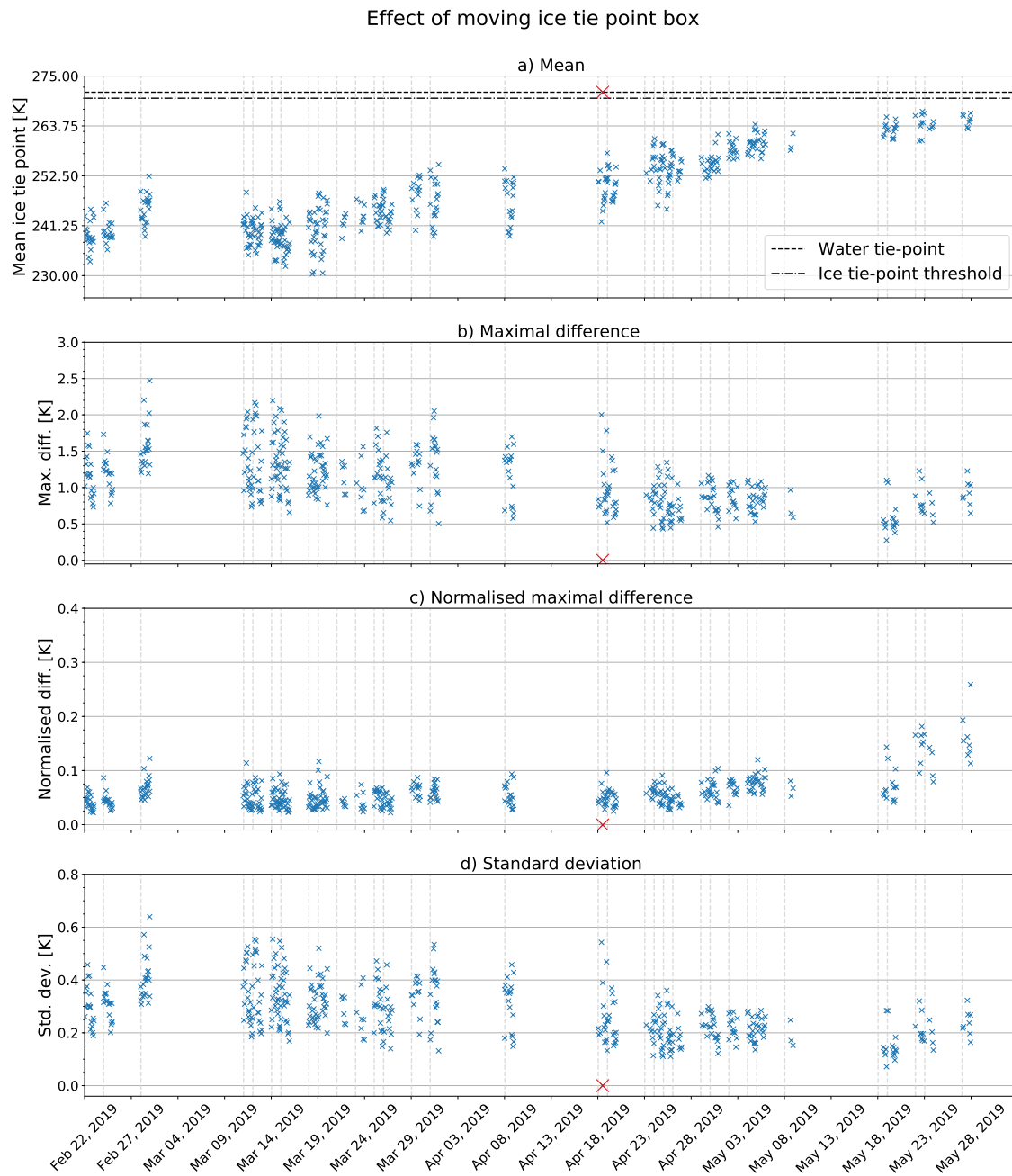


Figure 5.6.: Effect of shifting the starting position of the box used for the ice tie-point calculation. The starting position is shifted by one pixel before redoing the calculation, so that each pixel is covered 48 times. The x-axis shows the date, the vertical lines mark the days with Sentinel-2 scenes. Panel a) shows the mean of the 48 iterations, same as in Fig. 5.4 b). The dashed horizontal line shows the water tie-point. The dash-dotted line gives a discarding threshold. If the ice tie-point is above this threshold, no sea-ice concentration is derived in the current version of our retrieval. Panel b) shows the difference between the maximal and minimal ice tie-point. Panel c) also shows the maximal difference, but normalised by the dynamic range (difference between ice and water tie-point). Panel d) shows the standard deviation of the 48 iterations, also normalised by the dynamic range.

Next, we investigate how much this affects the variability of the MODIS sea-ice concentration. For this, we calculate the MODIS sea-ice concentration with the final ice tie-point plus/minus one standard deviation and show the resulting sea-ice concentration together with the difference in Fig. 5.7. The difference increases when the sea-ice concentration decreases, which we expect because a less compact sea-ice cover is naturally associated with larger variability. For example, the maximal difference of all 478 granules coincides with the third lowest sea-ice concentration. The maximal difference was 6.2%, the mean difference amounted to 1.9%. This can be interpreted as the inaccuracy introduced by the arbitrary starting point. Our approach of varying the starting position mitigates this inaccuracy as far as possible.

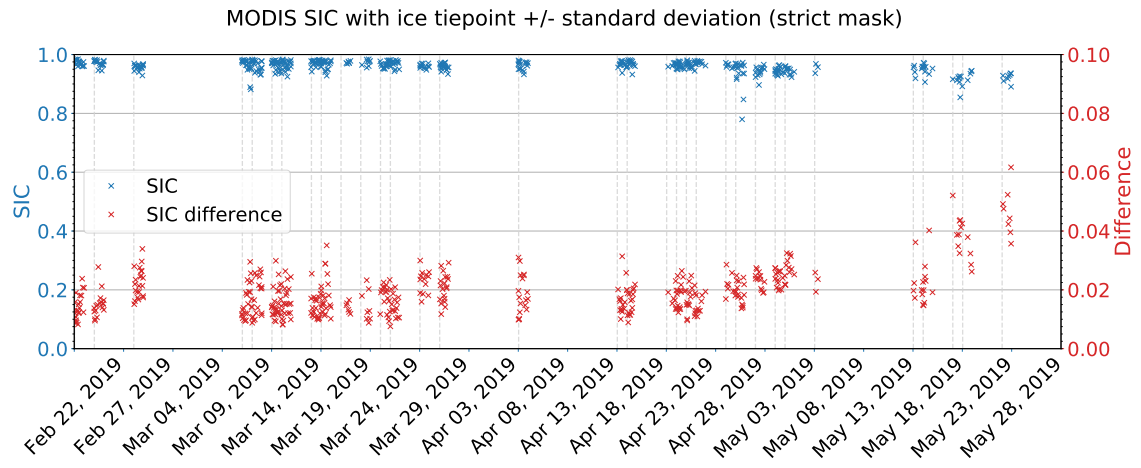


Figure 5.7.: MODIS sea-ice concentration calculated with the ice tie-point from Fig. 5.6a plus/minus the standard deviation from Fig. 5.6d. The blue dots show the sea-ice concentration. The orange dots show the difference between the MODIS sea-ice concentration resulting from varying the ice tie-point by plus/minus one standard deviation. The x-axis shows the date, the vertical lines mark the days with Sentinel-2 scenes.

5.4. Ice tie-point threshold

The MODIS sea-ice concentration uncertainties (equations 4.6-4.7) get large if the ice tie-point is close to the water tie-point. This can even lead to uncertainties which are larger than 1 in single cases. We consider a MODIS sea-ice concentration with an uncertainty of 0.3 (i. e., 30%) as the upper boundary for a meaningful sea-ice concentration. This is much larger than what one would accept as uncertainty for the final merged dataset. However, because the uncertainty of the merged sea-ice concentration gets reduced we accept higher uncertainties for the MODIS sea-ice concentration because they still can provide valuable spatial variability (see section 6.2). Since the water tie-point is fixed, we need to identify an ice tie-point threshold above which meaningful sea-ice concentrations

cannot be derived any more. To find this threshold, we investigate the uncertainties for all 997 MODIS granules for which we have Sentinel-2 scenes. We show the mean and the 99th percentile of the uncertainties for each granule in Fig. 5.8. The median has also been investigated and behaves similarly to the mean, which means that the amount of outliers is small. The parameters are shown for ice-surface temperature thresholds between 265 and 270 K, where ice tie-point values above the respective threshold are discarded.

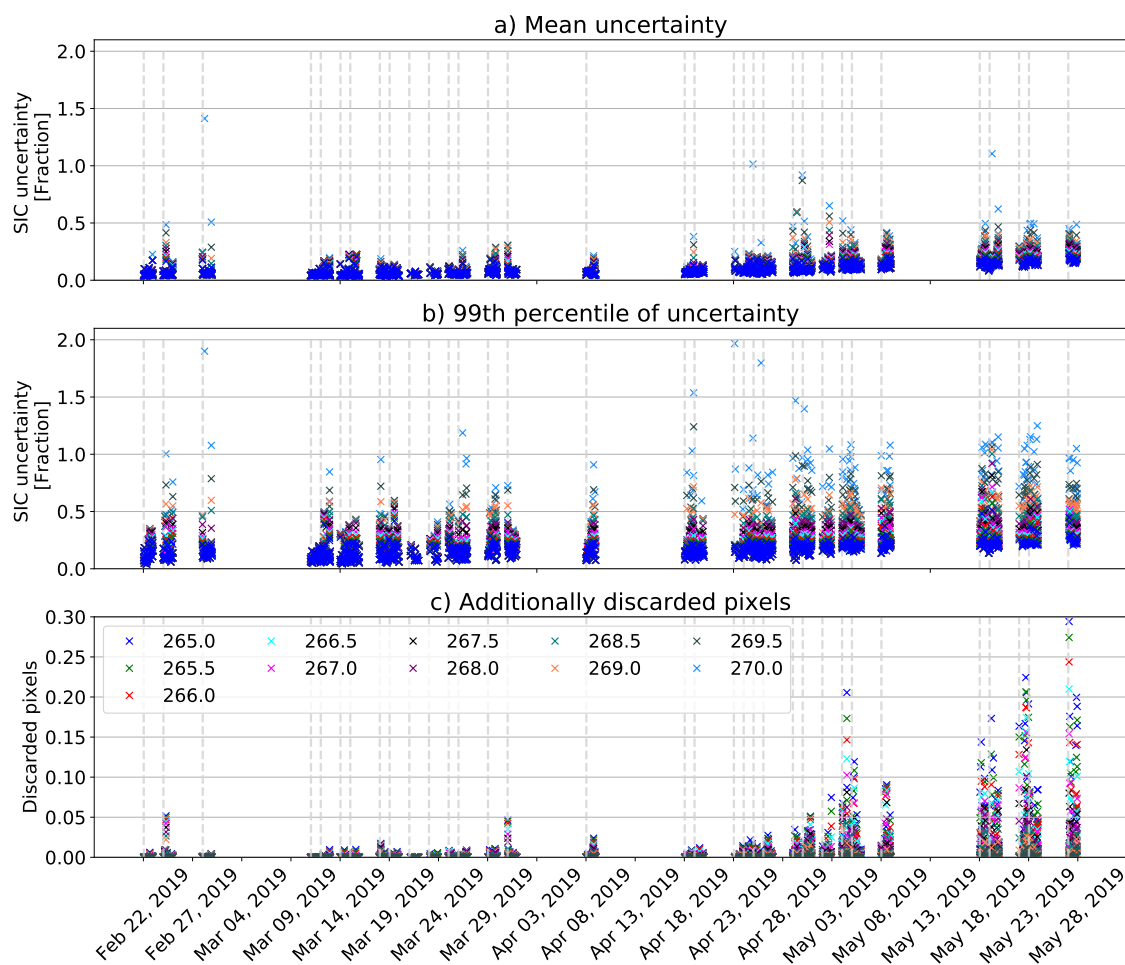


Figure 5.8.: Evaluation of the ice tie-point threshold. We show the mean uncertainties (a) and the 99th percentile uncertainties (b) per granule. Panel c) shows the 'additionally discarded values', i. e., the absolute difference between the fraction of values which would be discarded by the respective threshold and the fraction of values would be discarded by the highest threshold. The markers in the panels show the respective parameter for different thresholds between 265 and 270 K, where ice tie-point values above the respective threshold are discarded. The x-axis shows the date, the vertical lines mark the days with Sentinel-2 scenes.

We learn from Fig. 5.8 that the highest threshold, 270 K, would yield mean uncertainties above 0.3 in 69 cases, corresponding to 6.9% of all cases. A threshold of 266.5 K or lower

would have to be chosen to discard all granules with a mean uncertainty above 0.3. The time series of the 99th percentile (see Fig. 5.8 c) shows that the 99th percentile of the uncertainties exceeds our sanity threshold of 0.3 for 113 granules in May (44.7 % of the May granules), and for 169 granules before May (22.7 % of the granules before May) when applying a threshold of 269 K or higher. A threshold of 266.5 K yields 99th percentile values of above 0.3 for 32 granules before May (4.3 % of all granules before May) and for 31 granules in May (12.3 % of the May granules). The mean uncertainty does not show a trend until the end of April and then increase slightly, regardless of the threshold which is chosen. Except for some outliers, the mean uncertainties do not depend much on which threshold is chosen. This changes towards the end of the time series, when the higher thresholds exhibit a higher variability.

The final threshold will be a compromise between reducing the uncertainty as far as possible and, at the same time, keeping as many pixels as possible. Therefore, we also investigated how many pixels would be discarded by each threshold (see Fig. 5.8 c). We present the fraction of discarded pixels which would be discarded additionally to the pixels which are discarded by the highest threshold anyway. All percentages are absolute values, i. e., an increase of 10 % means an increase from, for example, 50 % to 60 %, not from 50 % to 50.5 %. Figure 5.8 d shows that applying the lowest threshold, 265 K, would result in discarding up to 30.0 % more pixels relative to the number which is discarded by the highest threshold of 270 K. However, on average (see Table 5.1), only 1.2 % of the pixels would be discarded additionally by the lowest threshold. As expected, the number of additionally discarded pixels increases in May due to the enhanced presence of clouds. This shows that our retrieval is expected to perform less reliably in May than in the other months, but we can be confident that the performance will be stable at least until the end of April.

In summary, Fig. 5.8 shows that a threshold of 266.5 K or lower needs to be chosen to ensure that the mean uncertainty is below our sanity threshold of 0.3 for all granules. At the same time, thresholds lower than 266.5 K would lead to discarding a high number (15-30 %) of pixels in May. We thus adopt a threshold of 266.5 K.

Table 5.1.: Number of additionally discarded pixels for each threshold, normalised to the number of pixels in one MODIS granule. „Additionally discarded“ means the increase in the number of discarded pixels compared to the number of pixels which the highest (i. e., most conservative) threshold, 270 K, would have discarded. The numbers are absolute percentage values, i. e., an additionally discarded fraction of 0.3 % for the lowest threshold, 265 K, in February means an increase from 77.2% of all pixels to 77.5 %. For the highest threshold of 270 K the absolute percentage values of discarded pixels are given.

Threshold	265.0	265.5	266.0	266.5	267.0	267.5	268.0	268.5	269.0	269.5	270
n_{feb}	0.3	0.3	0.3	0.2	0.2	0.2	0.1	0.1	0.1	0.0	77.2
n_{mar}	1.3	1.1	0.9	0.7	0.6	0.4	0.3	0.2	0.1	0.1	77.2
n_{apr}	0.3	0.2	0.2	0.1	0.1	0.1	0.0	0.0	0.0	0.0	73.8
n_{may}	3.0	2.6	2.2	1.8	1.4	1.0	0.7	0.5	0.3	0.1	82.6
n_{all}	1.2	1.0	0.9	0.7	0.6	0.4	0.3	0.2	0.1	0.1	77.6

5.5. Comparison to ASI SIC

Having introduced the MODIS sea-ice concentration, this section is dedicated to a brief comparison to sea-ice concentration derived by ASI, the passive-microwave based sea-ice concentration algorithm which is used in this thesis. This shall highlight the differences between the two approaches, motivating the development of the merged sea-ice concentration which is presented in Chapter 6. Figure 5.9 shows the Arctic-wide MODIS and ASI sea-ice concentration in January and May 2020.

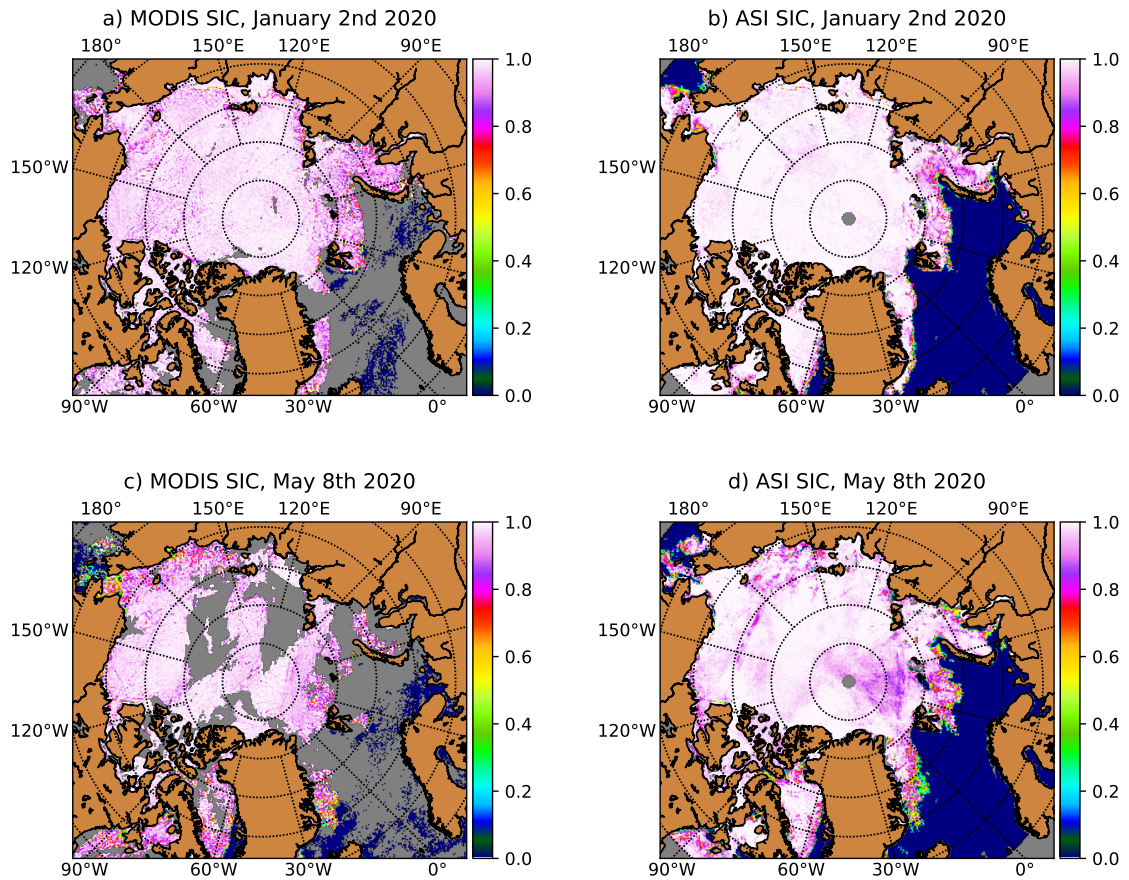


Figure 5.9.: Arctic-wide sea-ice concentration maps of MODIS and ASI sea-ice concentration on January 2nd, 2020 (panels a and b) and on May 8th, 2020 (panels c and d).

In most places, the sea-ice concentration retrieved from MODIS data is smaller than that retrieved by ASI. This can, in part, be explained by the more pronounced sensitivity to the ice thickness of the MODIS data. This causes overfrozen leads that are retrieved as 100% sea-ice concentration by ASI to show up as reduced sea-ice concentration in the MODIS sea-ice concentration. The question whether it is advantageous to retrieve overfrozen leads as reduced sea-ice concentration will be discussed in detail later (e.g., section 7.5). Furthermore, the design of the MODIS ice tie-point retrieval may lead to an underestimation of the sea-ice concentration. The ice tie-point is retrieved based on the temperature anomaly within a region of 48 km by 48 km (see section 4.1). If there are two ice thickness classes in this region, one which is thin enough for the ice-surface temperature to be influenced by the oceanic heat flux at the ice-water interface and one which is thick enough to not be influenced by this heat flux, the former will be retrieved as reduced sea-ice concentration. This will be discussed in detail later (e.g., sections 6.5 and 7.5).

Apart from the partly different magnitude where both datasets are available, Figure 5.9

also shows that MODIS sea-ice concentration are available almost exclusively over the ice and almost no values are retrieved over open water. Also over the ice, cloud-free measurements were not available for all pixels (see, e. g., the region around Greenland in Fig. 5.9 a). Between October 2019 and May 2020, when the Arctic-wide MODIS sea-ice concentration was retrieved operationally, more than 60 % of the pixels were cloud-free at least once per day on 84 % of the days. The cloud cover is less pronounced in winter than in summer. This is reflected in Fig. 5.9 c), where many more pixels are masked out compared to Fig. 5.9 a). Note that days with comparably little cloud cover have been selected for both examples. The magnitude of the MODIS sea-ice concentration does not change much between winter (Fig. 5.9 a) and summer (Fig. 5.9 c). We explain this by the dynamically adapted ice tie-point. ASI retrieves lower sea-ice concentration values in summer, but they are still available Arctic-wide without cloud gaps. The pattern of sea-ice concentration around 85 % north of Svalbard in Fig. 5.9 d), however, may be caused by atmospheric influences as described by Lu et al. (2018).

In summary, both datasets have advantages and deficiencies: The MODIS sea-ice concentration has a finer spatial resolution and allows better lead retrieval, but is more sensitive to the ice thickness and only available for cloud-free scenes. The ASI sea-ice concentration has a coarser spatial resolution, but is available independently of cloud cover. This motivates the development of the sea-ice concentration dataset which is presented in this thesis, incorporating the mutual benefits of the MODIS and ASI sea-ice concentration.

5.6. Discussion

Decreasing the stepsize for the ice tie-point retrieval as shown in section 5.1 is advantageous because of the smoother ice tie-point field and because it increases the spatial coverage. However, it also increases the runtime of the processing by a factor of 48 and makes the ice tie-point calculation one of the most time-consuming components of the operational processing chain (see subsection 4.2.1). For example, processing all granules north of 60 °N on October 17, 2020, took 37 minutes on a 32-core computer. The runtime increases to more than 50 minutes in mid-winter when more cloud-free MODIS pixels are available. Keeping the stepsize of 48 km would thus reduce the processing time of the ice tie-point calculation by a factor of 48 to between one and two minutes. The runtime of the entire processing chain is between two and two and a half hours, so that it would be reduced by approximately 25 %. However, the dataset is only available with 25 hours latency since the processing for one day can only start in the late evening of the next day, so that saving 30-45 minutes would not make a big difference concerning the time when the dataset is available. Therefore, we accept this as a trade-off to benefit from the smoother ice tie-point field and the increased spatial coverage.

The quality of the MODIS sea-ice concentration which we present in this chapter depends crucially on the reliability of the cloud screening, which we assess in section 5.2. Specifi-

cally, the MODIS cloud mask does not always identify thin clouds and fog correctly (Hall et al., 2004). We account for this by masking clouds strictly by only tolerating pixels which are flagged 'confident clear'. This means that the confidence in the pixel being cloud-free is more than 99% (Ackerman et al., 1998). Even better cloud screening might be achieved with the Fuzzy Cloud Artifact Filter proposed by Willmes and Heinemann (2015), but using the MODIS cloud mask (GSFC, 2020a) alone, this is the best we can do for cloud screening. Additionally, the merging procedure makes sure that even if there are unscreened clouds, the quality of the merged sea-ice concentration is not much worse than that of the passive microwave sea-ice concentration which we use for the merging, as we will show in section 6.3.1 and Fig. 6.10.

Calculating the MODIS sea-ice concentration, we find in section 5.3 that changing the freezing point from -1.87°C to -1.09°C (corresponding to salinities of 34 and 20, respectively) only introduces a mean difference of 0.5%. A salinity of 20 is the lower limit of what one would expect for the marginal seas (Zatsepin et al., 2010). It is higher in the Central Arctic, so that the small mean difference of 0.5% is already an upper limit of the actual error. Drüe and Heinemann (2005) find an even lower sensitivity of 0.2%. We thus consider the error introduced by the assumption of a constant freezing point as negligible. In brackish-water seas like the Baltic Sea with typical salinities between 5 and 8 (e.g., Vuorinen et al. (2015)), the water tie-point should be adapted to the lower salinities, but can still be assumed to be constant. Furthermore, we derive an ice tie-point threshold of 266.5 K as an upper limit for sea-ice concentration retrieval with acceptable uncertainties in section 5.4. Using this threshold in future instead of the 270 K threshold which is used in this thesis makes sure that the dynamic range is large enough to be robust against small freezing point variations.

For evaluation, Drüe and Heinemann (2005) compare the MODIS sea-ice concentration with sea-ice concentration derived from aircraft measurements and find an error of $\pm 10\%$ in April. Comparison with SSM/I data, also done by Drüe and Heinemann (2005), yields a linear regression error of $\pm 7\%$. The MODIS sea-ice concentration uncertainties derived by us in section 5.4 are on average lower than the ones from Drüe and Heinemann (2005), but are larger (up to 20%) in some cases. In May, they range from 10% to 35%, i.e., they are larger than the ones in Drüe and Heinemann (2005). However, since the values in April agree rather well, we conclude that our MODIS sea-ice concentration uncertainty estimates are in the range of what we expect from the literature.

The increasing MODIS sea-ice concentration uncertainty in May might be seen as an argument for stopping the retrieval already in April. However, our approach to not retrieve MODIS sea-ice concentration for ice tie-points above 266.5 K should keep the sea-ice concentration uncertainties comparably small. Furthermore, we expect ice-surface temperatures in the marginal seas to be higher than in the Central Arctic, therefore we expect smaller uncertainties there. Thus, we judge our physically based approach as appropriate. One could argue that the retrieval could also be extended towards June, which we have

not investigated here. However, since the uncertainties are already high in May, we expect them to be even stronger in June, when the temperature rises and the surface melt increases. Furthermore, the ASI sea-ice concentration, which will later be used for the merging, are also considerably less accurate in summer (e.g. Rösel et al. (2012); Ivanova et al. (2015); Kern et al. (2020)). Therefore, we decided against the attempt to validate the performance of our product, since we do not expect reasonably accurate results. For an extension towards summer, it would be more promising to test visible data, which have even finer spatial resolutions of, for example, 250 m of MODIS's band 1.

6. Merged sea-ice concentration

In this chapter, the merged sea-ice concentration dataset is presented and evaluated. We start by introducing the single datasets, namely the merged, MODIS and ASI sea-ice concentration, and the reference datasets used for the evaluation, namely the Sentinel-2 and Landsat 8 sea-ice concentration in section 6.1. Then, we demonstrate the benefits of the merged dataset in section 6.2 and its limitations in section 6.3. The chapter concludes with a time series and evaluation of uncertainty estimates of the merged, MODIS, and ASI sea-ice concentration in section 6.4 and a discussion of the presented results in section 6.5. Parts of the chapter, specifically the subsections 6.1.2, 6.1.3, 6.2.1, 6.3.1 and section 6.4, are published in Ludwig et al. (2020).

6.1. Introduction of the datasets

This section first introduces the merged dataset and highlights the differences between the merged, MODIS and ASI sea-ice concentration. This is followed by the introduction of the Sentinel-2 and Landsat 8 reference sea-ice concentration and a time series of the merged and MODIS sea-ice concentration. Note that this section does not aim at an evaluation of the datasets in the sense of determining which dataset performs best or worst. This will be the focus of the sections 6.2 and 6.3.

6.1.1. Merged, MODIS and ASI sea-ice concentration

To introduce the merged dataset, we show a scene recorded in the Kara Sea on April 25, 2019 (see Figure 6.1).

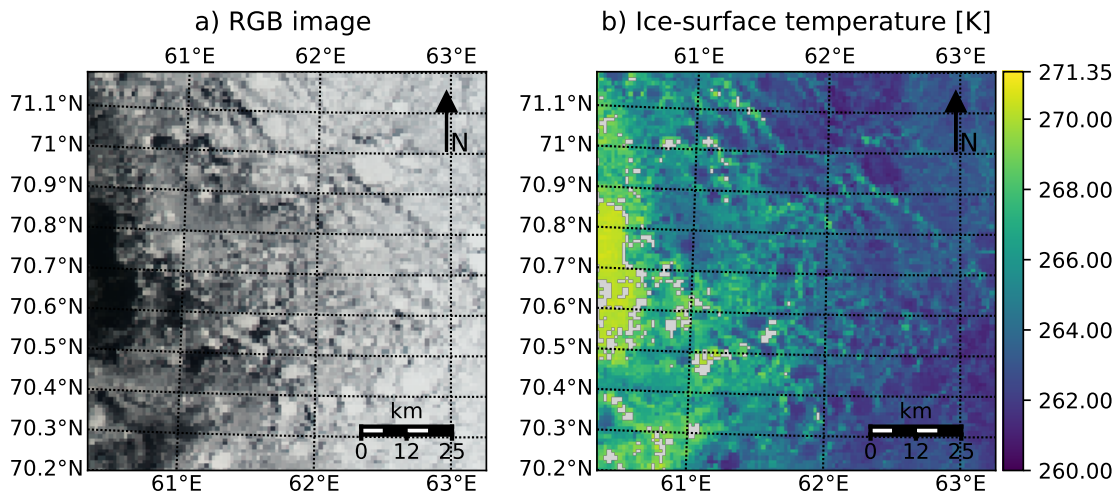


Figure 6.1.: Scene recorded in the Kara Sea on April 25, 2019 at 07:40 UTC. a) MODIS RGB image. b) MODIS ice-surface temperature. Cloud gaps are shown in grey.

In the scene in Fig. 6.1, there is open water and newly forming, thin ice in the western part of the scene, while the eastern part is dominated by larger contiguous, yet separate floes (see Fig. 6.1a). The surface temperature, which is converted to sea-ice concentration by the MODIS sea-ice concentration algorithm, decreases from approximately 270 K in the western part to around 260 K over the contiguous floes in the eastern part. It is important to note that the maximum surface temperature of the entire scene is 270.6 K, i. e., below the freezing point of 271.35 K which we assume for the MODIS sea-ice concentration retrieval. This means that the ice likely already started to grow also over the dark region in the western part of Fig. 6.1a).

The three sea-ice concentration datasets differ in their representation of the scene, mainly in the western part (see Fig. 6.2).

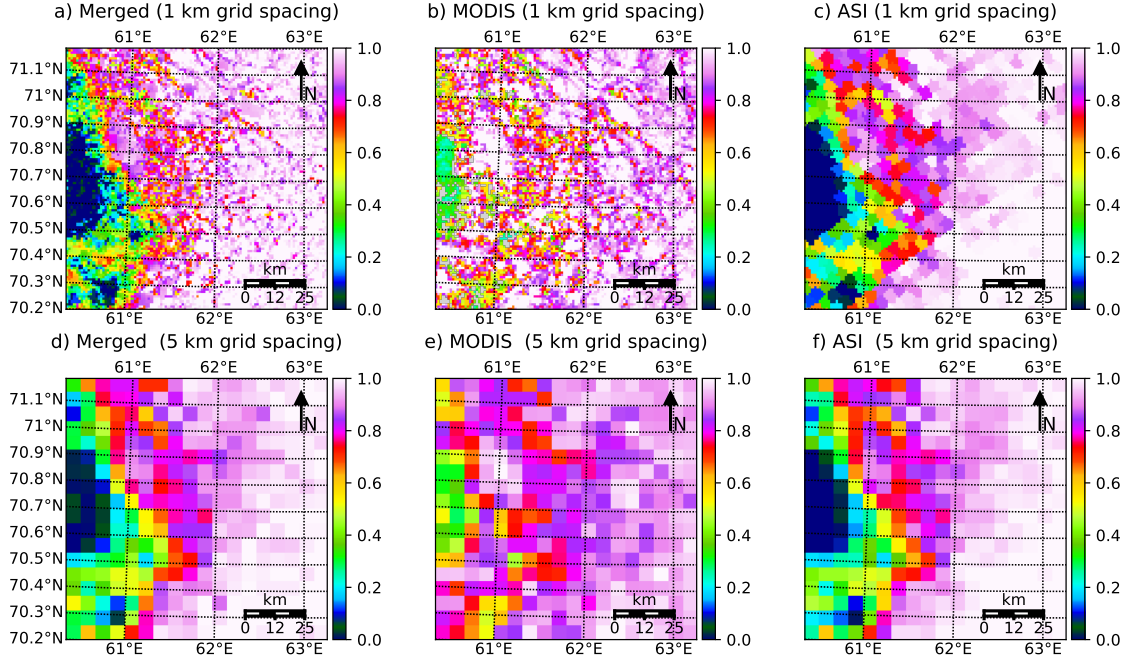


Figure 6.2.: Same scene as in Fig. 6.1, but showing the merged, MODIS and ASI sea-ice concentration. a) shows sea-ice concentration retrieved from MODIS measurements at a grid spacing of 1 km. b) shows sea-ice concentration retrieved by ASI and c) shows the merged sea-ice concentration dataset, both at 1 km grid spacing. d), e) and f) show the MODIS, ASI and merged sea-ice concentration, respectively, at 5 km grid spacing.

The merged and ASI sea-ice concentration go down to 0% over the dark region in Fig. 6.1a and are around 40% over the thin-ice region in the south-western corner. The MODIS sea-ice concentration is higher, around 40% over the region which appears dark in Fig. 6.1a and up to 100% in the south-western corner. In the eastern part of the scene, the merged and ASI sea-ice concentration is slightly higher than the MODIS sea-ice concentration. Apart from the magnitude, the datasets differ in the actual spatial resolution, which is about 1 km for the MODIS sea-ice concentration and about 5 km for the ASI sea-ice concentration. For the merging, the ASI sea-ice concentration have been upsampled to a grid spacing of 1 km (see section 4.2). The irregular arrangement of the ASI pixels in Figure 6.2c may partly be an artifact arising from this upsampling of the ASI sea-ice concentration from their effective field of view of about 5 km by 5 km to 1 km. The up-sampling is done by nearest-neighbour regriding. Depending on the exact coordinates, it may be that the nearest neighbours of two adjacent 1 km-pixels are from different 5 km-by-5 km footprints, considering the effective field of view. The resulting field at a resolution of 1 km is thus not necessarily composed of 5 km-by-5 km squares with identical sea-ice

concentration values, but may have adjacent pixels of identical sea-ice concentration which are not arranged in squares, but in irregular geometric shapes like those which are visible in 6.2c. Re-averaging them by calculating the mean of 5 by 5 adjacent pixels and then selecting the next 5 by 5 pixels yields the field shown in Fig. 6.2f.

Upsampling the ASI sea-ice concentration to a grid spacing of 1 km allows to incorporate the finer resolution of the MODIS sea-ice concentration, leading to the merged sea-ice concentration dataset shown in Fig. 6.2a. The merged sea-ice concentration resolves the floes in the eastern part of the image more finely than the ASI sea-ice concentration due to the inclusion of the MODIS sea-ice concentration, while tuning it to preserve the mean of the ASI sea-ice concentration causes it to be close to 0% in the western part of the scene. Next, we illustrate the difference between the MODIS and ASI sea-ice concentration and the effect of the merging in the scatter plots shown in Fig. 6.3. To this end, all datasets are downsampled to the 5 km resolution of the ASI sea-ice concentration.

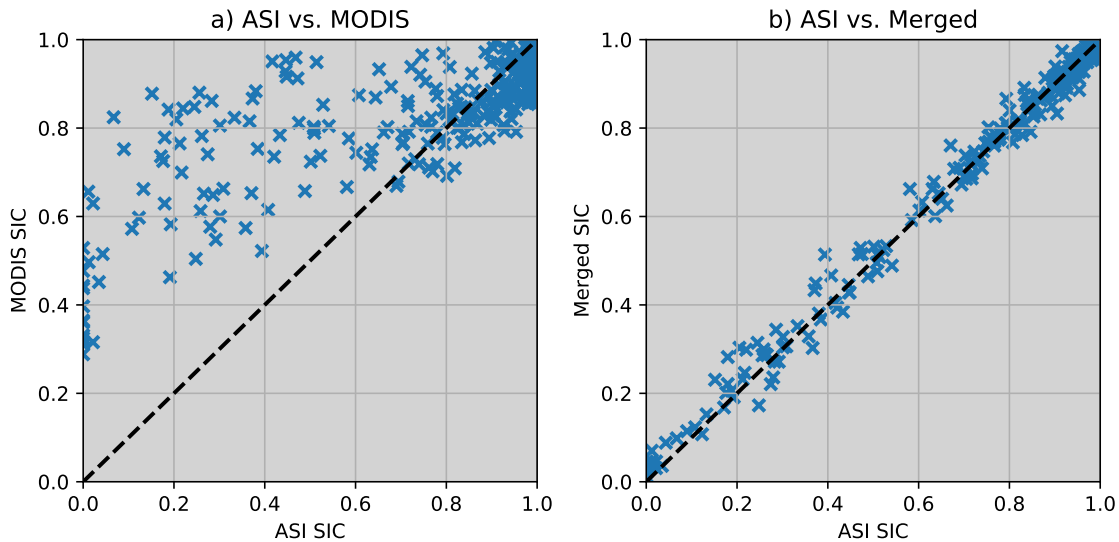


Figure 6.3.: Scatter plots of the sea-ice concentration datasets from Fig. 6.2d)–f). a) shows the ASI sea-ice concentration (see Fig. 6.2f) versus the MODIS sea-ice concentration (see Fig. 6.2e). b) shows the ASI sea-ice concentration versus the merged sea-ice concentration (see Fig. 6.2d).

In the ASI sea-ice concentration range up to 70%, the MODIS sea-ice concentration is higher than the ASI sea-ice concentration. The difference is largest for small ASI sea-ice concentration values, which correspond to the region of the freshly forming ice shown in Fig. 6.1a). This illustrates the different sensitivities of the ASI and MODIS algorithms towards freshly growing ice. For ASI, Heygster et al. (2014) and Shokr and Kaleschke (2012) report sea-ice concentration underestimations between 20% and 40% for ice thinner than 10 cm, i. e., in the very early growth phase. This may explain why ASI shows 0% sea-ice concentration although the air temperature is below the freezing

point. The MODIS algorithm, on the other hand, retrieves sea-ice concentration as soon as the surface temperature is below the freezing point. Since high surface temperatures are associated with high ice tie-points (see, e. g., section 5.3), temperatures which are slightly below the freezing point can already cause comparably high sea-ice concentrations. The difference between MODIS and ASI decreases for higher ASI sea-ice concentration values. For ASI sea-ice concentration above 80 % (corresponding to the eastern part of Fig. 6.2f), the ASI sea-ice concentration is mostly higher than the MODIS sea-ice concentration. The majority of the MODIS sea-ice concentration ranges between 85 % and 100 % for ASI sea-ice concentration values of 100 %, while there are less cases in which the ASI sea-ice concentration is lower than the MODIS sea-ice concentration. This can be explained by the different designs of the algorithms. The MODIS sea-ice concentration algorithm was defined to represent the thermal forcing of the atmosphere at the surface/atmosphere interface. It is based on the temperature anomaly within the surrounding 48 km by 48 km. If two thickness classes are present in this region, one for which thermodynamic equilibrium is reached, i. e., the heat loss to the atmosphere at the surface equals the heat gain by the ocean at the bottom (see subsection 2.2.1 for details), and one thickness class for which thermal equilibrium is not yet reached, i. e., the heat loss at the surface exceeds the heat gain at the bottom, the ice-surface temperature of the latter class will be higher than that of the former and will thus be retrieved as reduced sea-ice concentration by the MODIS sea-ice concentration algorithm, even if the actual sea-ice concentration is 100 %. This is partly mitigated by deriving a pixel-wise ice tie-point field instead of one fixed ice tie-point in each 48 km-by-48 km box. The ASI algorithm, on the other hand, was designed to retrieve the actual ice fraction within one footprint and is insensitive to the ice thickness for ice thicker than approximately 10 cm (Shokr and Kaleschke, 2012; Heygster et al., 2014). It is thus expected to retrieve close to 100 % sea-ice concentration if the ice cover is closed.

The merged sea-ice concentration preserve the mean of the ASI sea-ice concentration over a region of 5 km by 5 km. One would thus expect that the crosses in Fig. 6.3b) are all located on the identity line. We attribute the spread to one step in the merging procedure: After tuning the MODIS sea-ice concentration in a region of 5 km by 5 km to match the mean ASI sea-ice concentration and filling the cloud gaps with the ASI sea-ice concentration, we slide the 5 km-by-5 km box by one pixel and repeat the procedure (see subsection 4.2), thus covering every pixel 25 times and selecting the mean as final merged sea-ice concentration. This means that each pixel is influenced by the 9 by 9 pixels in its surrounding. Pixels which are close to the pixel have a larger influence than pixels which are further away since they are within the 5 km-by-5 km box used for the merging more often. At intermediate sea-ice concentration values, more fluctuations are expected, which would explain why the spread around the identity line is comparably large for sea-ice concentration values between 20 % and 40 %. At 0 % and 100 %, a second effect contributes to the spread: If the mean ASI sea-ice concentration within a 5 km-by-5 km box is 0 % or 100 %, values of

less than 0 % or more than 100 % are allowed at single pixels in order to include the fine-resolution information of the MODIS sea-ice concentration. They are set to 0 % and 100 % in the end. In this case, the merged sea-ice concentration mean at a scale of 5 km will be higher (if the ASI sea-ice concentration is 0 %) or lower (if the ASI sea-ice concentration is 100 %). This explains why the merged sea-ice concentration in the western part of the scene depicted in Fig. 6.2d is higher than the ASI sea-ice concentration (see Fig. 6.2f), which corresponds to the spread of the merged sea-ice concentration where the ASI sea-ice concentration is 0 in Fig. 6.3b. Having illustrated the differences between the merged, MODIS and ASI sea-ice concentration, we now turn to evaluate their performance against a reference dataset.

6.1.2. Reference data

79 Sentinel-2 scenes are used for constructing the Sentinel-2 sea-ice concentration reference dataset (see Fig. 3.1). Figure 6.4 shows one example scene from the Kara Sea on March 12, 2019. The RGB image (see Fig. 6.4 a) shows that there are regions of open water (dark), regions which have been recently overfrozen (greyish) and regions with thicker ice (bright). Treating the thin-ice class as water results in a number of open-water areas within the ice pack in the Sentinel-2 SIC (see Fig. 6.4 d). These areas are shown as 100 % sea-ice concentration if the thin ice is treated as ice. A large open-water lead and an area of smaller ice floes in the north-western corner of the scene are still represented as reduced sea-ice concentration. The mean of the Sentinel-2 sea-ice concentration is reduced from 99.6 % to 88.1 % if the thin ice is included and excluded, respectively, and the standard deviation increases from 3.3 % to 23.6 %, respectively.

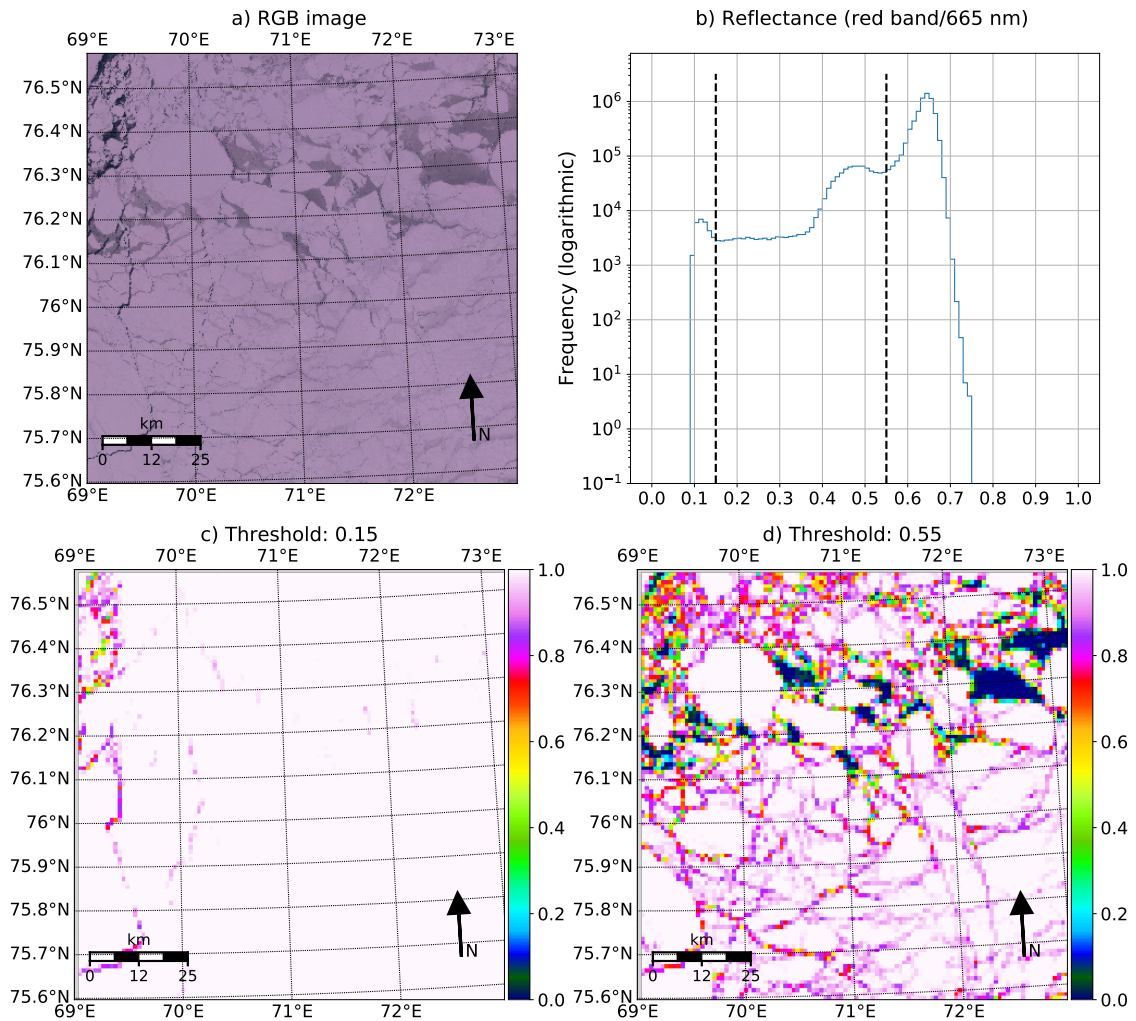


Figure 6.4.: Sentinel-2 sea-ice concentration in the Kara Sea on March 12 2019. a) Image using the Sentinel-2 channels 4 (red/665 nm), 3 (green/560 nm) and 2 (blue/490 nm). It shows open water (dark areas in the north-western corner), thin ice (for example, darker patches in the north-eastern corner) and thick ice (southern half of the scene). b) Frequency of occurrence of the 665 nm reflectance. Mind the logarithmic scaling of the y-axis. Vertical dashed lines mark the threshold for the thin and thick ice class. c): Sentinel-2 sea-ice concentration if thin ice is treated as ice. d) Sentinel-2 sea-ice concentration if thin ice is treated as water.

Next, we present the time series of all Sentinel-2 scenes in Fig. 6.5. The mean thin-ice sea-ice concentration was 94.4 %, while the mean of the thick-ice sea-ice concentration was 87.3 %. The mean sea-ice concentration standard deviations within a scene were 9.2 % (thin-ice SIC) and 13.2 % (thick-ice SIC). In scenes with 100 % sea-ice concentration, the thin- and thick-ice SIC is equal, i. e., there is no thin ice. In all other cases, the thin-ice SIC is higher, i. e., there is thin ice.

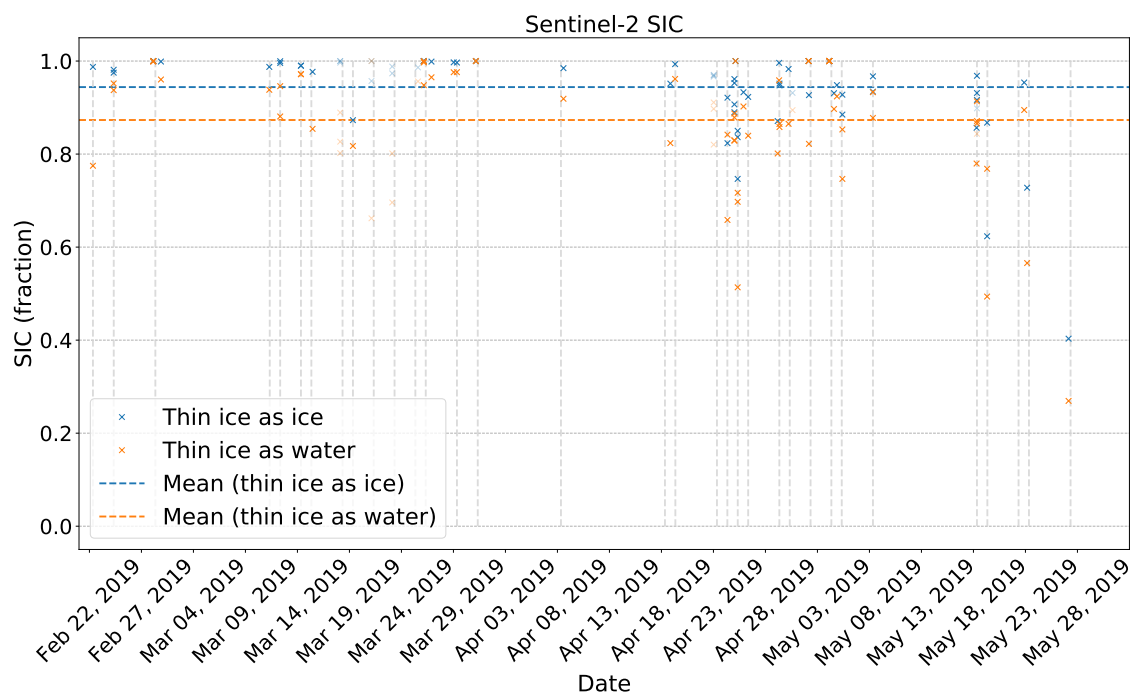


Figure 6.5.: Time series of the mean thin-ice and thick-ice SIC of all Sentinel-2 scenes. The x-axis shows the date, the vertical lines mark the days with Sentinel-2 scenes. Scenes with more than two hours time-lag towards the next MODIS/AMSR2 overflight are not used for the intercomparison, but included in the thesis because of their possible relevance for other validation studies.

To add another independent source, we also evaluated our data using five Landsat 8 scenes acquired in the Laptev Sea in March and April 2015 and 2016 (see Fig. 3.3). The analysis is limited to thin-ice SIC, i. e., thin ice was always treated as ice. The results are shown in subsections 6.2.2 and 6.3.2.

6.1.3. Time series of MODIS and merged sea-ice concentration

The MODIS and merged sea-ice concentration time series corresponding to the 66 Sentinel-2 scenes with a time lag below two hours are shown in Fig. 6.6. The ASI sea-ice concentration time series is not shown as the ASI sea-ice concentration mean is identical to that of the merged sea-ice concentration by definition. There is no significant bias between the datasets, the mean merged and MODIS sea-ice concentration are 93.1% and 92.8%, respectively. The Sentinel-2 thin- and thick ice SIC means are 94.4% and 87.3%, respectively. The RMSD between the MODIS and merged sea-ice concentration is 5.0%, which shows that the two datasets do differ. In the case with the largest discrepancy, the merged sea-ice concentration is 94.4%, while the MODIS sea-ice concentration is only 83.3%. Only points where MODIS data are available are considered in the means, so that different coverage cannot be the reason for these large differences. We will later in-

investigate this scene in detail to understand the reasons for the deviation. Generally, the absolute differences to the thin-ice Sentinel-2 SIC are smaller (mostly within $\pm 10\%$) than to the thick-ice SIC, which range from 10% to -30% . A positive difference means that the Sentinel-2 sea-ice concentration are higher. Next, we show selected scenes to demonstrate the benefit of the merged sea-ice concentration over the single-sensor sea-ice concentration data.

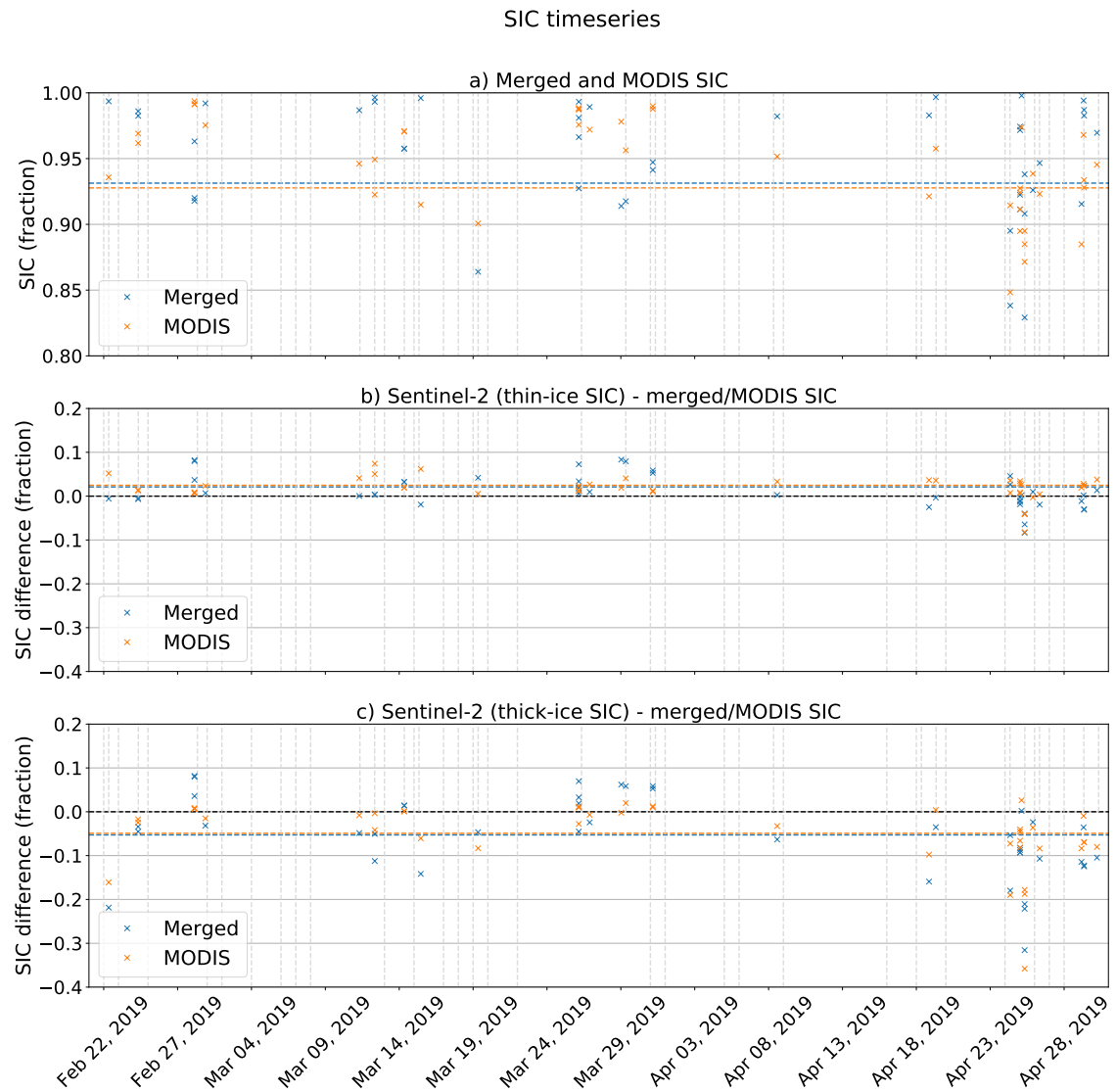


Figure 6.6.: a) Timeseries of the merged and MODIS sea-ice concentration corresponding to the Sentinel-2 time series from Fig. 6.5. The horizontal dashed lines show the mean of the respective dataset. b) Difference between the merged and MODIS sea-ice concentration and the thin-ice Sentinel-2 SIC from Fig. 6.5. Positive differences mean that the Sentinel-2 SIC is higher. The horizontal dashed lines show the mean difference for the respective dataset. c) Same as b), but for the thick-ice Sentinel-2 SIC. The x-axis shows the date, the vertical lines mark the days with Sentinel-2 scenes.

6.2. Benefits of merged dataset

6.2.1. Evaluation using Sentinel-2

An example to demonstrate the benefit of the merged dataset is presented in Fig. 6.7 which shows a scene recorded in the Beaufort Sea on May 22, 2020. The scene comprises one large open lead, several narrower leads and large, contiguous ice floes of 100 % sea-ice concentration (see Fig. 6.7 a). Some of the narrower leads are completely overfrozen, some are completely open and some are partly overfrozen. It is hard to determine one scene-wide threshold which classifies all pixels with open water as open and all overfrozen leads, even those with frazil or very thin ice as overfrozen. Some misclassification is likely to occur, so that the thin-ice SIC probably also includes small amounts of pixels which have been classified as ice, but are actually open water. Our approach of choosing one thin-ice threshold per scene, not one global thin-ice threshold for all scenes, reduces the risk of this misclassification. The MODIS sea-ice concentration resolve the leads as reduced sea-ice concentration, but undershoot the reference sea-ice concentration of the larger ice floes.

The ASI data consistently show 100 % sea-ice concentration over the large floes (see Fig. 6.7 j). The overfrozen, yet still recognisable leads are not visible in the ASI sea-ice concentration, except for a coarsely resolved large open lead in the middle of the scene. This is not a failure of the algorithm. Rather, the coarse resolution is because of the frequency and the insensitivity towards overfrozen leads is because the polarisation difference which the algorithm uses to derive sea-ice concentration approaches the ASI ice tie-point rapidly once the freezing started (Shokr and Kaleschke, 2012). Also, the non-linear nature of the ASI algorithm reduces variability near 100 %. This can lead to an overestimation of sea-ice concentration between 90 % and 100 % and may explain why we do not see traces of narrow leads in the ASI sea-ice concentration data.

The merged SIC resolves both the narrow, overfrozen leads and the large, open lead as reduced sea-ice concentration (see Fig. 6.7 d). At the same time, tuning them to preserve the ASI mean causes them to show close to 100 % sea-ice concentration over the large ice floes where the MODIS sea-ice concentration are around 90 %. A small open-water area in the south-eastern corner of the scene is partly masked in the MODIS sea-ice concentration, but retrieved by the ASI and the merged sea-ice concentration.

The mean of the merged sea-ice concentration is 98.7 %, while the mean of the thin- and thick-ice Sentinel-2 SIC is 95.9 % and 90.2 %, respectively. The MODIS sea-ice concentration is 88.7 %, which means an underestimation compared to both the thin- and the thick-ice Sentinel-2 SIC. The ASI sea-ice concentration have the smallest RMSD (12.0 %) compared to the thin-ice SIC, the RMSDs of the merged sea-ice concentration (13.5 %) and the MODIS sea-ice concentration (15.6 %) are higher. All RMSDs increase when considering thin ice as water (thick-ice SIC). The MODIS RMSD is now 16.3 %, while the merged and ASI RMSDs are 19.9 % and 19.8 %, respectively. The open-water extent of

the merged sea-ice concentration, 771 km^2 , is close to that of the thin-ice Sentinel-2 SIC (878 km^2). The open-water extent of ASI is much smaller (182 km^2), while that of MODIS is much higher (2760 km^2). This value is close to the thick-ice Sentinel-2 open-water extent (2313 km^2). The area where measurements of all 3 sensors are available was 11350 km^2 . Thus in this case we conclude that the merged sea-ice concentration shows clear advantages over the ASI sea-ice concentration because of its finer resolution and ability to resolve almost all leads identified in the Sentinel-2 reference sea-ice concentration. Also compared to the MODIS sea-ice concentration the merged sea-ice concentration shows clear advantages because the bias and RMSD compared to the reference sea-ice concentration are lower and unnatural fluctuations in the MODIS sea-ice concentration are removed.

Table 6.1.: Like Table 6.3, but for the data from Fig. 6.7. All datasets are available for 11350 out of 11881 pixels, which yields a surface area of 11350 km^2 .

	Merged	MODIS	AMSR2	S2 (thin)	S2 (thick)
μ	98.7	88.7	98.8	95.9	90.2
Δ_{thin}	-2.8	7.2	-2.8	N/A	N/A
Δ_{thick}	-8.5	1.5	-8.5	N/A	N/A
$RMSD_{thin}$	13.5	15.6	12.0	N/A	N/A
$RMSD_{thick}$	19.9	16.3	19.8	N/A	N/A
$OWE [km^2]$	771	2760	182	878	2313

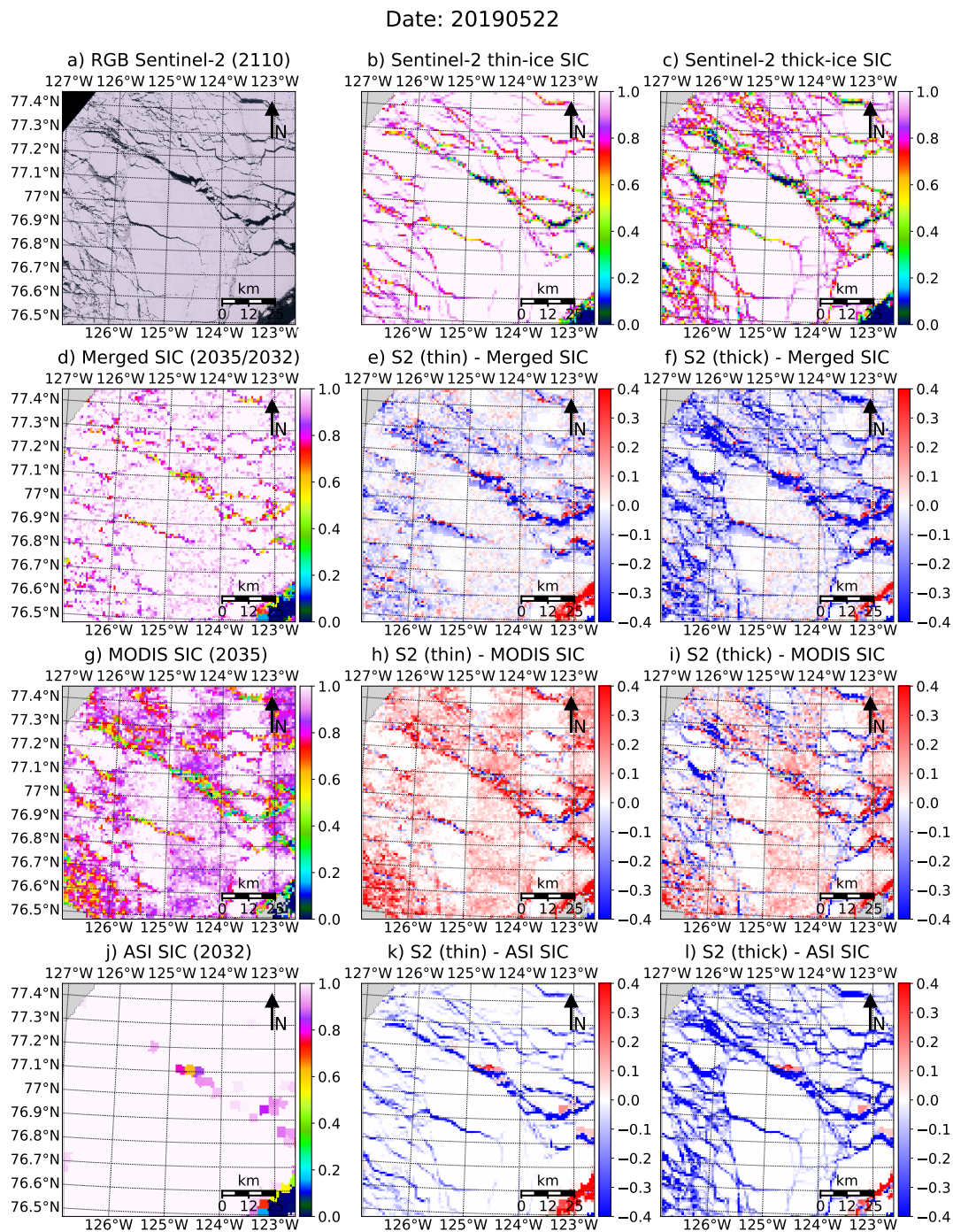


Figure 6.7.: Sentinel-2 scene in the Beaufort Sea on May 22, 2019 and the corresponding sea-ice concentration maps. a) Sentinel-2 RGB image. b)/c) Sentinel-2 sea-ice concentration with thin ice considered as ice (b) and water (c). d) through f) show the merged sea-ice concentration and their difference to the thin- and thick ice Sentinel-2 SIC. g) through i) and j) to l) show the same for the MODIS and ASI sea-ice concentration, respectively. The acquisition times for the single scenes in UTC are given in brackets in the titles of the maps in the left row.

6.2.2. Evaluation using Landsat 8

To have a second example for the benefits of the merged sea-ice concentration using another dataset as reference, we compare it to a Landsat 8 scene in this subsection. The Landsat 8 reflectance map in Fig. 6.8 c shows elongated features of reduced reflectance which are perpendicular to the leads close to 77°N , 111°E . These are likely not surface features, but clouds or cloud shadows from the masked clouds southeast of this region. The threshold which was chosen for the Landsat 8 sea-ice concentration classifies them as ice, so that they do not show up in the Landsat 8 sea-ice concentration. They are not screened by the MODIS cloud mask, but do not show up as anomaly in the MODIS sea-ice concentration. The Landsat 8 and MODIS acquisition times are close to identical (one MODIS granule covers five minutes), so that a cloud in the Landsat 8 scene would likely still be there when the MODIS granule was acquired. The fact that it does not show up in the MODIS sea-ice concentration indicates that the reduced reflectance is not due to a cloud, but the shadow of a cloud. Furthermore, we would expect a cloud to be brighter than the surface, i. e., increase the reflectance instead of decreasing it. The shadow would only result in a small ice-surface temperature anomaly, if at all, and thus likely not show up in the MODIS sea-ice concentration. A cloud, however, would probably change the ice-surface temperature more substantially.

A large lead, followed by an overfrozen region of thin ice, separates the landfast ice from the pack ice. The pack ice itself comprises leads and contiguous ice floes (see Fig. 6.8 a). The discrepancies between the sea-ice concentration datasets are largest over the thin-ice zone next to the large lead. The MODIS sea-ice concentration show around 80 %, while the other datasets are close to 100 % sea-ice concentration. Again, the discrepancy can be explained by the design of the MODIS sea-ice concentration algorithm. The region of 48 km by 48 km which is used for the MODIS ice tie-point calculation is larger than the area of thin ice and thus includes more than one ice class. The thin ice is therefore retrieved as reduced sea-ice concentration. Due to the merging, however, the merged sea-ice concentration is close to 100 % as it is tuned to preserve the mean of the ASI sea-ice concentration. While the thin-ice zone serves to demonstrate the benefit of tuning the merged sea-ice concentration to match the mean of the ASI sea-ice concentration, the benefit of including the MODIS sea-ice concentration is best demonstrated in the pack ice region, where the small leads visible in Fig. 6.8 a-c are not shown by the ASI sea-ice concentration (see Fig. 6.8 f), except for one region with leads in the eastern part of the scene at 77°N . As for the comparison with the Sentinel-2 reference sea-ice concentration in subsection 6.2.1, we attribute this to the reduced sensitivity of the ASI sea-ice concentration towards thin ice (Heygster et al., 2014; Shokr and Kaleschke, 2012) and to the nonlinearity of the ASI sea-ice concentration. Looking into the statistical properties of the sea-ice concentration datasets (see table 6.2), we find that the means of the merged sea-ice concentration and the MODIS are 1.6 % and 2.4 % higher than the Landsat 8 reference sea-ice concentration. The RMSDs of

the merged sea-ice concentration and ASI sea-ice concentration towards the Landsat 8 reference sea-ice concentration are almost identical (7.6% and 7.7% for the merged and ASI SIC, respectively), while that of the MODIS SIC towards the Landsat 8 SIC is higher (8.2%). The RMSD of the merged SIC has been calculated before setting the merged SIC above 1 to 1. If the merged SIC would be capped to 1 before the RMSD calculation (as is done in the final product), the RMSD would be reduced to 7.0%. As we found in the comparison with the Sentinel-2 reference SIC (see subsection 6.2.1), the benefit of the merged SIC over the ASI SIC mostly manifests in the higher open water extent. Here, the open-water extent of the merged SIC (528 km²) is one order of magnitude higher than the open-water extent of the ASI SIC (55 km²), although it is still lower than that of the Landsat 8 reference SIC (1213 km²).

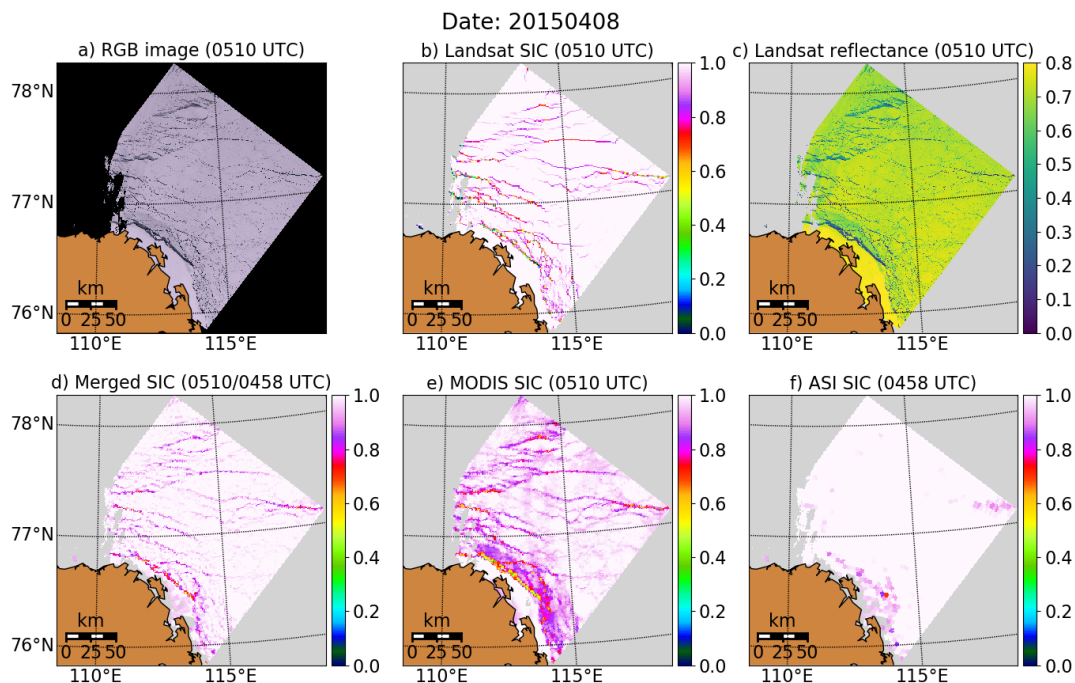


Figure 6.8.: Landsat 8 scene in the Laptev Sea on April 8, 2015 and the corresponding SIC maps. a) Landsat 8 RGB image. b) Landsat 8 SIC. c) Landsat 8 reflectance. d) Merged SIC. e) MODIS SIC. f) ASI SIC. The acquisition times for the single scenes in UTC are given in brackets in the titles of the maps.

Table 6.2.: Mean μ , mean difference Δ , RMSD and open-water extent OWE for the data from Fig. 6.8. All datasets were available for 31035 out of 36588 pixels covered by Landsat 8, which yields a surface area of 31035 km².

	Merged	MODIS	AMSR2	Landsat-8
μ	99.7	96.4	99.7	98.2
Δ	-1.6	2.4	-1.7	N/A
<i>RMSD</i>	7.6	8.2	7.7	N/A
<i>OWE</i> [km ²]	528	2274	55	1213

6.2.3. Comparison at the ice margin

Apart from lead detection, the fine resolution of the merged sea-ice concentration allows a more accurate representation of the ice margin. The example in Fig. 6.9 shows a scene recorded in the drift zone east of Greenland on March 13, 2020. The false-color MODIS image (see Fig. 6.9 a) shows a number of comparably large floes (turquoise) along with areas of open water (dark) in the western part of the scene, a transition zone with streaks of ice in the central part of the scene and open water in the eastern part of the scene, where parts of the scene are obscured by clouds (bright).

The merged SIC (see Fig. 6.9 b) resolve most of the single floes in the western part of the image. An area of open water within the ice pack (south-western part in Fig. 6.9 a) is resolved as SIC of approximately 40 %. The ice streaks are shown as SIC of approximately 20 %.

In the MODIS SIC image (see Fig. 6.9 c), the ice floes in the western part of the image are mostly resolved as 100 % SIC. The same applies for most of the ice streaks. The ice streaks which are not resolved are masked out by the MODIS cloud mask, i. e., erroneously classified as cloud. The open-water area in the south-western part of the scene is also masked out although it is not cloudy. The cloudy parts in the eastern part of the scene are masked out. Since clouds close to the ice margin are challenging to detect (Ackerman et al., 2010), but nevertheless masked out reliably here in most cases, we judge the performance of the MODIS cloud mask as good in this example.

The ASI SIC show the most abrupt transition between the ice and the water part of the scene. The ice streaks which mark the ice margin are not shown. We attribute this to the effect of the weather filters, which often erroneously remove sea-ice concentration up to 30 % (Andersen et al., 2006; Ivanova et al., 2015).

Tuning the merged SIC to preserve the mean ASI SIC may cause an underestimation of the true SIC in parts of this scene. Note that, in absence of independent reference SIC for this scene, we do not know the true SIC and can only compare qualitatively. Some of the contiguous ice floes (e. g., west of 73 °N, 15 °W) are shown as reduced SIC by the ASI SIC

although they seem to be close to 100% SIC in the false-color image and are retrieved as 100% SIC by MODIS. We accept this as a trade-off because tuning the merged SIC to preserve the mean ASI SIC ensures spatial continuity if MODIS data are not available. The fact that the ice streaks are resolved in the merged SIC despite our requirement to keep the ASI SIC mean reflects that we tolerate SIC below 0% in an interim step to benefit from the fine resolution of the MODIS SIC (see section 4.2 for details). Due to this, we can keep low SIC like in this example and the merged SIC mean still is 0% until we cap the negative SIC in the end.

We conclude that the merged SIC dataset has benefits over both input datasets for monitoring the ice margin. The effect of the weather filters erroneously discarding low ASI SIC is mitigated by the merging, so that the streaks of ice are shown in the merged SIC. At the same time, the cloud gaps in the MODIS SIC are filled by the merging.

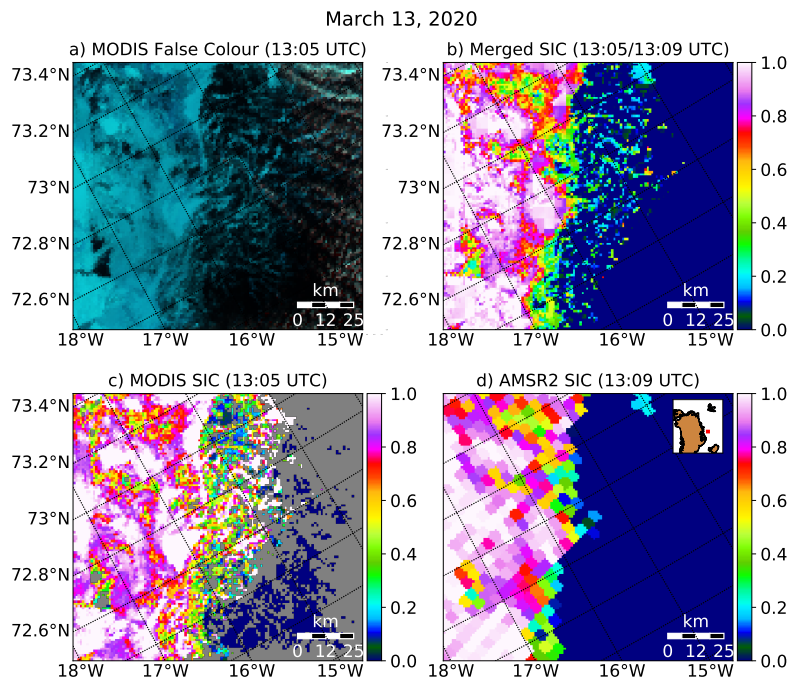


Figure 6.9.: Scene on March 13, 2020 which compares the ice margin as seen by the different datasets. a) False-color MODIS image utilizing bands 7 (2130 nm), 2 (858 nm), and 1 (645 nm) as red, green, and blue, respectively. Ice/snow, water and clouds appear turquoise, black, and white, respectively. b) Merged SIC. c) MODIS SIC. d) ASI SIC. The acquisition times of the single datasets are given in brackets in the captions. The inset in panel d) shows the region as small red square.

6.3. Limitations of merged dataset

Having demonstrated the benefits of the merged dataset, we will now show cases where either the MODIS sea-ice concentration or the ASI sea-ice concentration were of poor quality (subsections 6.3.1 and 6.3.2, respectively). Furthermore, we elaborate on the performance of ASI over landfast ice in subsection 6.3.3.

6.3.1. Merging with poor-quality MODIS sea-ice concentration

In Fig. 6.10, we present SIC maps for the scene with the largest discrepancy between the merged and the MODIS SIC. It is located in the Kara Sea and was acquired on May 18, 2019. The RGB image shows a multitude of small ice floes. The gap in the southwestern corner is not caused by a cloud, but by high MODIS ice tie-points, as we show in Fig. 6.11 b and c. The edge of the gap exactly follows the 270 K contour, above which no MODIS SIC are retrieved currently (see section 4.1). A new threshold of 266.5 K for future work is derived in section 5.4. The poor quality of the MODIS SIC with stripes of high and intermediate SIC which do not resemble the reference SIC at all over the entire scene, shows that this threshold which we chose initially is too conservative in this case. This highlights the importance of the ice tie-point threshold for meaningful MODIS SIC retrieval which we derived in section 5.4.

The performance of the MODIS SIC retrieval is further deteriorated by an unscreened cloud in the eastern part of the scene (see Fig. 6.11 a). This is hard to see here, but was determined by zooming into the full-resolution image. This scene therefore shows both the susceptibility of the MODIS SIC retrieval towards high surface temperatures and the susceptibility towards unscreened clouds. This might be even more pronounced in winter when the visible channels are not available for cloud masking. However, the visible channel cloud screening also has problems differentiating clouds from the ice surface (Ackerman et al., 1998). Furthermore, we expect less clouds in winter as there is less evaporation under cold conditions and a larger ice coverage.

In the part without MODIS data, the actual resolution of the merged dataset goes down to 5 km. The almost vertical stripes in the ASI and merged SIC (see Fig. 6.10 d, j) are along the AMSR2 scan lines. They are caused by fluctuations in the radiometer gain at 89 GHz within one scan for which currently no correction procedure is available (personal communication, Georg Heygster). The part of the scene where MODIS data are available is resolved more finely. The finer-resolution patterns of the merged SIC resemble the reference SIC, however the single floes are too small and the time difference is too large to recognize distinct floes of the reference SIC scene in the merged SIC (see Fig. 6.10 d). The influence of the large difference between the MODIS SIC and the Sentinel-2 SIC on the merged SIC is mitigated as we tune the merged SIC to preserve the ASI mean. We conclude that in this scene including the poor-quality MODIS SIC does not significantly deteriorate the quality of the merged SIC, but we also cannot conclude that it enhances

the quality.

All datasets underestimate the thin-ice SIC, the merged and MODIS SIC by 3.8% and 16.7%, respectively and the ASI SIC by 3.8%. The difference compared to the thick-ice SIC is smaller for all datasets (-1.4%, 11.7% and -1.3% for the merged/MODIS/ASI SIC, respectively). The percentages are absolute values, i. e., not relative to the other percentage value. Small differences do not necessarily indicate a more precise result, but can be the consequence of positive and negative differences cancelling out for the merged and ASI SIC. This is underlined by the RMSD between the Sentinel-2 reference SIC, the merged SIC, and the ASI SIC. It is smaller when computed towards the thin-ice SIC (9.3% for the merged SIC and 6.9% for the ASI SIC) than when computed towards to the thick-ice SIC (11% for the merged SIC and 6.2% for the ASI SIC). For the MODIS SIC, the RMSD is lower for the thick-ice SIC. To demonstrate the benefit of the finer resolution, we compare the open-water extent (area of pixels covered by at least 15% of water) of the datasets. We only consider pixels where all datasets are available, which yields an area of 8191 km². The open-water extent of the thin- and thick-ice Sentinel-2 SIC is 208 km² and 1045 km², respectively. The open-water extent of the merged SIC (818 km²) is close to the thick-ice open-water extent (1045 km²), but higher than the thin-ice open-water extent (208 km²). The ASI open-water extent (292 km²) is close to the thin-ice open-water extent, but lower than the thick-ice open-water extent. The MODIS open-water extent of 4508 km² is higher than both the thin- and the thick-ice open-water extent. An overview over all parameters is given in Table 6.3.

Table 6.3.: Comparison of the different SIC datasets in Fig. 6.10. We show the mean μ , the mean difference Δ between the thin- and thick-ice Sentinel-2 SIC and the respective dataset, the RMSD towards the thin- and thick-ice Sentinel-2 SIC and the open-water extent (OWE, area of pixels with less than 85% SIC). A positive difference means that the Sentinel-2 SIC is higher. All quantities except the open water extent are given as fraction of 1. Only pixels where all datasets are available are considered for the comparison. For this scene, this amounts to 8191 of 11881 pixels, equivalent to an area of 8191 km². Details about location and acquisition time of the scene are given in the caption of Fig. 6.10.

	Merged	MODIS	AMSR2	S2 (thin)	S2 (thick)
μ	94.4	81.3	94.3	98.1	93.0
Δ_{thin}	3.6	16.7	3.8	N/A	N/A
Δ_{thick}	-1.4	11.7	-1.3	N/A	N/A
$RMSD_{thin}$	9.3	23.5	6.9	N/A	N/A
$RMSD_{thick}$	11.0	21.2	9.2	N/A	N/A
$OWE [km^2]$	818	4508	292	208	1045

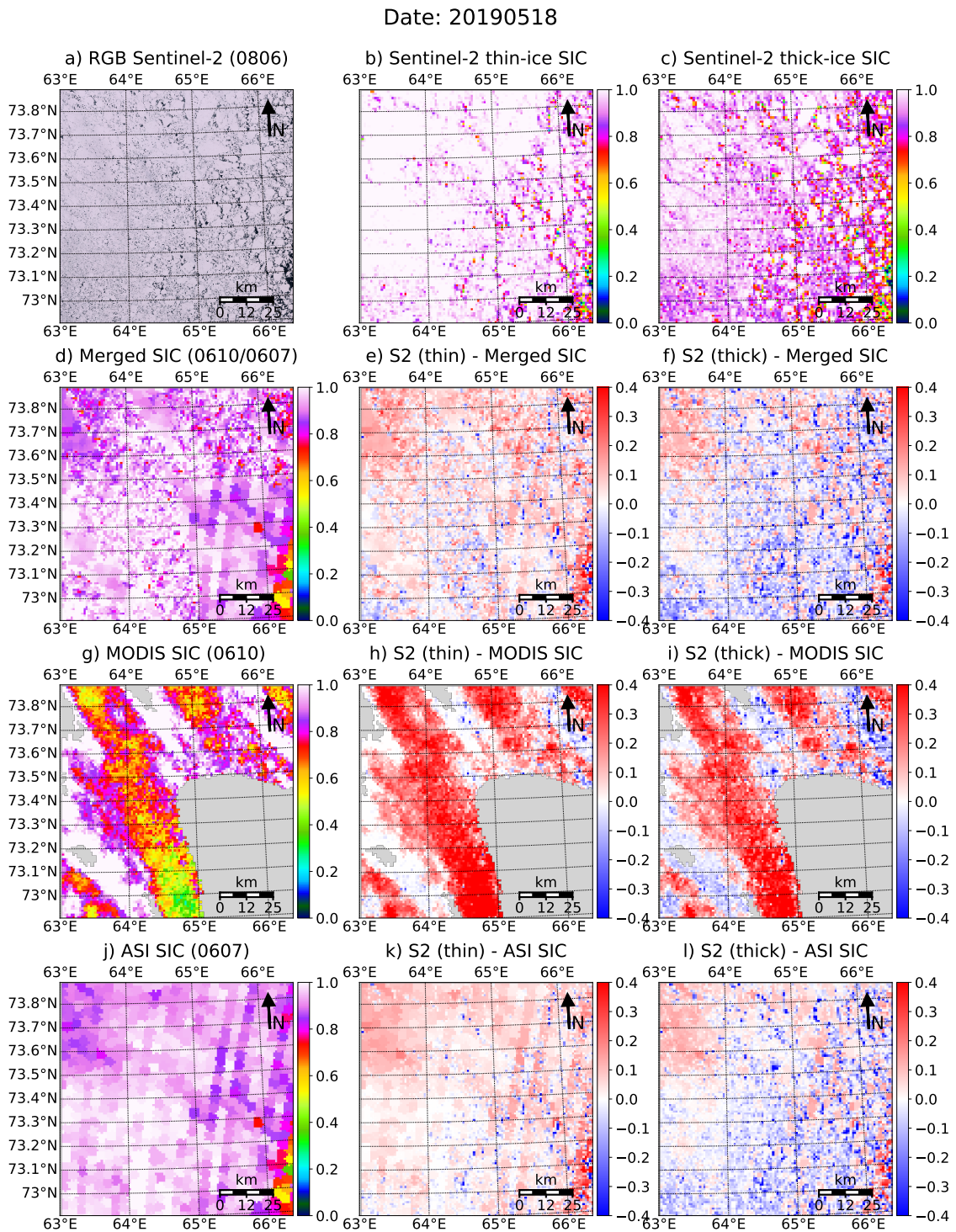


Figure 6.10.: Sentinel-2 scene in the Kara Sea on May 18, 2019 and the corresponding SIC maps. a) Sentinel-2 RGB image. b) Sentinel-2 SIC with thin ice considered as ice. c) Sentinel-2 SIC with thin ice considered as water. d) through f) show the merged SIC and their difference to the thin- and thick ice Sentinel-2 SIC. g) through i) and j) to l) show the same for the MODIS and ASI SIC, respectively. The acquisition times for the single scenes in UTC are given in brackets in the titles of the maps in the left row.

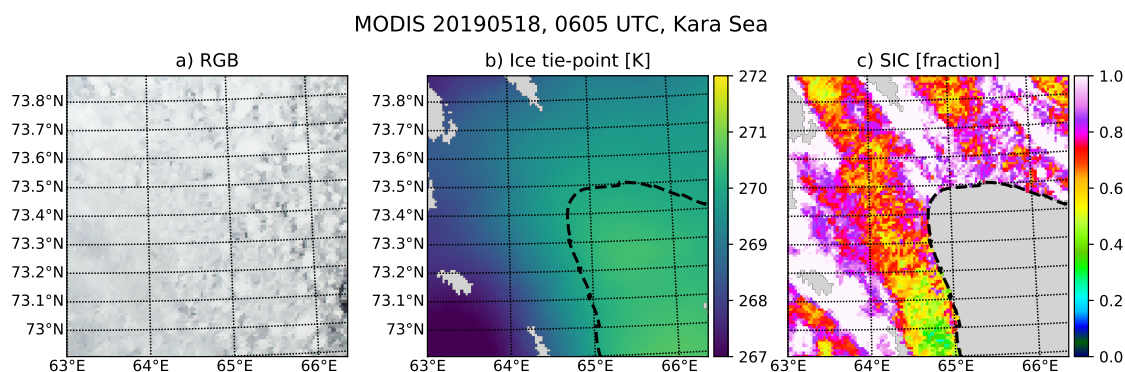


Figure 6.11.: a) MODIS RGB image of the scene in Fig. 6.10 g. b) Ice tie-point of the MODIS sea-ice concentration. The dashed line marks the 270 K threshold above which no SIC retrieval is performed. c) MODIS SIC as in Fig. 6.10 g.

6.3.2. Merging with poor-quality ASI SIC

Having shown an example of poor-quality MODIS sea-ice concentration, we now show an example of poor-quality ASI sea-ice concentration in Fig. 6.12. We identify two regions of reduced reflectance (around 120°E , 73°N and at 123°E , 73°N , see Fig. 6.12 c). They are of similar shape as the cloud gaps nearby (see Fig. 6.12 a), therefore we interpret them as cloud shadows. They do not appear in the MODIS SIC, which indicates that the thermal infrared channels which are used for the MODIS SIC retrieval are not very sensitive to cloud shadows.

The scene comprises a large region of landfast ice, a large lead and a smaller region of pack ice with leads (see Fig. 6.12). The ASI SIC over the landfast ice are between 80 % and 85 %, i. e., 15 % to 20 % too low (see Fig. 6.12 f). This underestimation has been investigated in an internal report, but the reason could not be identified (Wiedemeier and Ludwig (2017), see subsection 6.3.3). The MODIS SIC over the landfast ice are close to 100 %. Tuning the merged SIC to preserve the ASI SIC mean causes them to simultaneously underestimate the SIC over the landfast ice. In the small region outside of the landfast ice, the advantage still becomes manifest in the more finely resolved leads.

The mean Landsat 8 reference SIC is 99.1 % (see table 6.4). The mean merged and ASI SIC is 93.1 % and the mean MODIS SIC is 96.3 %. Consequently, the open-water extent of both the merged and ASI SIC is more than 4 times (merged SIC) respectively 5 times (ASI SIC) higher than that of the Landsat 8 reference SIC. The MODIS open-water extent is closest to that of the Landsat 8 reference SIC, but still 2.5 times higher. Also the RMSD (10.1 % for the MODIS SIC, 12.8 % for the merged and ASI SIC) shows that the MODIS SIC represent the Landsat 8 reference SIC better, so that the merged product is of poorer quality than the MODIS SIC. However, it is not worse than the ASI SIC and probably even better outside of the landfast ice zone due to the finer resolution, although that is hard to quantify here.

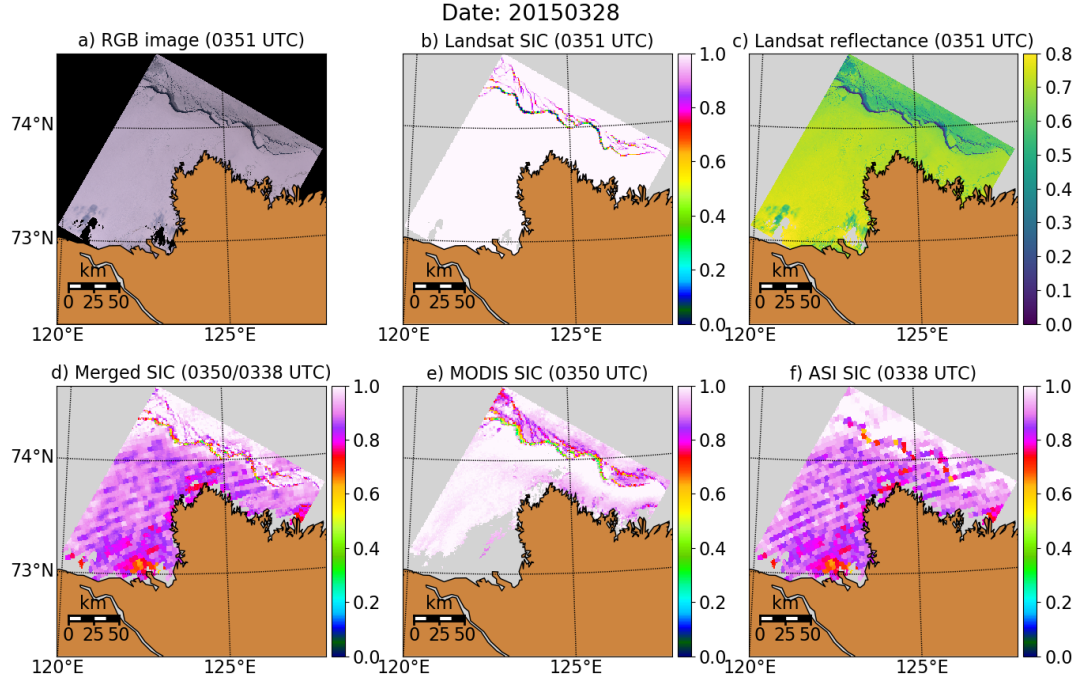


Figure 6.12.: Landsat 8 scene in the Laptev Sea on April 8, 2015 and the corresponding SIC maps. a) Merged SIC. b) MODIS SIC. c) ASI SIC. d) Landsat 8 SIC. e) Landsat 8 RGB image. The acquisition times for the single scenes in UTC are given in brackets in the titles of the maps.

Table 6.4.: Mean μ , mean difference Δ , RMSD and open-water extent OWE for the data from Fig. 6.12. All datasets were available for 17955 pixels out of 36588 pixels covered by Landsat 8, which yields a surface area of 17955 km².

	Merged	MODIS	AMSR2	Landsat-8
μ	93.1	96.3	93.1	99.1
Δ	8.8	2.6	8.8	N/A
<i>RMSD</i>	12.8	10.1	12.8	N/A
<i>OWE</i> [km ²]	2270	1206	2755	510

6.3.3. ASI sea-ice concentration over landfast ice

The negative bias of the ASI SIC over landfast ice (see subsection 6.3.2) is investigated by Wiedemeier and Ludwig (2017). They identified ten cases between January and April 2015 (see section 3.2.2) in which the 95th percentile difference (Landsat 8 reference SIC – ASI SIC) was between 4% and 33%. The 95th percentile difference was larger than 20% SIC in five of the ten cases.

The ASI SIC algorithm is based on the different polarisation differences of ice (small po-

larisation difference) and water (large polarisation difference), therefore Wiedemeier and Ludwig (2017) strive to identify a process which increases the polarisation difference. They investigate temperature, snow depth, atmosphere contributions, radiative fluxes and snow metamorphism using ERA Interim Reanalysis data (Dee et al., 2011). Surface roughness, snow density and salinity could not be investigated because no suitable data were available.

None of the investigated parameters or processes could be clearly identified as reason for the negative bias. The temperature hardly rose above 0°C , so that melt-refreeze cycles can be excluded as a reason. No relationship was found between ice-surface temperature and polarisation difference. For snow depth, one would expect a negative correlation as snow decreases the polarisation difference, therefore a decreasing snow depth should be associated with a large underestimation. However, the snow depth generally increased during the anomalies, so that it could be ruled out. For the analysis of atmospheric contributions, namely water vapour and ozone, radiative fluxes (surface latent heat flux, surface net thermal radiation and top net thermal radiation) and snow grain size, the reader is referred to Wiedemeier and Ludwig (2017).

Finally, we checked other SIC algorithms, namely ECICE, (Shokr et al. (2008); Ye et al. (2016a,b), calculated internally), the Bootstrap algorithm (Comiso (1995), calculated internally) and the NASA Team algorithm (Cavalieri et al., 1997) for the scene in Fig. 6.12. The resulting maps are shown in Fig. 6.13. All three algorithms underestimate SIC over the landfast ice. The NASA Team SIC are of similar magnitude as the ASI SIC, but distributed homogeneously over the entire region, so that the landfast ice and the pack-ice region have approximately the same SIC. The Bootstrap and ECICE SIC are higher than the ASI SIC, but still below 100 % SIC and show different signatures over the landfast and the pack-ice regions. Thus, we conclude that the unknown process which causes the SIC underestimation of landfast ice affects the 89 GHz frequency which ASI uses more strongly than the 19 GHz and 37 GHz channels used by NASA Team, ECICE and Bootstrap. However, all algorithms significantly underestimate the true sea-ice concentration. A similar problem is reported by Lam et al. (2018), who investigate a case in Antarctica in which the 19 GHz and 37 GHz weather filters applied in the ASI algorithm erroneously set sea-ice concentration to 0 % over landfast ice, where it should be 100 %. They propose a melt-refreeze cycle and the associated snow metamorphism as most likely reason. While both Lam et al. (2018) and Wiedemeier and Ludwig (2017) investigate ASI sea-ice concentration underestimation over landfast ice, the reason which Lam et al. (2018) propose does not explain the underestimation in our cases since Wiedemeier and Ludwig (2017) excluded melt-refreeze cycles as reason. Furthermore, in the case of Wiedemeier and Ludwig (2017) the sea-ice concentration is underestimated by up to 25 %, while it is set to 0 %, i. e., underestimated by 100 %, in the case of Lam et al. (2018).

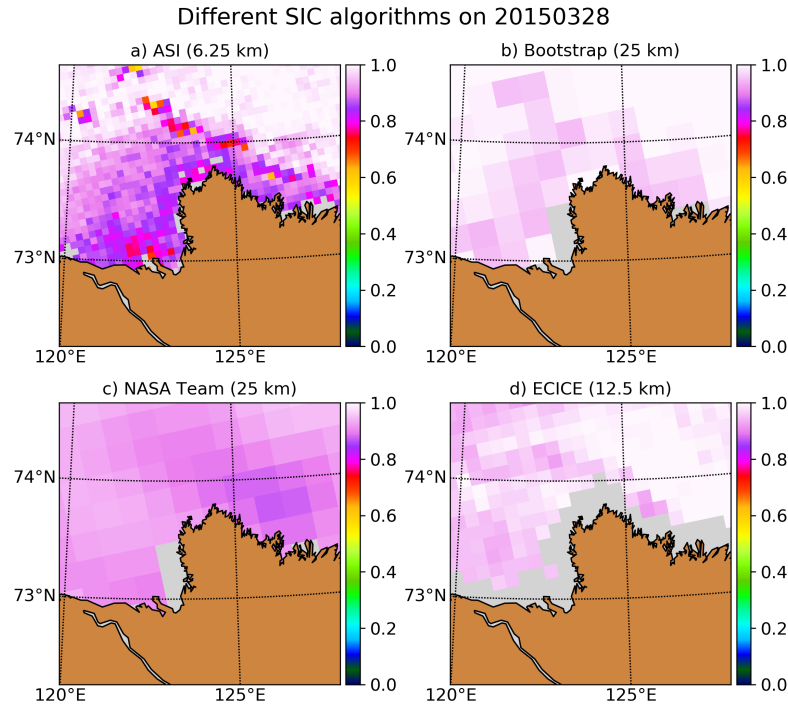


Figure 6.13.: Comparison of SIC algorithms for the scene from Fig. 6.12. The panels show the ASI SIC (panel a)), the Bootstrap-AMSR2 SIC (panel b)), the NASA Team-SSMIS SIC (panel c)) and the ECICE-ASCAT/AMSR2 SIC (panel d)). All arrays are daily means.

The fact that as many as ten examples were identified within four months in the Arctic despite the limited spatial and temporal availability of clear-sky Landsat 8 scenes shows that this effect should not be neglected for passive microwave radiometry over landfast ice. The Arctic-wide mean annual extent of landfast ice between 2008 and 2018 was $1.1 \cdot 10^6 \text{ km}^2$ (Li et al., 2020). Similar values for landfast ice area are not published to the author’s best knowledge, but we make the simplifying assumption that landfast ice extent and area are approximately the same. We argue that landfast ice mostly occurs in big, contiguous blocks which do not break easily. Thus, we assume that the landfast ice concentration in one grid cell is mostly 100 % or 0 %. Multiplying the grid cell area with the fraction of ice (landfast ice area) or counting all cells with more than 15 % landfast ice as completely ice-covered, regardless of their actual landfast ice concentration (landfast ice extent), should therefore yield comparable results. Assuming that the landfast ice is underestimated by 10 % on average, the annual mean total sea-ice area would be underestimated by $0.11 \cdot 10^6 \text{ km}^2$. Taking an annual mean sea-ice area of $9.18 \cdot 10^6 \text{ km}^2$ as reference (based on ASI SIC between 2013 and 2019, own calculations), the sea-ice area would be underestimated by 1.2 %. The underestimation is larger in winter than in summer, when the landfast ice disappears completely (Li et al., 2020). The presented numbers are a rough estimate based on single cases. More extensive research, e. g. comparing land-

fast ice charts directly to passive microwave SIC instead of only considering scenes where Landsat 8 images are available, is needed to obtain more robust results. Also, note that sea-ice extent, which is the most commonly used metric for overall sea-ice coverage in the Arctic, would not be affected as the ASI SIC is still above 15 %.

While the low bias of the ASI SIC over landfast ice is of relevance for landfast ice studies with passive microwave radiometry and causes estimates of the Arctic-wide sea-ice area to be too low, it is not the focus of this thesis. The main benefits of the merged SIC product, the spatial continuity and the enhanced potential for lead retrieval, are not affected by the low bias of the ASI SIC. Therefore, and because Wiedemeier and Ludwig (2017) could exclude most of the physical reasons which are known for influencing passive microwave measurements, the underestimation of landfast ice by the ASI SIC was not investigated further.

6.4. Uncertainty estimates

Having introduced and evaluated the merged, MODIS and ASI sea-ice concentration, we now present and evaluate uncertainty estimates for the three datasets.

6.4.1. Temporal evolution

In Fig. 6.14, we show the mean merged, ASI and MODIS SIC uncertainty estimates for the time between February 22nd and May 27th 2019. Only pixels where MODIS and ASI data are available are considered. The MODIS SIC uncertainty estimate increases with time as the main uncertainty contributor, the dynamic range, decreases. It is important to note that the dynamic range starts to decrease in April due to the increasing surface temperatures (see Fig. 5.6, an increase in ice tie-point means a decrease in dynamic range), while the MODIS SIC uncertainty estimate only increases in May. We explain this by the non-linear increase of the single MODIS SIC uncertainty components (see equations 4.6-4.7) for a linearly decreasing dynamic range. Therefore, a decrease of the dynamic range by for example 1 K has a stronger effect on the uncertainty estimate in May, already starting at a lower dynamic range than in April.

The increase of the MODIS SIC uncertainty estimate also causes the uncertainty estimate of the merged SIC to increase with time. In fact, the temporal evolution of the MODIS and merged SIC is nearly identical as the ASI SIC is quite constantly between 6 % and 8 % over the entire period. Therefore, the temporal variability of the MODIS SIC directly propagates into the merged SIC. The reason for the comparably constant uncertainty estimate of the ASI SIC is that we selected mainly Sentinel-2 scenes with high SIC and the ASI uncertainty is expressed as a function of SIC after Spreen et al. (2008). This is a much simpler assumption than the more realistic MODIS sea-ice concentration uncertainty

estimate and thus shows lower variability. It should not be interpreted as an assessment of the ASI uncertainty under different conditions.

The benefit of the merged dataset over the MODIS SIC with regard to uncertainty estimates is best demonstrated by the difference between their respective uncertainty estimates. Figure 6.14 b shows that the uncertainty estimate is reduced in most cases by including the ASI data. Until April, this mostly reflects in single scenes in which the MODIS SIC uncertainty estimate is between 10 % and 18 %, while the merged SIC uncertainty estimate is between 8 % and 14 %. Apart from these single scenes, the MODIS SIC uncertainty estimate is mostly between 5 % and 8 %, while the merged SIC uncertainty estimate is between 5 % and 6 %. In May, the uncertainty estimates of the merged and MODIS SIC start to increase. The increase of the merged SIC uncertainty estimate is less pronounced than that of the MODIS SIC uncertainty estimate. This means that the effect of including the ASI data reduces the uncertainty estimates stronger for higher uncertainty estimates. By the end of May, the mean uncertainty estimate of the merged SIC is 18 %, while the MODIS SIC uncertainty estimate is 25 %. When interpreting these numbers, the reader should keep in mind that there are large scene-to-scene fluctuations of up to 10 % (merged SIC uncertainty estimate) and up to 15 % (MODIS SIC uncertainty estimate). Considering the entire time series, the mean uncertainty estimate of the merged dataset is 8.9 %, while that of the MODIS SIC is 10.6 %. If only May is considered, the mean uncertainty estimates of the merged and the MODIS SIC are 11.6 % and 14.9 %.

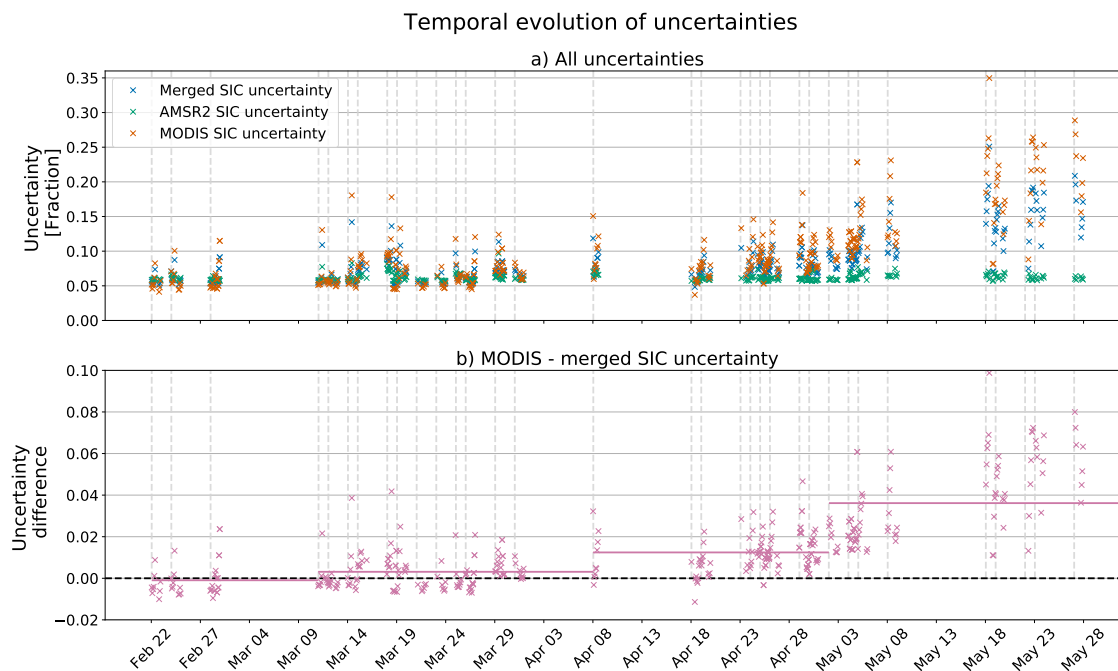


Figure 6.14.: The mean uncertainty estimate of the merged, ASI and MODIS sea-ice concentration is shown in panel a). Panel b) shows the difference between the MODIS SIC and the merged SIC uncertainty estimate, the monthly mean difference is shown as solid horizontal line. The uncertainty estimate is given as a fraction of 1. The x-axis shows the date, the vertical lines mark the days with Sentinel-2 scenes.

6.4.2. Evaluation

We evaluate the uncertainty estimates by comparing them to the differences towards the Sentinel-2 reference SIC from Fig. 6.6. Figure 6.15 shows that in most cases, our uncertainty estimate is larger than the actual difference to the reference Sentinel-2 SIC. The uncertainty estimates for the merged SIC are in most cases around 6%, go up to 15% and reach higher values only in exceptional cases. The differences are mostly close to 0% and hardly above 10%. In 79.2% of the cases, the uncertainty estimate is higher than the difference. The uncertainty estimates of the MODIS SIC are higher than those of the merged SIC. Uncertainty estimates to 20% occur frequently, but the majority is close to 5% and in 84.8% of the cases, the uncertainty estimate is higher than the difference. The ASI SIC uncertainty estimates are centered at about 5% and hardly exceed 8%. Here, our uncertainty estimates are higher than the differences in 72.8% of the cases. We conclude that our uncertainty estimates are a conservative assumption of the actual difference to the reference SIC. In the majority of cases (approximately 80%) the actual deviation from the real SIC should be lower than the uncertainty estimates provided in the merged SIC dataset.

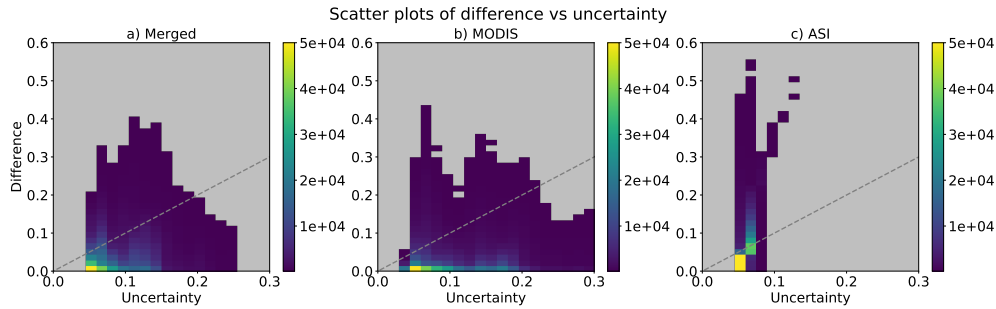


Figure 6.15.: a) Density scatter plot of the absolute difference to the thin-ice Sentinel-2 SIC against the merged (left), MODIS (middle) and ASI (right) SIC uncertainty estimate. All pixels, i. e., each pixel from each scene used for the time series in Fig. 6.6 are shown. We exclude pixels where one dataset is not available from all other datasets as well. This results in 743202 pixels. We use 40 bins per dimension and limit the data to the range between 0 and 0.6. All difference/uncertainty estimate pairs which occur less than 150 times are excluded. The color scale is cut at 50,000.

6.5. Discussion

MODIS SIC and ASI SIC are both influenced by sea-ice thickness. The ASI SIC underestimate a SIC of 100 % by up to 50 % for very thin ice (thinner than 6 cm), but are close to 100 % SIC for ice thicker than this under the surface conditions of our study (Shokr and Kaleschke, 2012). Heygster et al. (2014) confirm this by reporting SIC underestimations of 5 % or less for ice thicker than 10 cm. Other passive microwave SIC algorithms are affected more strongly by sea-ice thickness (Heygster et al., 2014; Shokr and Kaleschke, 2012).

The MODIS SIC underestimation due to sea-ice thickness is not linked to a certain thickness. Instead, it depends on the distribution of sea-ice thickness. The MODIS SIC algorithm assumes a bimodal ice thickness distribution within the region used for the ice tie-point retrieval. If more than one sea-ice thickness class is present in this region, the ice tie-point will represent the ice-surface temperature above the thicker ice, while the thin ice will appear warmer due to the oceanic heat flux and will thus be retrieved as reduced SIC. This is desired by Drüe and Heinemann (2004) who first applied the algorithm to retrieve SIC from MODIS data as their primary goal is to represent the thermal forcing of the atmosphere rather than the actual fraction of ice. In our case, this fraction is the quantity of interest. Thus, we tune the MODIS SIC to the mean of the ASI SIC which are closer to the actual ice surface fraction.

A situation with inhomogeneously distributed sea-ice thickness as described above can happen throughout the winter season, while sea ice which is thin enough to appear as reduced SIC in the ASI SIC is not expected that often, especially in winter then the large temperature contrast between ocean and air lets the ice grow quickly. We thus consider

the ASI SIC to be less dependent on sea-ice thickness than the MODIS SIC, which is again an argument for tuning the MODIS SIC to match the mean of the ASI SIC.

The main benefit of including the MODIS data is the higher potential for identifying leads. Generally, it is debatable whether an overfrozen lead should be shown as reduced SIC, since strictly speaking the SIC should be 100% instantly when the lead starts to refreeze. For most applications, e.g. heat flux calculation or navigation, the presence of leads is very relevant. A calculation in Kern et al. (2019) shows that for thick ice the heat flux would be approximately 9 W m^{-2} for 99% SIC and 5 W m^{-2} for 100% SIC. In a 1 km grid cell of our dataset, this would correspond to a difference of 4 MW. We see this and the importance of leads for navigation as a sufficient argument for keeping the leads as reduced SIC in our merged dataset. The benefit of keeping the leads is also reflected in the higher open-water extent of the merged and MODIS SIC compared to the ASI SIC. For lead retrieval only, the MODIS SIC would be more suitable than the merged SIC. However, our main goal is to have a dataset which does not only allow lead identification, but also offers spatial continuity. We therefore see our dataset as a compromise where a part of the lead information from the MODIS data is lost, but we judge the spatial continuity as valuable enough to accept this as a trade-off. For users who are mainly interested in leads, the MODIS SIC will be provided along with the merged SIC in a future version of our dataset.

Both MODIS and ASI SIC are strongly influenced by melt ponds. We do not consider this relevant for our study here since we do not cover the melt season, but it makes MODIS SIC retrieval from the ice-surface temperature in summer unfeasible, especially if we discard pixels with ice tie-points above 266.5 K as derived in section 5.4. The merged SIC are thus only available between October and May.

We do not compare our merged SIC to passive microwave SIC other than ASI. The reason for this is that the main advantage of our product over the well-established passive microwave SIC algorithms is the finer resolution. Since the ASI SIC have the finest spatial resolution of all passive microwave SIC algorithms, we expect the ASI SIC to yield an open-water extent (the metric which we used to show the advantages of the merged SIC) which is closer to that of the Sentinel-2 reference SIC than for the other passive microwave algorithms. Showing that the open-water extent of our merged SIC is closer to the Sentinel-2 open-water extent than that of the ASI SIC does thus immanently show that the merged SIC are also better compared to the other passive microwave SIC products with their even coarser spatial resolution. Since we preserve the mean of the ASI SIC, previous comparisons of ASI SIC to alternative SIC products (e.g. Ivanova et al. (2014, 2015); Kern et al. (2019, 2020)) are also valid for our product in terms of potential biases, although the variability might be different.

The selection of Sentinel-2 scenes for evaluation could introduce a bias into our dataset as we are a) limited to daylight conditions, b) limited to the marginal seas and c) limited to temporally unevenly sampled scenes. Our results are thus only representative for these

conditions and regions, they should not be interpreted as an assessment of the Arctic-wide SIC transition from late Winter to early Summer. However, the 66 reference scenes cover a fair amount of different ice conditions and a higher than average percentage of intermediate ice concentrations due to their location in the marginal seas. Low and intermediate SIC retrievals are in general more challenging and have higher uncertainties than the close to 100 % SIC in the central Arctic. Thus we do not expect worse results for the latter.

We make a quite simple approach for estimating the ASI SIC uncertainty by simply assuming them as a function of the SIC after Spreen et al. (2008), yielding uncertainties between 5 % and 10 %. The accuracy of the ASI SIC and 12 other passive microwave SIC algorithms has been assessed by Ivanova et al. (2015). They report accuracies between 3.1 % and 8.1 % compared to a reference dataset of 75 % SIC in winter (Table 2b in Ivanova et al. (2015)). The accuracy of ASI given by Ivanova et al. (2015) is 3.9 %. Our uncertainty estimates for the merged SIC during spring are mostly at the upper end of the range of the passive microwave SIC algorithms given by Ivanova et al. (2015), but higher in summer. However, the finer spatial resolution of our dataset has to be taken into account as an additional advantage. We thus judge our merged SIC uncertainty estimates as acceptable.

7. Case study: The 2018 North Greenland Polynya

This chapter is dedicated to a case study using our merged sea-ice concentration dataset published in Ludwig et al. (2019). We apply the merged sea-ice concentration dataset to monitor a polynya which formed north of Greenland in February 2018. A polynya is a non-linearly shaped opening in the sea ice (World Meteorological Organisation, 1970). Polynyas form the basis for food webs by enabling photosynthesis and provide food for mammals, birds and humans alike (Smith and Wessel, 1990; Morales-Maqueda et al., 2004; Schledermann, 1980). Preußer et al. (2016) report that polynyas between January and March have sizes between 400 and 43,600 km². Many polynyas recur annually in the same places (Morales-Maqueda et al., 2004; Preußer et al., 2016), but the one we investigate does not appear frequently (see Fig. 7.1). The sea ice north of Greenland is one of the oldest and thickest in the entire Arctic (Vaughan et al., 2013) and polynyas do not occur there regularly. Nevertheless, in February 2018, the sea ice was blown off-shore in the course of days, forming a coastal polynya which lasted from February 14th to March 8th and spanned more than 60,000 km² at its maximal extent.

In section 7.1, we put the polynya into the climatological context and describe the temporal evolution. Section 7.2 compares the different sea-ice concentration datasets, namely the merged, MODIS and ASI sea-ice concentration and sea-ice concentration derived from SAR data which we use for intercomparison in the absence of ground-truth reference data. Next, we analyse drift, temperature and air pressure to find out what caused the polynya in section 7.3. We conclude by estimating the amount of sea ice which grew in the polynya and the amount of heat released to the atmosphere in section 7.4 and discussing our findings in section 7.5.

7.1. Temporal evolution

7.1.1. Climatological context

Figure 7.1 puts the polynya into a climatological context by comparing it to the OSI SAF Climate Data Record (OSI-450) which goes back to 1979 (Lavergne et al., 2019). Since the Climate Data Record is only available until 2015, we use the OSI SAF Interim Climate

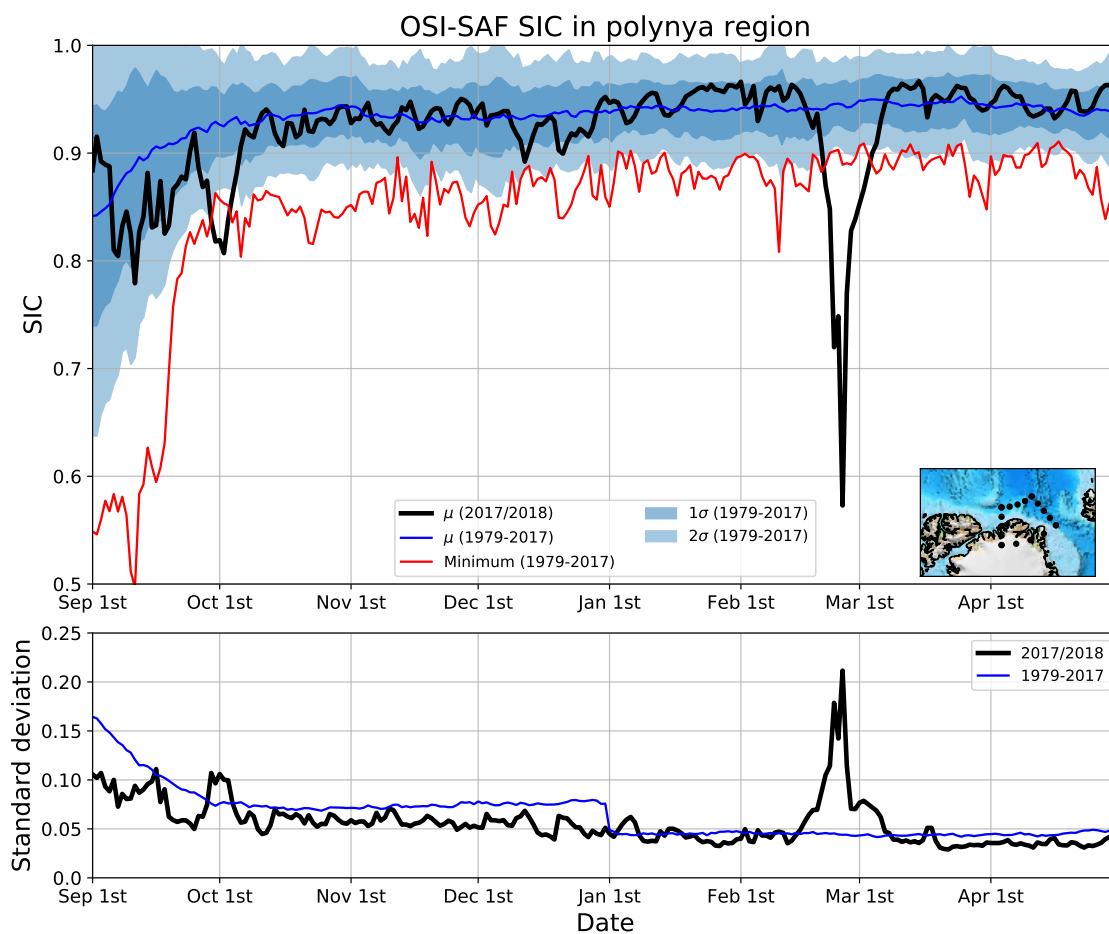


Figure 7.1.: Upper panel: Mean OSI-SAF SIC (Lavergne et al., 2019) in the polynya region (indicated by the dashed box on the map in the lower right corner). The black line shows the mean SIC in 2018. The blue line shows the mean SIC between 1979 and 2017. The dark/light shades indicate the $1\text{-}/2\sigma$ interval, respectively. The red line shows the minimal mean SIC between 1979 and 2017 for each day. Lower panel: Time series of the standard deviation in the polynya region for 2018 (black). The blue line shows the mean of the standard deviations in the polynya region between 1979 and 2017.

Data Record (OSI-430-b) after 2015. The products are temporally consistent at the transition. We show the 1979–2017 mean SIC in the polynya region (box on the inset map) for each day between September 1st and April 30th.

Normally, the mean SIC in the region north of Greenland is around 95 %, with a standard deviation of 3 % after the freeze-up period in September and October. The OSI SAF SIC are capped at 100 %, thus the SIC average can only be beneath 100 % and must result in lower SIC than might have been the case. The climatological mean and the standard deviation do not change much between the beginning of November and the end of April. Except for a 10 % drop during the early freeze-up at the end of September, the 2017/2018

SIC stayed within one standard deviation of the climatological mean until mid January. There was a two-week period of SIC above the climatological mean in the second half of January.

In mid February, the polynya started opening rapidly. The mean SIC was at its minimum at February 26th, when it was close to 70 %. Previously, the lowest mean SIC at any day between October 1st and April 30th was 79 %. The time series of the minimal SIC shows that there were other periods during which the mean SIC was outside of the 2σ interval in particular years, for example once in mid December 1986, once in early January 1984 and once in late March 1983 (single years not shown in Fig. 7.1). However, none of them reached the low extent of the 2017/2018 winter season.

We investigate the homogeneity of the sea-ice cover by calculating the mean spatial standard deviation in the polynya region (see Fig. 7.1, lower panel). It was above 20 % in 2018, while it is normally close to 5 %. This underlines how strongly the normally homogeneously distributed sea-ice cover north of Greenland broke up during this exceptional event.

7.1.2. Polynya development

Having shown that the polynya was unprecedented in magnitude in subsection 7.1.1, we now focus on describing the temporal and spatial development of the polynya during the opening and refreezing. For this, we show maps before, during and after the polynya event in Fig. 7.2 a–h, as well as a time series of the open water area from the merged product (see Fig. 7.2 i).

First leads are already visible on February 8th, six days before the polynya actually starts to open. Also, the shear zone parallel to the coast where the polynya will break up later is already visible. This demonstrates the benefit of the merged product over the ASI SIC, which would be too coarse to resolve these leads, as seen in Fig. 7.3.

Starting on February 14th, the polynya area increases steadily until February 22nd, when it already spans 30,000 km². The polynya area decreases on February 22nd and 24th. Apart from this, it increases strongly until it reaches its maximum extent on February 26th, when it spans more than 60,000 km² (see Fig. 7.2 i). Afterwards, the area decreases almost linearly with time until the now refrozen polynya is not identified as open water any more on March 8th. Note that the area of the opening is still visible as dark/new ice in the Sentinel-1 mosaic. There are areas (see Fig. 7.2 a, g) where leads and 100 % SIC are directly next to each other. This happens when there are no MODIS SIC available for the merging. In this case, the merged SIC are equal to the ASI SIC which show 100 % SIC for sea ice thicker than ≈ 10 cm.

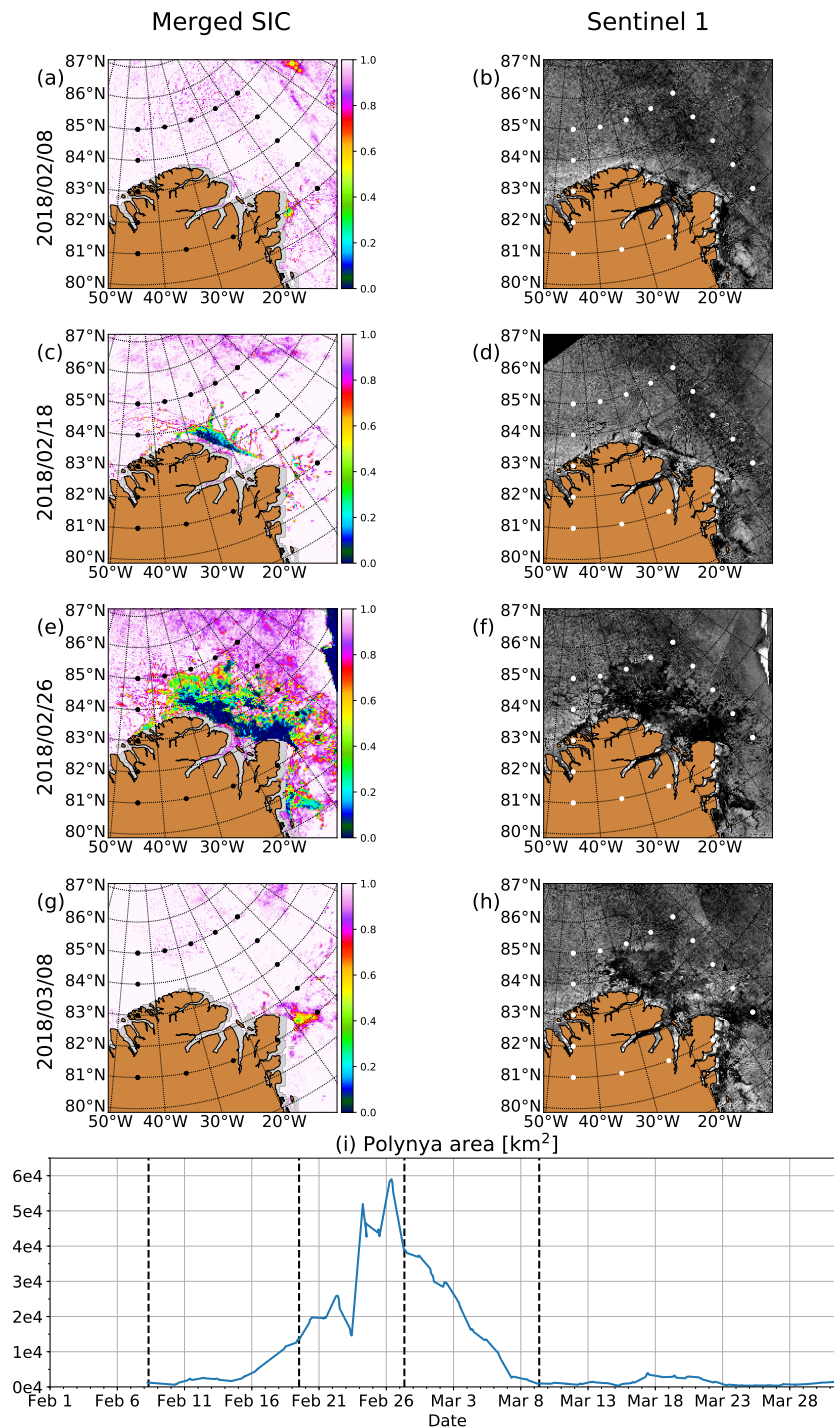


Figure 7.2.: a), c), e) and g): Merged SIC before, at the beginning, at the maximum and after the refreezing of the polynya. The MODIS/ASI pairs were acquired at 07:50/07:44 on February 8th, at 11:45/11:39 on February 18th, at 09:15/09:11 on February 26th and at 11:30/11:28 on March 8th. All times are a.m. and UTC. b), d), f) and h): Corresponding Sentinel-1A/B daily mosaics. The colorbar units are greyscale values. i): Time series of the polynya area. The polynya area is calculated as sum of the open-water fraction ($1 - \text{merged SIC}$) in the map area, multiplied with the respective grid cell size. All available granules are shown. The acquisition times of a), c), e) and g) are marked by the vertical dashed lines.

7.2. Intercomparison of sea-ice concentration datasets

The advantage of fine-resolution SIC datasets and the differences between the single-sensor datasets are illustrated in this subsection. The ASI SIC, MODIS SIC, merged SIC and SAR SIC are compared in Fig. 7.3 a–d.

West of the polynya, the MODIS SIC are lower than the ASI SIC. The merged SIC preserve the ASI mean and are thus higher than the MODIS SIC and spatially continuous if there are no MODIS data available. The benefit of including the MODIS data can be seen when looking at the leads which open west of the polynya: They are much more clearly resolved in the merged product.

The finer resolution is illustrated in the cumulative frequency distribution in Fig. 7.3 e in more detail. The SAR SIC are the only product which shows 0 % SIC as they have the finest spatial resolution and are based on a binary product. Additionally, a lead covered by very thin, smooth sea ice would still be classified as „open water“. These leads show up as reduced SIC of around 20 % in MODIS SIC. The broader leads are also resolved by ASI and show up as SIC between 70 and 80 %. ASI retrieves only few values in the range between 40 % and 60 %. The higher amount of SIC between 60 % and 80 % reflects that the merged SIC resolves leads more finely than ASI.

Over the polynya region, the MODIS SIC and the SAR SIC are higher than the ASI SIC. While ASI retrieves 0 % SIC at the onshore side and 20 % at the offshore side of the polynya, MODIS retrieves 40 % SIC at the onshore side and 80 % at the offshore side of the polynya. The gradient occurs because the newly formed sea ice is advected away from the coast and pushed towards the northeastern boundary of the polynya. New sea ice forms and piles up at the offshore side of the polynya.

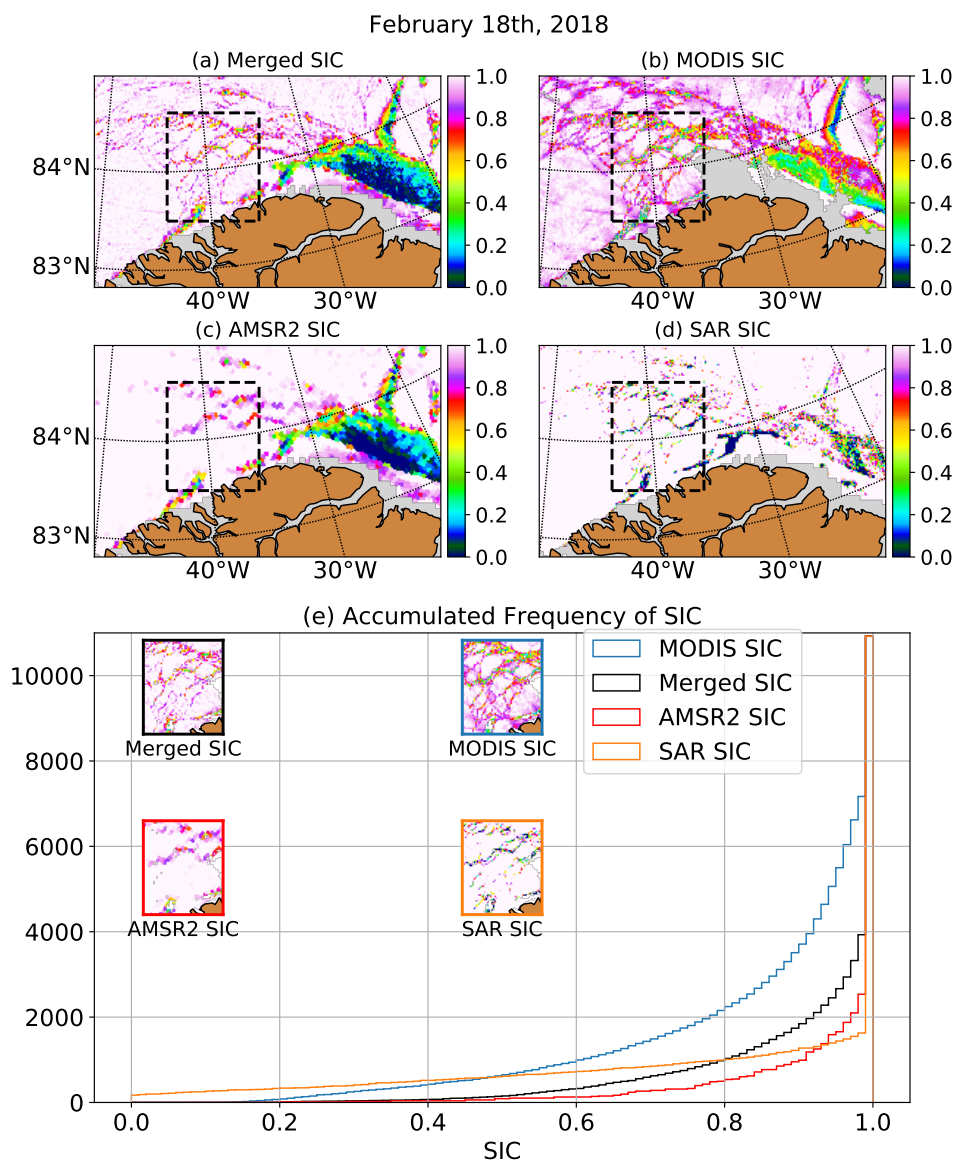


Figure 7.3.: SIC on February 18th, 2018 observed with a) merged, b) MODIS, c) ASI and d) SAR SIC. The acquisition times for MODIS/ASI were 11:45/11:39 am UTC, respectively. The black dashed box in a)–d) marks the region used in Fig. 7.3 e). e) Cumulative histograms for the four datasets. The insets show the SIC distribution for the single datasets. Data points where one of the products was not available were discarded for all products.

Generally, the impact of thin sea ice on the different products can be described as follows: In the very early growth phase, the SAR SIC are close to 0% as long as the sea ice is smooth. When the smooth sea-ice cover breaks up, the backscatter starts to increase and the SAR SIC increases. Additionally, the algorithm was trained with small leads which have a flat surface (Murashkin et al., 2018). In the polynya area, which is larger, the water surface can be rougher and would therefore not be classified as lead. This is

consistent with the SAR SIC only going down to 85 % even at the maximal extent of the polynya (see Fig. 7.4).

The MODIS SIC are low during the early growth phase, but not 0 %. Our explanation is that already frazil ice, the first stage of freshly grown ice, dampens the ocean-atmosphere heat flux, so that the surface air temperature is below the freezing point and thus converted to sea-ice concentration. Additionally, the ice tie-point is expected to be close to the water tie-point, so that small temperature variations can cause large SIC variations. The heat flux decreases non-linearly with increasing sea-ice thickness. The MODIS SIC are thus very sensitive to sea-ice thickness during the early formation phase of sea ice, but the dependence decreases as the sea-ice thickness increases. Note that the sensitivity is not linked to a certain sea-ice thickness, but rather to the distribution of sea-ice thickness: If there are two thickness classes in the region used for the MODIS ice tie-point retrieval (see section 4.1) and the thinner class is thin enough to permit ocean heat flux, sea ice pertaining to the thinner class will show up as reduced SIC.

The ASI SIC are sensitive to sea-ice thicknesses up to 10 cm (Heygster et al., 2014). The merged SIC are less sensitive to sea-ice thickness than the MODIS SIC because they are tuned to preserve the ASI SIC mean. However, because they also include the MODIS information, they still have some sensitivity to sea-ice thickness above 10 cm. The different sensitivities to sea-ice thickness are further illustrated in the time series of the mean SIC in Fig. 7.4.

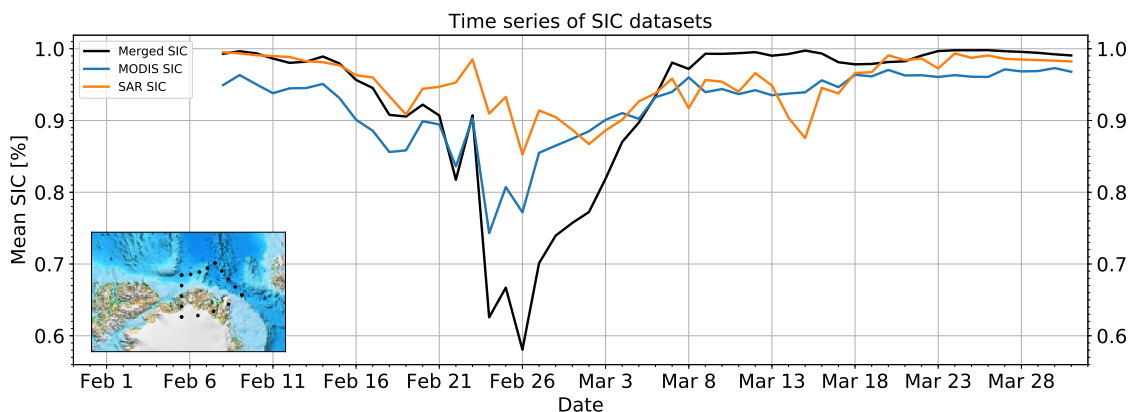


Figure 7.4.: Time series of the mean merged, MODIS and SAR SIC in the polynya region. The ASI SIC are not shown because their mean is equal to the mean of the merged SIC by definition. Only points where all datasets were available have been considered. The map in the lower left shows the region which was considered for the time series as dotted polygon.

Note that the mean of the ASI SIC is not shown because it is equal to that of the merged SIC by definition (see section 4.2). The MODIS SIC are lower than the merged SIC while the polynya opens and after it has frozen over. This reflects that they are more

sensitive to the sea-ice thickness and thin sea ice is shown as reduced sea-ice concentration. During the peak of the polynya area, they are larger than the merged SIC. Here, they are more sensitive to freshly grown sea-ice. Also, they are more sensitive to small sea-ice surface temperature variations because the range between the sea-ice tie-point and the water tie-point gets very small.

The SAR SIC are also larger than the ASI SIC during the peak of the polynya area. The reason is again that they are more sensitive to newly formed sea ice than the merged SIC. While recently formed sea ice is retrieved as low SIC by the merged SIC, it increases the backscatter as soon as it breaks up. Due to the drift within the polynya, it is expected that the sea-ice surface is not smooth, but breaks up quickly. Additionally, as mentioned above, the algorithm was not trained to classify rough surfaces as water.

To demonstrate the benefit of the finer resolution of the merged product compared to the ASI SIC, we show the open-water extent in Figure 7.5.

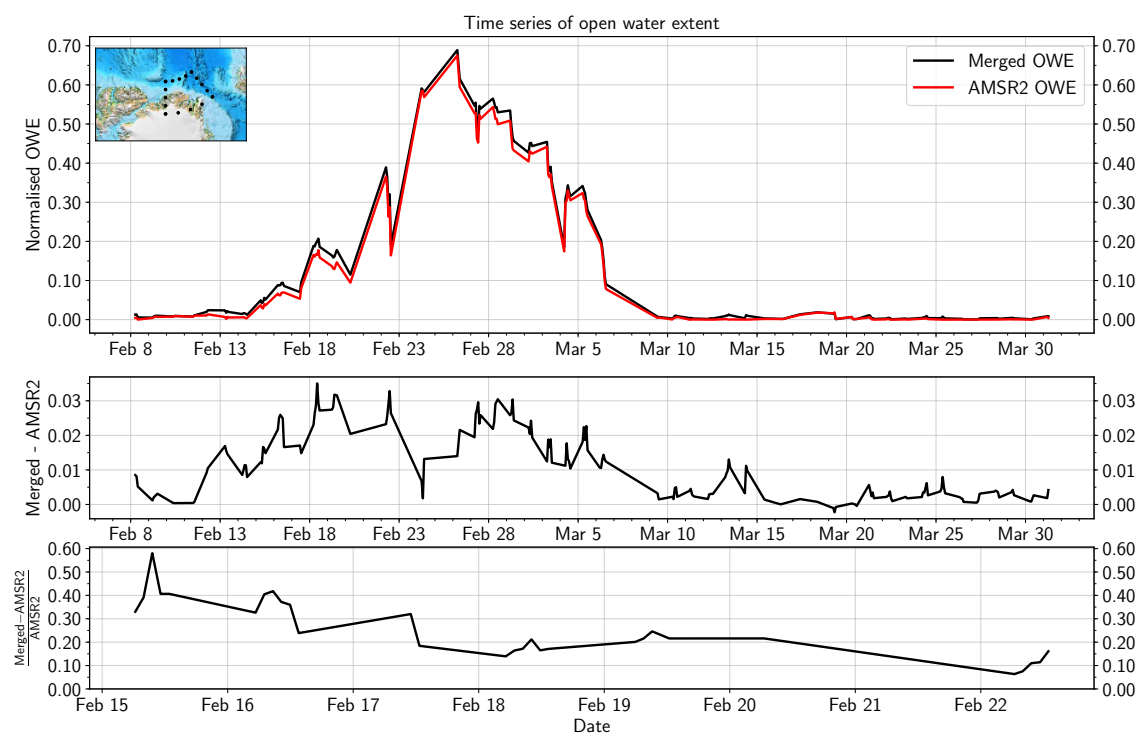


Figure 7.5.: Time series of the merged and ASI open-water extent. The upper panel shows the open-water extent for both datasets. It was normalised to the number of cloud-free pixels. The middle panel shows the difference of the merged and the ASI open-water extent. The lower panel shows the normalised difference of the two datasets during the opening phase. Mind the different time span of the lower panel. Only points where MODIS data were available were considered for all three panels.

The open-water extent is the area covered by all pixels which have at least 15 % open

water. Consider a typical ASI grid cell of 5 km by 5 km with an ASI open-water fraction of 10 %. Our 1 km resolution dataset allows the retrieval of 25 different open-water fractions in this grid cell whose mean would still amount to 10 %. However, single cells may have an open-water fraction above 15 %, so that the open-water extent is expected to be higher for a dataset with finer resolution. A comparison of the time series shows that the difference between the two datasets is small during most of the time. It is 2-3 % while the polynya is open and close to 1 % after it has been closed. The benefit is more apparent when comparing the datasets relative to each other, as shown in the lower panel of Fig. 7.5. The normalised difference is largest during the very early opening phase and smaller towards the end of the opening phase.

7.3. Environmental conditions

Polynyas can open due to two reasons: The sea ice can drift away, which would be typical for a latent heat polynya, or it can melt, which would be typical for a sensible heat polynya. This section describes and analyses the 2 m air temperature and surface air pressure (subsection 7.3.1) and the sea-ice drift pattern (subsection 7.3.2) associated with the polynya.

7.3.1. Air temperature and surface air pressure

Local air temperatures (see Fig. 7.6) at the autonomous weather station in Cape Morris Jesup in 2018 were above the 2010–2017 average from February 15 to March 8. This is in line with the opening and refreezing of the polynya. The air temperature increased rapidly at the beginning of the polynya period. During the formation of the polynya, the air temperature varied by more than 10 °C from day to day and crossed the freezing point on nine out of ten days between February 16th and 25th. The air temperature decreased as soon as the polynya started to refreeze and reached the average value on March 8th. Above-average air temperatures during this time of the year have occurred before, for example in 2011 and 2013 (see Fig. 7.6). However, those lasted only up to five days and not ten days like during the event studied here.

On a larger spatial scale, Fig. 7.7 and Fig. 7.8 show the air temperature and surface air pressure distribution during the formation phase (February 22nd to 26th) and the refreezing phase (March 2nd to 4th) of the polynya. During the formation, the air temperature was up to 20 °C above the average in the polynya region, which corresponds to more than two standard deviations. This was not only a local phenomenon, but associated with a warm-air intrusion from the Atlantic Ocean which caused anomalously high air temperatures until beyond the North Pole (see Fig. 7.7 a).

The surface air pressure distribution completes the picture: There was a high-pressure system over the Barents and Kara Sea which persisted until February 26th. The surface

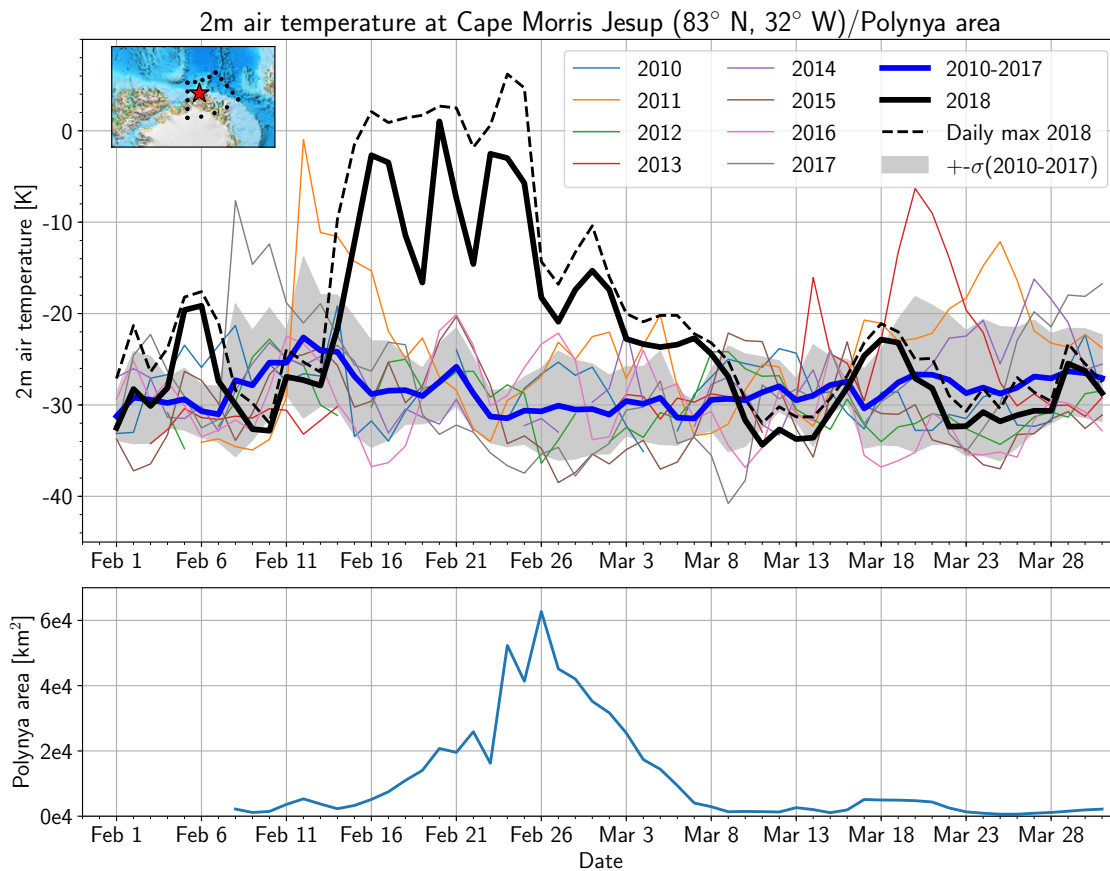


Figure 7.6.: Upper plot: Daily average of 2 m air temperature data at the Danish Meteorological Institute’s weather station at Cape Morris Jesup since 2010. The blue line shows the mean air temperature of the years 2010–2017, the black line shows the air temperatures in 2018. The thin lines represent the single years. The shades indicate the standard deviation of the air temperatures in the years 2010–2017. The box and star in the map mark the region of the polynya event and the location of the Cape Morris Jesup Station, respectively. Lower plot: Time series of the polynya area from Fig. 7.2, but with daily means instead of all granules.

air pressure was 30–40 hPa above average, which is more than two standard deviations (see Fig. 7.7 f). This is the period when the polynya opening rate increased (see Fig. 7.2 i). The high-pressure system caused northward winds over the Greenland Sea which contributed to the opening of the polynya. Furthermore, it caused the advection of warm air from the mid-latitudes towards the Arctic region.

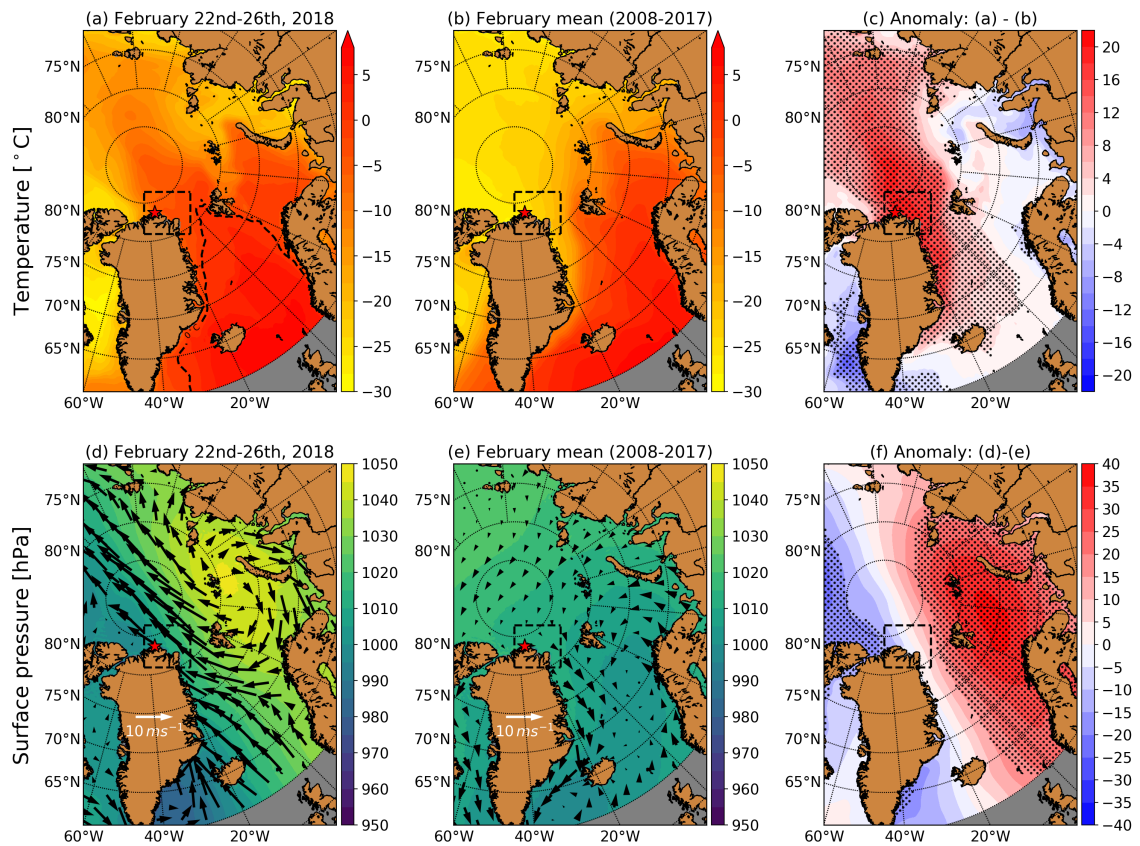


Figure 7.7.: a) ERA5 2 m air temperature from February 22nd to February 26th, 2018, together with the 0° C isotherm. The box and star in the map mark the region of the polynya event and the location of the Cape Morris Jesup Station, respectively. b) February mean ERA5 2 m air temperature between 2008 and 2017. The 0°C isotherm is shown as dashed line. c) Difference between a) and b). Black dots mark points where the air temperature in 2018 was more than two standard deviations above/beneath the 2008–2017 average. d) ERA5 surface air pressure distribution from February 22nd to February 26th, 2018. The black arrows give the ERA5 10 m wind. e) Same as d), but for the February mean surface air pressure between 2008 and 2017. f) Difference between d) and e). Black dots mark points where the surface air pressure in 2018 was more than two standard deviations above/beneath the 2008–2017 average.

Ten days later, the atmospheric state had changed substantially (see Fig. 7.8). The air temperature dropped down to the mean of the previous years. The surface air pressure was high over the Central Arctic and lower over the Eurasian Arctic. This caused southward winds which contributed to the closing of the polynya, together with the Transpolar Drift. Although the air temperature was far above average, it was not high enough to explain the polynya. It only crossed the freezing point for some hours (see Fig. 7.6), but cannot have melted the thick multi-year ice north of Greenland. We conclude that the sea ice must

have been broken up by sea-ice drift. This is consistent with the study of Moore et al. (2018). They found that the thermodynamic sea-ice production was always positive, while the sea-ice motion caused the net loss of sea ice. The warm-air intrusion between February 13th and March 3rd (see Fig. 7.6 and 7.7) contributed to maintaining the polynya open because the warm air temperatures slowed down the refreezing. However, the warm-air intrusion did not contribute to the opening itself.

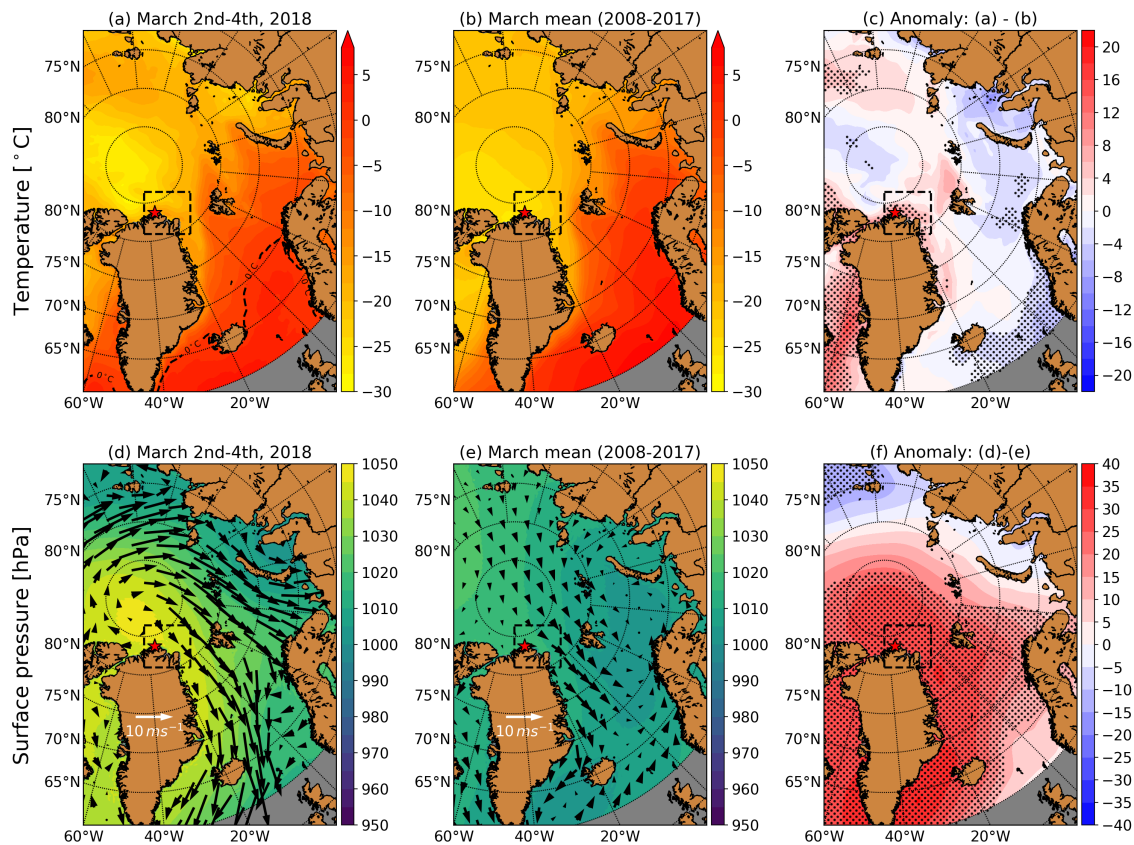


Figure 7.8.: a) and d): Same as Fig. 7.7, but for March 2nd–4th. b) and e): Same as Fig. 7.7, but for the March mean. c) and f): Difference between a) and b) respectively d) and e)

7.3.2. Sea-ice drift

Having found that melting cannot have been the reason for the polynya, we use OSI SAF sea-ice drift data between the opening of the polynya (February 14th) and the end of our study period (March 31st) to investigate the dynamic drivers of the polynya. In general, the Transpolar Drift exports the sea ice to the Atlantic Ocean via Fram Strait. During the polynya event, however, this sea-ice drift pattern was reversed. Where there is normally southward flow, there was northward flow while the polynya opened (see Fig. 7.9 a, b).

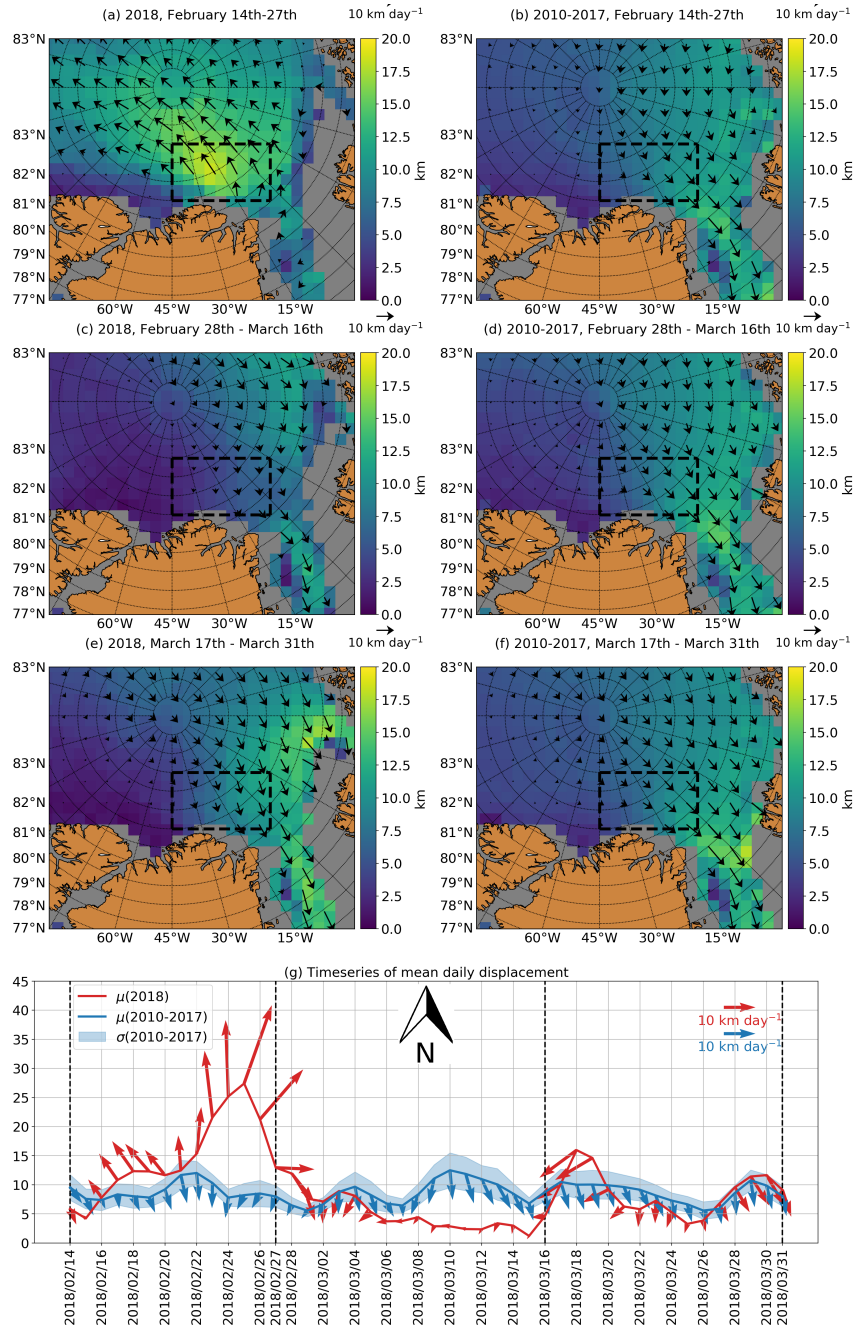


Figure 7.9.: Daily displacement based on the OSI SAF drift product in the polynya region between February 14th and March 31st. The periods February 14th–27th, February 28th–March 16th and March 17th–31st in 2018 are considered in a), c) and e). The same periods, but for the mean between 2010 and 2017 are considered in b), d) and f). The vectors in a)–f) show the mean sea-ice drift velocity in the corresponding periods, where velocity is defined as displacement per day. g) shows a time series of the displacement (lines), the standard error of the sea-ice drift between 2010 and 2017, defined as standard deviation divided by the square root of the number of years (blue shades) and the sea-ice drift velocity (vectors). The orientation is such that an upward-pointing vector points towards North. The arrows in the top right give the scale of the arrow length. Displacement and sea-ice drift velocity are the averages in the black dashed boxes in a)–f).

The sea-ice drift was not only to the opposite direction than usual, but also stronger: The sea ice moved by more than 14 km d^{-1} over a period of almost two weeks. This is 50 % more than in the eight years before on average (see table 7.1). Afterwards, the sea-ice drift direction changed to normal conditions, i. e., southeast, and there was below-average displacement in the first half of March (see Fig. 7.9 c, d). During the second half of March, the sea-ice drift was about average (see Fig. 7.9 e, f). The mean sea-ice displacement and the sea-ice drift angle for 2018 and 2010–2017 are given in Table 7.1. The sea-ice drift angle is the orientation of the sea-ice drift towards North and is counted counter-clockwise, so that a sea-ice drift angle of 90° means westward movement.

Because of the south-southwestern sea-ice drift direction, the sea ice was not completely exported towards the Fram Strait in south-east direction. Instead, it partly returned to the polynya region. Here, we assume that it got rafted and ridged with the newly formed sea ice in the polynya area. This matches the observation of strong southwestern sea-ice drift between March 16th and March 20th (see Fig. 7.9 g). We therefore expect a mix of thermodynamically grown, flat sea ice and rough sea ice grown due to sea-ice deformation at the end of March.

The polynya event can be summarised as follows: In February, the sea ice broke apart and was transported northwards. In the first half of March, the sea-ice drift was weak and there was rapid thermodynamic sea-ice growth in the resulting open water of the polynya since air temperatures were almost 30°C below the freezing point (see Fig. 7.6). In the second half of March, parts of the sea ice which had moved northwards in February returned to the area, mainly during one event between March 16th and March 20th, where the sea-ice drift was strong and directed towards Southwest, i. e., towards the Northern Greenland coast.

	2018	2010–2017	2018	2010–2017
	Displ.[km]	Displ.[km]	Angle[°]	Angle[°]
Feb 14th – Feb 27th	14.4	8.9 ± 1.9	359.4	186.5 ± 8.2
Feb 28th – Mar 16th	4.9	8.7 ± 1.9	157.9	187.5 ± 6.2
Mar 17th – Mar 31st	8.7	8.7 ± 1.8	165.5	194.8 ± 12.9

Table 7.1.: Mean daily displacement and sea-ice drift angle in the dashed box shown in Fig. 7.9 a–f, calculated based on the OSI SAF drift product. For the period 2010–2017, the standard error (defined as the standard deviation divided by the square root of the number of years) is given as well. The angles give the mean orientation of the sea-ice drift vectors towards north. The counting goes counterclockwise, so that a sea-ice drift angle of $0^\circ/90^\circ/180^\circ/270^\circ$ corresponds to purely north-/west-/south-/eastward sea-ice drift, respectively.

7.4. Processes

This section is dedicated to the processes in the polynya: We estimate the amount of sea ice grown in the polynya and the heat released to the atmosphere. To estimate sea-ice growth, we calculate the accumulated thermodynamic sea-ice growth assuming calm, snow-free conditions. We employ the freezing degree day parameterisation of Lebedev (1938). The calculations start on February 14th, when the first leads were visible in the merged SIC product. This is compared to AEM sea-ice thickness measurements taken on March 30th and 31st (see subsection 3.5.4) and to the simulations of thermodynamic growth by the NAOSIM model (see subsection 3.5.3). Also, the estimates of thermodynamic growth are compared to the SMOS/SMAP sea-ice thickness product of the University of Bremen (Patilea et al., 2019). For a consistent comparison despite the different grids, we define the polynya area as the area of all pixels which had less than 50 % SIC on the respective grid at least once during the event as described in section 3.5.1.

The accumulated sea-ice growth calculated from the freezing degree days increased strongly over the first days while the polynya opened and then slowed down (see Fig. 7.10). This is expected because the heat flux decreases non-linearly with sea-ice thickness once the sea ice starts to grow. As air temperatures decreased, sea-ice growth increased until the accumulated sea-ice growth at the end of March was 65 cm. The NAOSIM accumulated sea-ice growth increased slowly during the opening of the polynya. Then, it increased strongly from February 25th to March 1st. After that, the accumulated sea-ice growth increased slowly to 60 cm at the end of March.

The SMOS/SMAP sea-ice thickness is dominated by dynamic processes during the opening of the polynya. Also, the SMOS/SMAP algorithm assumes 100 % SIC (Patilea et al., 2019; Huntemann et al., 2014), which is not the case here. During the opening, it can therefore not be compared to the estimates of pure thermodynamic growth. After the refreezing started, it evolved synchronously to the accumulated thermodynamic sea-ice growth from the freezing degree day parameterisation until both datasets showed sea-ice thicknesses of 50 cm. Since the SMOS/SMAP algorithm does not retrieve sea-ice thicknesses above 50 cm (Huntemann et al., 2014; Patilea et al., 2019), we cannot compare the two thermodynamic estimates to the SMOS/SMAP sea-ice thickness product after March 20th (see Fig. 7.10).

In addition to sea-ice growth, we estimate the thermodynamically produced sea-ice volume by multiplying the accumulated growth rates from Fig. 7.10 with the maximum area covered by the polynya. For the maximum area, we again consider all points where the sea-ice concentration dropped beneath 50 % at least once during the polynya event. The freezing degree day parameterisation yields a sea-ice volume of 33 km³, NAOSIM yields a sea-ice volume of 15 km³. This can be explained because the area of the polynya in the model is only half as big compared to the observations (not shown here). Furthermore, we use NAOSIM to model the heat released to the atmosphere (see Fig. 7.10 b). It is closely

coupled to the opening and closing of the polynya. It is negative, i. e., directed from the ocean to the atmosphere, throughout the entire event. The average/maximum daily heat flux was $-40/-124 \text{ W m}^{-2}$. The time-integrated heat flux was -866 W m^{-2} . The actual heat flux may have been larger as the model polynya area is smaller than the one we observe from the satellite data, as mentioned above.

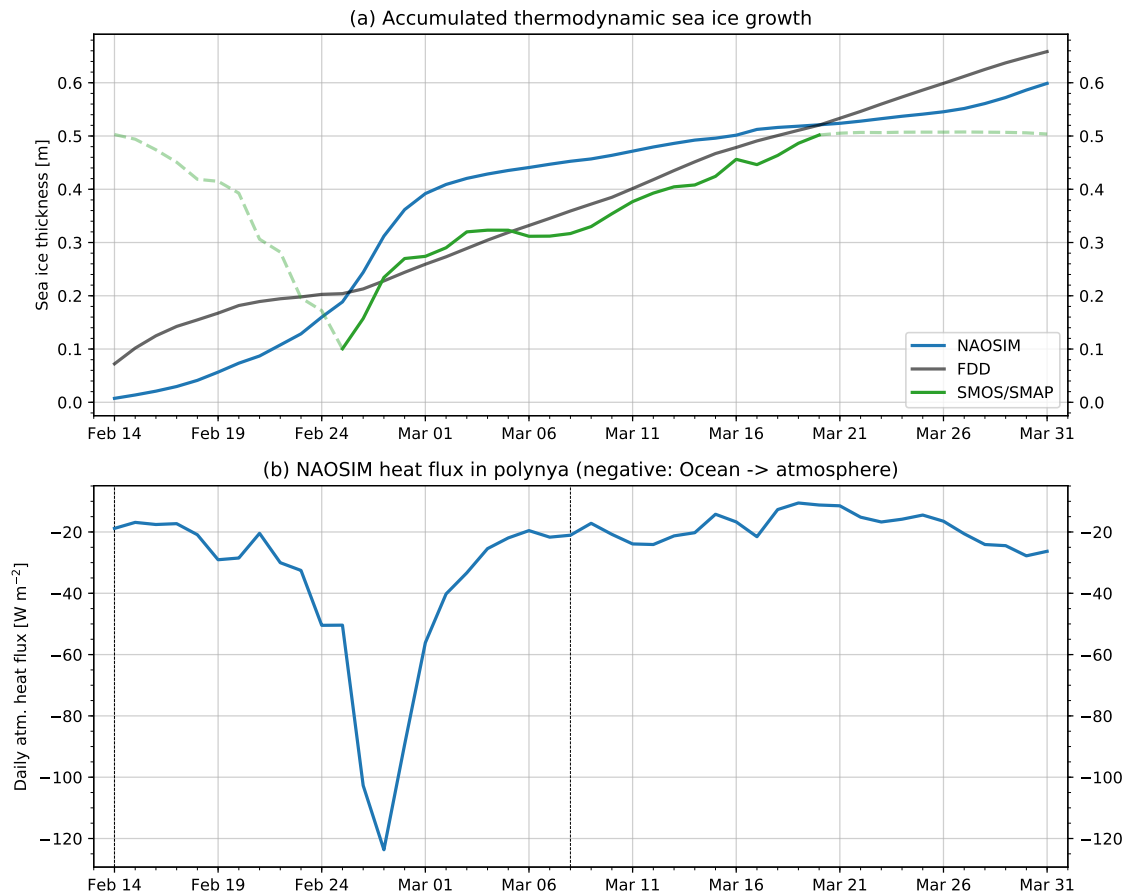


Figure 7.10.: a) Accumulated thermodynamic sea-ice growth after February 14th modeled by NAO SIM and estimated using the freezing degree day parameterisation. The SMOS/SMAP passive microwave sea-ice thickness product of the University of Bremen is shown for comparison. Days before the refreezing started are marked by the faint dashed line. the same holds for the days after the algorithm reached its maximally retrievable sea-ice thickness. b) Spatially averaged atmospheric heat flux, defined negative upward (blue line) during the polynya period (vertical dashed lines).

Figure 7.11 compares the accumulated thermodynamic sea-ice growth to the sea-ice thickness measured by three AEM flights on March 30th and 31st. Their modal/mean value was 1 m/1.94 m with a smaller mode at 5 cm. The small mode is caused by refrozen leads covered with dark and light nilas which were observed visually during the flights

(personal communication, Christian Haas). This explains the presence of classes of very thin sea ice adjacent to the open leads. The tail of the frequency distribution in Fig. 7.11 represents deformed sea ice rather than purely thermodynamically grown flat sea ice. The main mode of a sea-ice thickness distribution is usually associated with the thermodynamically grown sea ice (Haas et al., 2010). We note that there is a difference of the main mode of the AEM measurements of 1.0 m which normally represents the thickness of the most abundant, thermodynamically grown sea ice (e.g. Haas et al. (2010)), and the 0.60 m and 0.65 m obtained by the NAOSIM and freezing degree models, respectively. This difference can be due to insufficient heat flux assumptions in the models, in particular unrealistic ocean heat flux, or it can indicate that much of the level sea ice in the polynya was also formed by rafting, which could increase level sea-ice thickness much above the thermodynamically achievable thickness. However, the much larger mean AEM sea-ice thickness of 0.94 m above the modal sea-ice thickness demonstrates the importance of dynamic sea-ice growth by sea-ice convergence and compression as a result of the closing of the polynya.

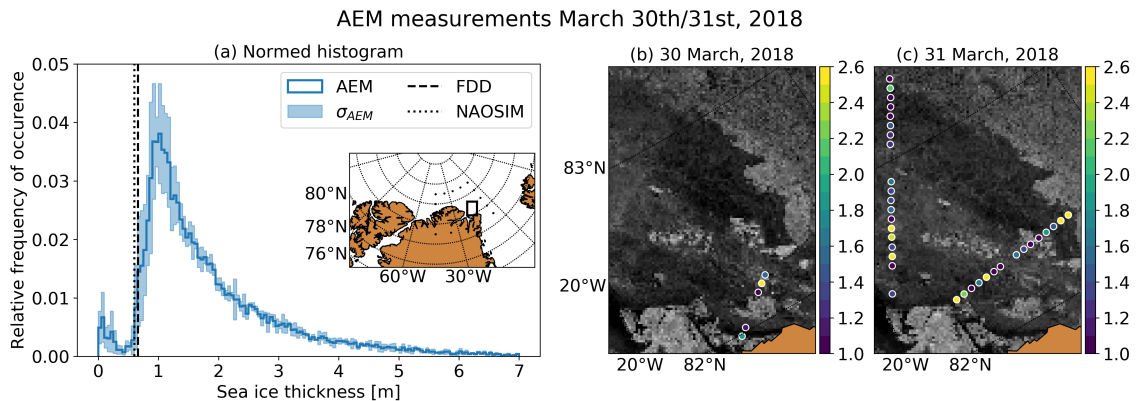


Figure 7.11.: AEM measurements of the thickness of young first year ice formed in the polynya until the end of March. a): Normalised histogram of the AEM measurements. The shades indicate the standard deviation of the three single flights. The black vertical line shows the mean sea-ice thickness calculated based on freezing degree days since February 14th. The dotted polygon shows the region of the polynya. The small black rectangle shows the region of the AEM flights. b) and c): AEM flights on March 30th and 31st. The dots show the AEM measurements, averaged every 5 km. The background shows a Sentinel-1 mosaic for the respective day.

7.5. Discussion

Comparing the 2018 polynya north of Greenland to the climatology between 1979 and 2017, we find that the SIC in the polynya area during the peak period between February 25th and February 27th were the lowest observed during any day between November and

April since 1979. This confirms the findings of Moore et al. (2018) who showed that the mean February SIC 2018 was smaller than any mean February SIC between 1979 and 2018. We confirm and further strengthen the findings of Moore et al. (2018) as we include the entire winter season in our comparison and add more direct sea-ice observations from satellite and helicopter-borne remote sensing. The 2018 winter polynya thus was a first-time event which had influence on the regional sea-ice production and ocean-to-atmosphere heat flux as will be discussed below. An event as strong as this never happened before during the satellite period. The 1979–2017 all-time minima curve in Fig. 7.1 accumulates all potential polynya events during that period. We identify clear but smaller polynya events like in 1986 in mid December. Improved monitoring of these events is possible with the fine-resolution, spatially continuous SIC dataset which we present in this thesis.

By comparing the merged, MODIS and ASI SIC, we find that ASI SIC are higher than MODIS for high SIC. As the merged SIC preserve the ASI SIC mean, this also holds for the merged SIC. The differences between the MODIS and the ASI SIC arise because the algorithms have different sensitivities to sea-ice thickness: ASI is based on the polarisation difference which is independent of the sea-ice thickness if the sea ice is thicker than 10 cm (Heygster et al., 2014). The MODIS SIC algorithm was designed under the premise that the area used for the ice tie-point retrieval only contains one ice thickness class. If it contains more than one sea-ice thickness class and the thinner class is thin enough to permit significant ocean heat flux to reach and warm the ice surface, this ice class will be reported as reduced SIC, even when the actual SIC is 100%. Within the 48 km-by-48 km window used for the derivation of the sea-ice tie-point, the sea-ice thickness is expected to vary, especially during and after a dynamic event like the polynya which we investigate. This is also the reason why the MODIS SIC are lower than the merged SIC before and after the maximal extension of the polynya (see Fig. 7.4). The SIC underestimation is tolerated by Drüe and Heinemann (2004) because the algorithm was designed to derive the thermal surface conditions rather than the actual surface ice fraction. However, the SIC underestimation causes a discrepancy when compared to ASI SIC. The described dependence of the MODIS SIC on sea-ice thickness and the fact that the SAR SIC also are close to 100% let us conclude that the ASI SIC are closer to the true SIC here. Thus we merge the ASI SIC and MODIS SIC, keeping the ASI SIC on a larger scale but adding the finer resolution of the MODIS SIC to resolve smaller leads and openings.

Comparing the histograms of the SIC datasets, we find that the leads west of the polynya tend to be smeared out by the ASI SIC. This is caused by the coarser spatial resolution of ASI and not a deficiency of the algorithm. It illustrates that the merged SIC are better than ASI or MODIS SIC alone. Using only MODIS SIC would mean an underestimation of the SIC in many cases, as described above, and would be limited to cloud-free scenes. Using only ASI SIC would result in smearing out narrow leads. Also, refrozen leads which are covered by snow or sea ice which is thicker than 10 cm would not be identified (Heygster et al., 2014; Shokr and Kaleschke, 2012). The merged product's magnitude is closer

to the SAR SIC than the MODIS SIC and at the same time it preserves most of the fine-resolution spatial information of the MODIS data. The SAR SIC themselves are well-suited as a reference product above the region west of the polynya due to their fine spatial resolution. However, larger open water areas like the polynya itself can be misclassified due to, e. g., wind roughening effects. Also, SAR data are only available locally. Thus, the merged SIC are the only product which combines fine spatial resolution, spatial coverage and daily Arctic-wide coverage.

Over the polynya region, we find that the SAR and MODIS SIC are higher than the ASI SIC. As the air temperatures were still below freezing, it is likely that sea-ice production started shortly after the opening. The wind and sea-ice drift patterns hindered the evolution of a homogeneous sea-ice cover and the newly formed sea ice was likely turned into grease and pancake ice. Under these circumstances, it may be that ASI does not retrieve the grease ice. The grease ice would, however, change the backscatter signature, so that the polynya is no longer recognised as such by the SAR SIC. Additionally, a rough water surface can be misinterpreted as ice by the SAR SIC algorithm as it was trained to retrieve small leads which generally have a smooth surface. The grease ice also shows up as increased MODIS SIC. Another reason for higher MODIS SIC is that the sea-ice tie-point is derived based on the local sea-ice surface temperature anomaly. If the surrounding sea-ice surface temperature is only slightly below freezing, the range between the dynamic sea-ice tie-point and the fixed water tie-point gets small and small sea-ice surface temperature variations cause high SIC variations. The described sensitivity of the MODIS and SAR SIC to very freshly grown sea-ice is also the reason why they are lower during the maximal extension of the polynya (see Fig. 7.4). It may be that we underestimate the SIC here by tuning MODIS SIC to the ASI SIC as we get SIC between 0% and 20%, although the actual concentration of grease ice is probably higher. We tolerate this as a trade-off because the approach allows better retrieval of higher SIC and a spatially continuous field. The advantage of the finer resolution of the merged SIC product is shown in Figure 7.5. It is most pronounced during the early break-up and less pronounced towards the end of the opening phase. The reason is that small leads which are formed while the polynya breaks up are resolved by the merged product, but not or only hardly by the ASI SIC. This is caused partly by the finer resolution of the merged product and partly because the MODIS SIC can retrieve refrozen leads which are not retrieved by the ASI SIC any more.

Strictly speaking, a refrozen lead should not be visible in a SIC product, i. e., have a SIC of 100% as soon as it refreezes. While the sea ice is thin (approximately thinner than 10 cm), a lead will likely be shown as reduced SIC in our merged product as the ASI SIC are influenced by sea-ice thickness (Heygster et al., 2014; Wiebe et al., 2009). For new sea ice in leads, the brine on top of the ice and the thin sea-ice thickness influence the brightness temperatures measured by the passive microwave radiometer, which can lead to a reduced SIC retrieval. While the sea ice is growing, this effect gets reduced and when the sea-ice thickness exceeds approximately 10 cm, the lead would appear as 100%

SIC in a pure ASI SIC product. In our merged product, however, it may still appear as reduced SIC. This is due to the influence of thin sea ice on the MODIS SIC (Drüe and Heinemann, 2004) which is stronger than the influence on the ASI SIC. In this case, we could set the SIC to 100 % to be fully consistent with the definition of SIC, but we decide to keep this additional lead information. The rationale for this is that for many applications and processes, e.g. navigation or heat flux calculations, the presence of leads is highly relevant. We thus accept being slightly inconsistent with the definition of sea-ice concentration as a trade-off for conveying the lead information to the user. A step forward in future could be to add a flag to our product which tells the user that the ASI SIC at the respective pixel is 100 %, meaning that the lead is already refrozen. This flag would also convey information about the sea-ice thickness: It would indicate that the sea ice is thick enough to be retrieved as 100 % SIC by ASI, i. e., thicker than approximately 10 cm, but still thin enough to be retrieved as reduced SIC by MODIS.

Next, we look into the spatial and temporal evolution of the polynya and the environmental conditions. At its maximal extent, it spanned more than 60,000 km². The mean size during the opening was 11,000 km². This is slightly larger than the average size of 17 recurring Arctic polynyas reported by Preußner et al. (2016). They find sizes between 400 and 43,600 km², but at different locations.

The opening of the polynya was driven by anomalous sea-ice drift. It was directed northwards where it is normally directed southwards. Besides, the sea-ice drift speed was 14 km d⁻¹, which is 50 % stronger than in the eight years before. Also, other studies (Kwok et al., 2013; Vaughan et al., 2013) find typical sea-ice drift speeds between five and 10 km d⁻¹ in this region. During the second half of the opening period, the sea-ice drift anomaly was caused by a persistent high-pressure system above the Eurasian Arctic.

The sea-ice drift pattern during the polynya event has also been analysed by Moore et al. (2018). They use data of the Pan-Arctic Ice Ocean Modeling and Assimilation System (PIOMAS) (Zhang et al., 2003). We can only compare our findings indirectly because they look at the sea-ice thickness change due to sea-ice motion, while we look at the sea-ice drift directly. Still, the temporal evolution is consistent: They identify a first peak on February 16th and a second, stronger one on February 23rd and 24th. In our sea-ice drift time series, the peaks are one to two days later. The event on March 3rd during which the sea ice was partly returned to the polynya area is also visible in their data. Since their time series ends on March 5th, further comparison is not possible.

We found that the surface-air-pressure distribution during February and March was coincident with the opening and closing of the polynya. Moore et al. (2018) identify the surface pressure distribution and the associated warm-air intrusion as surface response to a sudden stratospheric warming which occurred in early February. The high-pressure system caused northward winds in the polynya area and increased the opening rate. The warm-air intrusion from the mid-latitudes featured air temperatures up to 20 °C above the average, visible in both reanalysis data and local measurements. The heat released by

the polynya contributed to the anomaly.

Other studies (Graham et al., 2017; Woods and Caballero, 2016; Moore, 2016; Mewes and Jacobi, 2018) report that such winter warming events have occurred since the 1950s, but did not last as long and were weaker than in recent years. Also, they were not related to polynyas. Even if the 2 m air temperatures in our case were exceptionally high, they were below/only slightly above the freezing point. The advected air temperature anomaly contributed to the polynya development only indirectly: It slowed the sea-ice growth, but did not prevent sea-ice growth totally and did not melt the sea ice. This is again consistent with the results of Moore et al. (2018) who show that the thermodynamic sea-ice production was always positive, i. e., no sea-ice melt occurred. After the air pressure distribution changed, the sea-ice drift was directed towards Fram Strait as usual and air temperatures were 20 °C below the freezing point. The polynya refroze and closed quickly.

We identify two periods of enhanced sea-ice drift directed towards the Northern Greenland coast in the beginning and in the second half of March (see Fig. 7.9). These closing events have caused deformation of the newly formed sea ice in the polynya. At the end of March, the polynya was covered by a mixture of multi-year ice from before the event, deformed newly grown young ice and flat new ice (see Fig. 7.11). Our estimate of thermodynamic sea-ice growth (60 cm modeled by NAOSIM, 65 cm estimated by the freezing degree day parameterisation) for March 31st is thus likely an underestimation of the actual sea-ice thickness due to the sea-ice thickening by deformation. This is confirmed by comparing these estimates to AEM sea-ice thickness measurements at the end of March, which found a modal sea-ice thickness value of 1 m as well as a tail towards higher sea-ice thicknesses due to deformation.

The agreement between the freezing degree day parameterisation, the SMOS/SMAP sea-ice thickness and the NAOSIM sea-ice thickness during the refreezing period is good. For SMOS/SMAP and the freezing day parameterisation, this is partly because the SMOS/SMAP algorithm was trained using this parameterisation (Huntemann et al., 2014; Patilea et al., 2019). The air temperature was beneath 0 °C and thus the warm-air intrusion did not influence the sea-ice thickness retrieval during the refreezing. The air temperature was only above 0 °C during the opening of the polynya, so that this, and maybe the early refreezing phase with sea ice thinner than approximately 10 cm for which passive microwave retrievals of sea-ice thickness and sea-ice concentration are ambiguous and their influence on the signal is hard to disentangle (Ivanova et al., 2015; Heygster et al., 2014), is the only phase where the SMOS/SMAP sea-ice thickness underestimates the actual sea-ice thickness. A quantitative estimate of how much the small ice thickness and sea-ice concentrations beneath 100 % influence the sea-ice thickness retrieval would be beyond the scope of this thesis. We note that the SMOS/SMAP sea-ice thickness during the opening and early refreezing are less reliable than at a later stage of refreezing. It is, however, this later stage of refreezing which we are interested in, which makes the product well-suited for our purposes and the quality of the retrieval good. The only disadvantage here is that

the SMOS/SMAP sea-ice thickness is only valid until a sea-ice thickness of 50 cm (Huntemann et al., 2014; Patilea et al., 2019). Therefore, we can only compare the SMOS/SMAP sea-ice thickness to the other products between February 25th, when the refreezing starts and March 20th, when the SMOS/SMAP sea-ice thickness reaches 50 cm.

By comparing the estimates of the thermodynamically produced sea-ice volume, we find a discrepancy between the freezing degree day parameterisation (33 km^3) and the NAOSIM model (15 km^3). The discrepancy is because the polynya in the model is only half as large as in the observations. A similar finding was presented in Moore et al. (2018), who find that the polynya in the PIOMAS model was significantly smaller than in the observations. Since our observations agreed well with the outline of the polynya in the SAR images, we conclude that the 33 km^3 are the better estimate. This highlights the need for further improvements of the sea-ice models. Preußer et al. (2016) give January-March accumulated sea-ice production rates of 52 km^3 on average for 17 Arctic coastal polynyas. According to Tamura and Ohshima (2011), the ten major coastal polynyas in the Arctic produce between 130 and 840 km^3 per year. Total winter-accumulated sea-ice production in Arctic polynyas has been estimated between 1811 km^3 (Preußer et al., 2016) and 2940 km^3 (Tamura and Ohshima, 2011). However, given that normally sea-ice production north of Greenland is negligible and that the 2018 polynya was only open for three weeks, while the values of Preußer et al. (2016)/ Tamura and Ohshima (2011) are given for three months/an entire year, the event is still remarkable on a regional scale. Finally, we estimate a mean/maximum heat flux of $-40/-124 \text{ Wm}^{-2}$ during the time when the polynya was opened. The mean heat flux is at the lower end of the ranges of mean heat fluxes given by Morales-Maqueda et al. (2004). They report mean heat fluxes between -38 and -105 Wm^{-2} . We attribute this to the warm-air intrusion. When the polynya was opening, the air temperatures were around -10°C , so that the heat flux was comparably small. When the air temperatures decreased to -30°C , the polynya had already started to refreeze, which dampened the heat flux.

8. Summary & Conclusions

The title of this thesis claims that the merged sea-ice concentration product is „More than the sum of its parts“. Is this supported by the results presented in this study? This is answered in this chapter by presenting the major achievements. In doing so, the applied methods and the most important findings are summarised.

The most important steps in this thesis were to:

(i) Improve the MODIS sea-ice concentration retrieval of Drüe and Heinemann (2004)

The MODIS sea-ice concentration is determined by deriving reference temperatures, so-called tie-points, for a pixel covered purely by ice and for a pixel covered purely by water and interpolating the sea-ice concentration linearly if the temperature is between the tie-points. The freezing point of seawater at -1.86°C is chosen as water tie-point. The choice of the ice tie-point, however, is less straightforward as the ice-surface temperature has large horizontal variability. It is thus derived from the ice surface temperature anomaly in a region of 48 km by 48 km. A linear regression with two independent variables is used to assign each pixel an ice tie-point based on its position within the 48 km-by-48 km box. The concept was introduced by Lindsay and Rothrock (1994) and applied to MODIS ice-surface temperatures by Drüe and Heinemann (2004). After determining the tie-points in one 48 km-by-48 km box, they shift the box by 48 km and apply the same analysis. This means that the regression coefficients change abruptly at the border of the two boxes, which introduces physically implausible sharp gradients at the transition. We overcome this by shifting the box in smaller steps. This way, each pixel is covered multiple times and the mean is selected as the ice tie-point. Different stepsizes are tried, but we decide for the smallest possible stepsize of 1 km. This increases the number of iterations and thus the runtime of the processing by a factor of 48. We accept this as a trade-off for the smoother ice tie-point field. Additionally, this has the advantage that the standard deviation of the 48 iterations can be used as estimate for the tie-point uncertainty. The smoother field, the possibility to get an uncertainty estimate and an increased spatial coverage are the main advancements of our version of the algorithm compared to the version of Drüe and Heinemann (2004).

(ii) Assess the impact of the ice tie-point on MODIS sea-ice concentration

To see how the choice of tie-points and their variability influences the MODIS sea-ice concentration, we download 997 MODIS granules covering the Arctic marginal seas between February and May 2019. We calculate the pixel-wise ice tie-point mean and standard deviation as described under (i). Then, we look into the mean standard deviation of the granules. Averaged over all seasons, it is 0.33 K, which corresponds to 1.7% of the dynamic range (difference between water and ice tie-point). Then, we calculate the MODIS sea-ice concentration twice, once with the ice tie-point plus one standard deviation and once with the ice tie-point minus one standard deviation. The difference in sea-ice concentration is on average 1.9% and at maximum 6.2%. We interpret this as the inaccuracy which is introduced by only shifting the box by 48 km and which we overcome by shifting the box by 1 km.

(iii) Assess the impact of the water tie-point on the MODIS sea-ice concentration

The inaccuracy introduced by assuming a constant freezing point as water tie-point, ignoring the effect of varying salinity, is assessed by calculating MODIS sea-ice concentration with freezing point corresponding to salinities ranging between 20 and 34. The average sea-ice concentration difference between assuming a salinity of 20 and assuming a salinity of 34 is only 0.5%. Given that a salinity of 20 is a lower boundary of what would be expected in the marginal seas and the salinity in the Central Arctic varies roughly between 30 and 34, we conclude that the inaccuracy introduced by the assumption of a constant freezing point is negligible. In brackish-water seas with considerably lower salinities, the water tie-point should be adapted to the lower salinities, but can still be assumed to be constant.

(iv) Develop a procedure for merging MODIS and ASI sea-ice concentration

The central assumption for the merging is that the MODIS sea-ice concentration captures the spatial variability at a scale of 1 km correctly, but does not necessarily reflect the correct magnitude. Furthermore, it is only available for clear-sky pixels. The ASI sea-ice concentration, on the other hand, is closer to the correct magnitude and is available independently of cloud coverage and thus spatially continuous. However, ASI can only retrieve sea-ice concentration at a spatial scale of 5 km and does not show overfrozen leads after the initial refreezing. These leads are more readily retrieved from MODIS sea-ice concentration. We thus tune the MODIS sea-ice concentration to preserve the mean ASI sea-ice concentration in a region of 5 km by 5 km. This is done by adding the difference between the two of them on a scale of 5 km to the MODIS sea-ice concentration. In this way, we preserve the spatial distribution of the MODIS data, but tune it to the more correct magnitude of the ASI data. If the mean ASI sea-ice concentration is close to 0% or 100%, it

8. Summary & Conclusions

can happen that it is not entirely preserved. As for the MODIS ice tie-point retrieval, the 5 km-by-5 km region is shifted by 1 km before the merging is repeated. This way, each pixel is covered 25 times. The mean of the 25 iterations is selected as final value. Cloud-covered pixels are set to the ASI sea-ice concentration. This assures spatial continuity at the transition between cloud-covered and cloud-free pixels. Furthermore, by preserving the mean of the ASI sea-ice concentration we make sure that statistical comparisons between the ASI sea-ice concentration and other passive microwave sea-ice concentration algorithms (e. g. Ivanova et al. (2014, 2015); Kern et al. (2019, 2020)) are also valid for our product as far as biases are concerned.

(v) Evaluate the merged, MODIS and ASI sea-ice concentration against independently derived reference sea-ice concentration

For the evaluation, we produce a reference sea-ice concentration dataset from 79 Sentinel-2 scenes by classifying the reflectances into water, thin ice and thick ice. We only use scenes with a time-lag of less than two hours to the next cloud-free MODIS granule, which leaves us with 66 scenes. They cover the period from February 22nd to May 27th and are located in the Arctic marginal seas and in the Fram Strait. The scenes are mostly dominated by a compact sea-ice cover and leads, but also comprise open-water areas. Thin ice is part of the ice cover and should be reproduced as high sea-ice concentration by a sea-ice concentration retrieval. Thus, treating thin ice as ice (thin-ice sea-ice concentration) is the primary reference dataset. Still, the presence of thin ice is relevant for many practical applications, e. g. the calculation of heat fluxes. Therefore, we create a second reference sea-ice concentration dataset to evaluate the sensitivity of our sea-ice concentration retrievals to thin ice. For this dataset, we include the thin ice in the open water class and only consider thick ice as ice (thick-ice sea-ice concentration).

Treating only thick ice as ice yields a mean Sentinel-2 sea-ice concentration of 87.3 %, treating thin and thick ice as ice yields a mean sea-ice concentration of 94.4 %. The standard deviation decreases from 13.2 % (thick-ice sea-ice concentration) to 9.2 % (thin-ice sea-ice concentration). The mean merged and MODIS sea-ice concentration are 93.1 % and 92.8 %, which means that there is closer agreement with the thin-ice sea-ice concentration than with the thick-ice sea-ice concentration. Thus, both retrievals correctly identify thin ice as ice and only show a small underestimation of about 1 % due to the presence of thin ice for the 66 Sentinel-2 reference scenes used for the intercomparison. The RMSD between the merged and MODIS sea-ice concentration is 5 %, which means that the algorithms do yield different results despite the small bias.

We further investigate this by analysing one scene with good-quality MODIS sea-ice concentration and one scene with poor-quality MODIS sea-ice concentration. In the

first case, the combination of the fine resolution of the MODIS sea-ice concentration and the magnitude of the ASI sea-ice concentration used for the merged sea-ice concentration retrieval allows better representation of the reference data than with either dataset alone. In this scene, the merged sea-ice concentration has a smaller difference and a smaller RMSD than the MODIS sea-ice concentration compared to the thin-ice reference dataset, while at the same time the fine resolution causes an open-water extent (area with at least 15 % open water) which is closer to that of the thin-ice sea-ice concentration than that of the MODIS or ASI sea-ice concentration. In the poor-quality MODIS sea-ice concentration case, an unscreened cloud and high ice-surface temperatures deteriorate the quality of the MODIS sea-ice concentration. This is mitigated by the merging, so that the result has a similar quality as the ASI sea-ice concentration alone, however, likely not improving it.

(vi) Identify benefits over single-sensor sea-ice concentration products

Our merged dataset incorporates thermal infrared and passive microwave data. To support the claim that it is „more than the sum of its parts“, it should thus outperform both of the input datasets, as well as other sea-ice concentration products based on thermal infrared or passive microwave observations. This has been briefly touched under point (v), but warrants more extensive discussion since it is the core of this thesis.

The main benefit of the merged dataset over single-sensor passive microwave datasets is the finer resolution. This benefit manifests in a higher open-water extent which is closer to that of the Sentinel-2 and Landsat 8 reference sea-ice concentration, as mentioned under point (v) and detailed in the sections 6.2 and 7.2. Since ASI has the finest resolution of the currently available passive microwave sea-ice concentration algorithms, showing that our merged dataset is better than ASI in terms of an open-water extent which is closer to the reference data immanently shows that it is also better than other, even more coarsely resolved passive microwave sea-ice concentration algorithms.

The advantage of the thermal infrared data over the passive microwave data is their finer spatial resolution, but the disadvantages are the limitation to cloud-free scenes, the so-induced dependence on the quality of the cloud mask and an enhanced sensitivity to sea-ice thickness which makes it hard to disentangle sea-ice concentration and sea-ice thickness. These points are overcome by the merging: We do not only fill the cloud gaps, but also ensure spatial continuity by tuning the merged product to preserve the mean of the ASI passive microwave sea-ice concentration. Furthermore, we mitigate the influence of unscreened clouds. The sensitivity towards sea-ice thickness arises from the design of the algorithm which assumes only water and one sea-ice thickness class within the region which is used for the ice tie-point retrieval.

8. Summary & Conclusions

If there are two ice thickness classes and the thinner class is thin enough to be influenced by the oceanic heat flux from the ocean-ice interface, it will show up as reduced sea-ice concentration, even if the actual sea-ice concentration is 100%. This is desired by Drüe and Heinemann (2005), the authors upon whose work we build, as they aim to represent the thermal forcing of the atmosphere, but problematic for us because we want to retrieve the actual ice fraction. Therefore, we tune the merged dataset to preserve the mean of the ASI sea-ice concentration. Our merged product is thus superior to the MODIS sea-ice concentration product alone in that it is spatially continuous and spatially consistent with the ASI sea-ice concentration on a scale of 5 km by 5 km.

Another approach to retrieve the sea-ice concentration from thermal infrared data would be to use a lead product (e. g., Willmes and Heinemann (2016)) and use the inverse of the lead-area fraction as sea-ice concentration. One advantage over the MODIS sea-ice concentration algorithm which we use would be that the thinner ice class of the example above would show up as 100% sea-ice concentration. However, since the lead product is a binary product on a scale of 1 km, we would need to average over a larger spatial scale to obtain a lead-area fraction product which we could invert to obtain sea-ice concentration, which would mean that we lose the main advantage of the finer spatial resolution. Lead products can, however, be used for qualitative comparison to evaluate the potential of the merged dataset for lead retrieval.

Lastly, lead-area fraction can be retrieved from SAR data. Owing to its fine resolution of 40 m by 40 m (for the data used in this study), enough binary lead/no lead pixels are present on a scale of 1 km by 1 km to use the inverse of the lead-area fraction as sea-ice concentration, as we do in section 7.2. The advantage of the SAR data is that leads are clearly identifiable as 0% sea-ice concentration. However, the product used here was trained using small leads with a flat surface (Murashkin et al., 2018), so that larger open-water areas with a rough surface are classified as ice. This makes it hard to use this product operationally as a sea-ice concentration dataset for the merging, but it is well-suited for an intercomparison study as we do in section 7.2.

(vii) Derive uncertainty estimates for the merged and MODIS sea-ice concentration

The MODIS sea-ice concentration uncertainties are derived by Gaussian error propagation based on the ice and water tie-point uncertainties. The ice tie-point uncertainty is the standard deviation of the 48 iterations described under (i), the water tie-point uncertainty is the measurement uncertainty of 1.3 K. The MODIS sea-ice concentration uncertainty increases towards summer, driven by increasing surface temperatures which decrease the dynamic range (difference between ice and water

tie-point). The large uncertainties in May motivate us to derive an ice tie-point threshold above which meaningful sea-ice concentration cannot be retrieved. Choosing a low threshold would ensure that the uncertainties are small at the expense of discarding many pixels. Choosing a high threshold, on the other hand, would enable us to keep many pixels at the expense of accepting pixels with larger uncertainties. The threshold is thus a compromise between discarding as few pixels as possible and at the same time reducing the uncertainty as far as possible. We select a threshold of 266.5 K.

Having derived MODIS sea-ice concentration uncertainty estimates, we next present uncertainty estimates for the merged sea-ice concentration. To this end, we assume that the ASI sea-ice concentration uncertainties are a function of the sea-ice concentration according to Spreen et al. (2008). Gaussian error propagation based on the MODIS and ASI sea-ice concentration uncertainties then yields the merged sea-ice concentration uncertainty. A time series of the uncertainties shows that the evolution of the merged and MODIS sea-ice concentration uncertainty is mostly synchronous and between 5 % and 15 % until mid April, when the MODIS sea-ice concentration uncertainty gets larger than the merged sea-ice concentration uncertainty. In May, the average merged sea-ice concentration uncertainty is 18 %, while the average MODIS sea-ice concentration uncertainty is 25 %. The ASI sea-ice concentration is constantly between 6 % and 8 % throughout the entire period, which is mostly due to our selection of scenes with high sea-ice concentration and the much simpler uncertainty assumption for the ASI sea-ice concentration. Last, we compare our uncertainties to the differences between the merged, MODIS and ASI sea-ice concentration and the Sentinel-2 reference sea-ice concentration (classifying thin ice as ice). We find that in most cases (approximately 80 %) our uncertainties are higher than the differences. We conclude that our uncertainties are a conservative estimate of the actual uncertainty.

(viii) Apply the merged sea-ice concentration dataset for monitoring the February 2018 North Greenland polynya

In this part of the thesis, we use the merged sea-ice concentration dataset to monitor a polynya which formed north of Greenland in the second half of February 2018 and lasted until March 8.

The mean MODIS sea-ice concentration in the polynya region (see Fig. 7.4) is 95 % before the polynya opens, goes down to 75 % at the maximal extent and increases to 95 %, where it levels off. The merged sea-ice concentration starts at 100 %, goes down to 60 % and then increases to 100 % again. Note that the area which we defined as polynya region also comprises areas which were close to 100 % throughout the polynya event, which explains the comparably high mean sea-ice concentration

8. Summary & Conclusions

even at the maximal extent of the polynya.

The explanation for the MODIS sea-ice concentration being smaller than the merged sea-ice concentration during the opening and refreezing of the polynya is the sensitivity of the MODIS sea-ice concentration to the ice thickness distribution: If there is more than one ice thickness class within the region used for the tie-point retrieval, the thinner ice will be retrieved as reduced sea-ice concentration, as described under point (vi). The merged sea-ice concentration is less sensitive to the ice thickness because it is tuned to preserve the mean of the ASI sea-ice concentration. This effect is predominant during the opening and the refreezing/closing of the polynya, therefore the MODIS sea-ice concentration is lower.

While the polynya is open, the freshly forming frazil and grease ice within the polynya is retrieved as sea-ice concentration of approximately 40 % by the MODIS sea-ice concentration. The high ice-surface temperatures caused by the oceanic heat flux in the absence of a closed ice cover and by the high air temperatures cause high ice tie-points, making the MODIS sea-ice concentration susceptible to small temperature variations. The combination of these effects causes the comparably high MODIS sea-ice concentration even when there is open water, while the ASI sea-ice concentration goes down to 0 %.

As in the intercomparison study, we use the open-water extent as metric to show the advantages of the finer resolution of the merged sea-ice concentration over the ASI sea-ice concentration with the coarser resolution. It is normalised by the number of cloud-free pixels for a consistent day-to-day comparison. The open-water extent of the merged sea-ice concentration is up to 60 % higher relative to the ASI open-water extent during the early opening phase. This shows the benefit of the finer resolution of the merged product which allows a finer resolution of leads and thus a larger open-water extent. As the polynya opens, it gets higher than the ASI open-water extent in absolute terms, but the relative difference decreases.

(ix) Investigate evolution, drivers and consequences of the February 2018 North Greenland polynya

After the initial opening, the open-water area expanded over 12 days, reached its maximal extent of more than 60,000 km² on February 26th and decreased linearly until it closed on March 8th. The closing was due to fast refreezing after the warm-air intrusion abated. Additionally, there was dynamic closing by southward sea-ice drift. The merged sea-ice concentration shows closed sea-ice cover after March 8th. Nonetheless, the area of freshly grown sea ice is still distinguishable in SAR images on March 31st.

The evolution of the polynya in February is driven by the sea-ice drift. The sea-ice drift was directed northwards instead of the usually dominating southward direction

during the polynya opening. Furthermore, it was 50% stronger than usual. The sea-ice drift was weak during the first half of March, allowing for undisturbed thermodynamic growth of new sea ice. Two convergent events at the end of February and mid March brought back sea ice which was exported from the polynya area during the formation. Therefore, there is a mixture of flat, thermodynamically grown sea ice and rough sea ice grown due to sea-ice dynamics at the end of March. We derive a sea-ice volume of 33 km^3 which has been produced in the polynya. This is small compared to other Arctic polynyas, but considerable given that the polynya was only open for a comparably short time and that sea-ice production in this region is normally negligible.

Temperatures during the opening of the polynya were more than 20° C above average. This was caused partly by a high-pressure system above the Kara Sea which brought in warm air from the Atlantic. However, the air temperatures still remained below freezing. They were not high enough to melt the sea ice, but slowed down the refreezing process. Only locally, the daily maximum air temperature exceeded the freezing point several times, but not long and strong enough to cause substantial melting. The polynya also contributed to this air temperature anomaly due to the heat released from the ocean to the atmosphere.

In summary, this thesis introduces a new sea-ice concentration dataset from merged thermal infrared and passive microwave satellite data. It is superior to the MODIS sea-ice concentration alone in that it is spatially continuous, i. e., without cloud gaps, and less sensitive towards the influence of thin ice. At the same time, it outperforms the ASI sea-ice concentration due to its unprecedentedly fine spatial resolution of 1 km. This makes it possible to retrieve leads which are not resolved or smeared out by the ASI sea-ice concentration. By tuning the merged sea-ice concentration to preserve the mean of the ASI, we ensure that the sea-ice concentration field is spatially continuous if MODIS data are not available.

Coming back to the title of the thesis, we conclude that merging MODIS and ASI sea-ice concentration data indeed creates a dataset which is „more than the sum of its parts“ since it outperforms ASI sea-ice concentration due to its finer resolution and is superior to MODIS sea-ice concentration in that it is spatially continuous and less susceptible to ice thickness.

9. Outlook

The retrieval of meaningful MODIS thermal infrared data is limited to winter and spring conditions since the small temperature contrast between the ice and water surface in summer limits their usability. At this time of year, visible channels, e.g. by MODIS, can provide similar fine-resolution data which can be used for sea-ice concentration retrieval to extend the merged product to a year-round dataset. The MODIS thermal infrared sea-ice concentration algorithm should also be applicable to visible data. First tests showed promising results.

Care has to be taken concerning the surface melt, which makes ASI data in summer underestimate the sea-ice concentration. Tuning the merged product to preserve the mean of the ASI sea-ice concentration would thus mean that this underestimation propagates into the merged sea-ice concentration. This could be mitigated by including melt-pond data as presented by Rösel et al. (2012) or Istomina et al. (2015b,a) in the product. Using atmospherically corrected ASI sea-ice concentration data as proposed by Lu et al. (2018) would further improve the product's accuracy. Especially since most of the ship traffic is in summer, a fine-resolution, spatially continuous sea-ice concentration product in which the influence of surface melt and the atmospheric contribution on the ASI data is mitigated would be a valuable product.

The MODIS instruments aboard Aqua and Terra have exceeded their design lifespans and successor missions like NASA's Visible Infrared Imaging Radiometer Suite (VIIRS) (since 2011) aboard the Suomi National Polar-orbiting Partnership (Suomi NPP) satellite or the Sea and Land Surface Temperature Radiometer (SLSTR) and Ocean and Land Colour Instrument (OLCI) on European Space Agency (ESA)'s Sentinel-3A (since 2016) and Sentinel-3B (since 2018) satellites are already operational. Visible and thermal infrared data from these instruments can replace the MODIS data once it ceases operation. Possible follow-ups for the AMSR2 passive microwave radiometer are AMSR3 or the Copernicus Imaging Microwave Radiometer (CIMR), whose launches are scheduled for 2023 and 2028, respectively. Calculating the merged sea-ice concentration from these measurements and calibrating the time series at the transition between sensors would enable the operational production of a consistent long-term time series of sea-ice concentration at 1 km resolution, which could be extended backwards until 2002 by including AMSR-E data. Using the 85 GHz frequency channel of the SSM/I and SSMIS microwave radiometers and thermal infrared data of AVHRR, the time series could even be extended backwards to 1987. Such a time series would allow to study the long-term evolution of the Arctic sea-ice cover at

an unprecedentedly fine resolution under a climatological perspective.

A. Appendix

Natural constants

Table A.1.: Natural constants used in this thesis

Quantity	Symbol	Value	Unit
Planck's constant	h	6.63×10^{-34}	Js
Boltzmann's constant	k	1.38×10^{-23}	JK^{-1}
Velocity of light	c	3×10^8	ms^{-1}
Stefan-Boltzmann constant	σ	5.637×10^{-8}	$Wm^{-2}K^{-4}sr^{-1}$

Acronyms

AEM Airborne Electromagnetic

AMSR-E Advanced Microwave Scanning Radiometer for Earth Observation

AMSR2 Advanced Microwave Scanning Radiometer 2

ASCAT Advanced Scatterometer

ASI Arctic Radiation and Turbulence Study Sea Ice

ATBD Algorithm Theoretical Basis Document

AVHRR Advanced Very High Resolution Radiometer

CET Central European Time

CFSv2 Climate Forecast System version 2

CIMR Copernicus Imaging Microwave Radiometer

CMEMS Copernicus Marine Environment Monitoring Service

EASE Equal-Area Scalable Earth

ECICE Environment Canada's Ice Concentration Extractor

ECMWF European Centre for Medium-Range Weather Forecasts

ERA5 European Centre for Medium-Range Weather Forecasts Reanalysis 5th Generation

ESA European Space Agency

EUMETSAT European Organisation for the Exploitation of Meteorological Satellites

EU European Union

GCOM-W1 Global Change Observation Mission–Water 1

GSFC Goddard Space Flight Center

HDF4 Hierarchical Data Format 4

HTTPS Hypertext Transfer Protocol Secure

JAXA Japan Aerospace Exploration Agency

MODIS Moderate Resolution Imaging Spectroradiometer

MOSAIC Multidisciplinary drifting Observatory for the Study of Arctic Climate

NAOSIM North Atlantic Arctic Ocean Sea Ice Model

NASA National Aeronautics and Space Administration

NCEP-CFSR Climate Forecast System Reanalysis

NCEP National Center for Environmental Prediction

NSIDC National Snow and Ice Data Center

NetCDF4 Network Common Data Form 4

OLCI Ocean and Land Colour Instrument

OSI SAF Ocean and Sea Ice Satellite Application Facility

PIOMAS Pan-Arctic Ice Ocean Modeling and Assimilation System

RMSD root mean square deviation

SAR Synthetic Aperture Radar

SIC sea-ice concentration

SLSTR Sea and Land Surface Temperature Radiometer

A. Appendix

SMAP Soil Moisture Active Passive

SMMR Scanning Multi-channel Microwave Radiometer

SMOS Soil Moisture and Ocean Salinity

SSM/I Special Sensor Microwave Imager

SSMIS Special Sensor Microwave Imager/Sounder

Suomi NPP Suomi National Polar-orbiting Partnership

VIIRS Visible Infrared Imaging Radiometer Suite

XML Extensible Markup Language

Bibliography

- Ackerman, S., Frey, R., Strabala, K., Liu, Y., Gumley, L., Baum, B., and Paul, M. (2010). Discriminating clear-sky from cloud with MODIS. Technical report.
- Ackerman, S. A., Strabala, K. I., Menzel, W. P., Frey, R. A., Moeller, C. C., and Gumley, L. E. (1998). Discriminating clear sky from clouds with MODIS. *Journal of Geophysical Research Atmospheres*, 103(D24):32141–32157.
- Alfred-Wegener-Institute (2020). MOSAiC expedition website. <https://mosaic-expedition.org/>, last access 19 November 2020.
- Andersen, S., Tonboe, R., Kern, S., and Schyberg, H. (2006). Improved retrieval of sea ice total concentration from spaceborne passive microwave observations using numerical weather prediction model fields: An intercomparison of nine algorithms. *Remote Sensing of Environment*, 104(4):374–392.
- Assmy, P., Fernández-Méndez, M., Duarte, P., Meyer, A., Randelhoff, A., Mundy, C. J., Olsen, L. M., Kauko, H. M., Bailey, A., Chierici, M., Cohen, L., Doulgeris, A. P., Ehn, J. K., Fransson, A., Gerland, S., Hop, H., Hudson, S. R., Hughes, N., Itkin, P., Johnsen, G., King, J. A., Koch, B. P., Koenig, Z., Kwasniewski, S., Laney, S. R., Nicolaus, M., Pavlov, A. K., Polashenski, C. M., Provost, C., Rösel, A., Sandbu, M., Spreen, G., Smedsrud, L. H., Sundfjord, A., Taskjelle, T., Tatarek, A., Wiktor, J., Wagner, P. M., Wold, A., Steen, H., and Granskog, M. A. (2017). Leads in Arctic pack ice enable early phytoplankton blooms below snow-covered sea ice. *Scientific Reports*, 7:40850.
- Beitsch, A., Kaleschke, L., and Kern, S. (2014). Investigating high-resolution AMSR2 sea ice concentrations during the February 2013 fracture event in the Beaufort Sea. *Remote Sensing*, 6(5):3841–3856.
- Boisvert, L. N. and Stroeve, J. C. (2015). The Arctic is becoming warmer and wetter as revealed by the Atmospheric Infrared Sounder. *Geophysical Research Letters*, 42(11):4439–4446.
- Campana, S. E., Casselman, J. M., Jones, C. M., Black, G., Barker, O., Evans, M., Guzzo, M. M., Kilada, R., Muir, A. M., and Perry, R. (2020). Arctic freshwater fish productivity and colonization increase with climate warming. *Nature Climate Change*, 10(5):428–433.

- Cavalieri, D. J., Gloersen, P., and Campbell, W. J. (1984). Determination of sea ice parameters with the Nimbus 7 SMMR. *Journal of Geophysical Research*, 89(D4):5355–5369.
- Cavalieri, D. J., Gloersen, P., Parkinson, C. L., Comiso, J. C., and Zwally, H. J. (1997). Observed Hemispheric Asymmetry in Global Sea Ice Changes. *Science*, 278(5340):1104–1106.
- Cavalieri, D. J., Parkinson, C. L., Gloersen, P., and Zwally, H. J. (1996). *Sea Ice Concentrations from Nimbus-7 SMMR and DMSP SSM/I-SSMIS Passive Microwave Data, Version 1*. [1979-2014]. Boulder, Colorado USA. NASA National Snow and Ice Data Center Distributed Active Archive Center. <https://nsidc.org/data/nsidc-0051>, last access November 19, 2020.
- Chen, J., Kang, S., Chen, C., You, Q., Du, W., Xu, M., Zhong, X., Zhang, W., and Chen, J. (2020). Changes in sea ice and future accessibility along the Arctic Northeast Passage. *Global and Planetary Change*, page 103319.
- Cohen, J., Screen, J. A., Furtado, J. C., Barlow, M., Whittleston, D., Coumou, D., Francis, J., Dethloff, K., Entekhabi, D., Overland, J., and Jones, J. (2014). Recent Arctic amplification and extreme mid-latitude weather. *Nature Geoscience*, 7(9):627–637.
- Cohen, J., Zhang, X., Francis, J., Jung, T., Kwok, R., Overland, J., Ballinger, T., Bhatt, U., Chen, H., Coumou, D., et al. (2019). Divergent consensus on Arctic amplification influence on midlatitude severe winter weather. *Nature Climate Change*, pages 1–10.
- Comiso, J. C. (1986). Characteristics of Arctic winter sea ice from satellite multispectral microwave observations. *Journal of Geophysical Research*, 91(C1):975–994.
- Comiso, J. C. (1995). SSM/I Sea Ice Concentrations Using the Bootstrap Algorithm. Technical Report 1380, NASA, Goddard Space Flight Center, Greenbelt, Maryland 20771, US.
- Comiso, J. C., Cavalieri, D. J., Parkinson, C. L., and Gloersen, P. (1997). Passive microwave algorithms for sea ice concentration: A comparison of two techniques. *Remote Sensing of Environment*, 60(3):357–384.
- Coumou, D., Di Capua, G., Vavrus, S., Wang, L., and Wang, S. (2018). The influence of Arctic amplification on mid-latitude summer circulation. *Nature Communications*, 9(1).
- Dai, A., Luo, D., Song, M., and Liu, J. (2019). Arctic amplification is caused by sea-ice loss under increasing CO₂. *Nature Communications*, 10(1):121.

- Danielson, S., Ahkinga, O., Ashjian, C., Basyuk, E., Cooper, L., Eisner, L., Farley, E., Iken, K., Grebmeier, J., Juranek, L., et al. (2020). Manifestation and consequences of warming and altered heat fluxes over the Bering and Chukchi Sea continental shelves. *Deep Sea Research Part II: Topical Studies in Oceanography*, page 104781.
- Dee, D. P., Uppala, S. M., Simmons, A. J., Berrisford, P., Poli, P., Kobayashi, S., Andrae, U., Balmaseda, M. A., Balsamo, G., Bauer, P., Bechtold, P., Beljaars, A. C. M., van de Berg, L., Bidlot, J., Bormann, N., Delsol, C., Dragani, R., Fuentes, M., Geer, A. J., Haimberger, L., Healy, S. B., Hersbach, H., Hólm, E. V., Isaksen, L., Kållberg, P., Köhler, M., Matricardi, M., McNally, A. P., Monge-Sanz, B. M., Morcrette, J.-J., Park, B.-K., Peubey, C., de Rosnay, P., Tavolato, C., Thépaut, J.-N., and Vitart, F. (2011). The ERA-Interim reanalysis: configuration and performance of the data assimilation system. *Quarterly Journal of the Royal Meteorological Society*, 137(656):553–597.
- Drüe, C. and Heinemann, G. (2004). High-resolution maps of the sea-ice concentration from MODIS satellite data. *Geophysical Research Letters*, 31(20):L20403.
- Drüe, C. and Heinemann, G. (2005). Accuracy assessment of sea-ice concentrations from MODIS using in-situ measurements. *Remote Sensing of Environment*, 95(2):139–149.
- Eastman, R. and Warren, S. G. (2010). Interannual Variations of Arctic Cloud Types in Relation to Sea Ice. *Journal of Climate*, 23(15):4216–4232.
- ECMWF Copernicus Climate Change Service (2020). ERA5 documentation. <https://confluence.ecmwf.int/display/CKB/ERA5+data+documentation>, last access November 19, 2020.
- ESA (2020). Download of Sentinel data. <https://scihub.copernicus.eu/> last access November 19, 2020.
- Farrelly, B., Johannessen, J. A., Johannessen, O. M., Svendsen, E., Kloster, K., Horjen, I., Mätzler, C., Campbell, W. J., Crawford, J., Harrington, R., Jones, L., Swift, C., Delnore, V. E., Cavalieri, D., Gloersen, P., Hsiao, S. V., Shemdin, O. H., Thompson, T. W., Ramseier, R. O., Johannessen, O. M., and Campbell, W. J. (1983). Norwegian remote sensing experiment in a marginal ice zone. *Science*, 220(4599):781–787.
- Gao, Y., Xie, H., Lu, N., Yao, T., and Liang, T. (2010). Toward advanced daily cloud-free snow cover and snow water equivalent products from Terra-Aqua MODIS and Aqua AMSR-E measurements. *Journal of Hydrology*, 385(1):23 – 35.
- Graham, R. M., Cohen, L., Petty, A. A., Boisvert, L. N., Rinke, A., Hudson, S. R., Nicolaus, M., and Granskog, M. A. (2017). Increasing frequency and duration of Arctic winter warming events. *Geophysical Research Letters*, 44(13):6974–6983.

- GSFC (2020a). MODIS cloud mask homepage. <https://modis.gsfc.nasa.gov/data/dataproduct/mod35.php>, last access November 19, 2020.
- GSFC (2020b). MODIS instrument homepage. <https://modis.gsfc.nasa.gov/>, last access November 19, 2020.
- GSFC (2020c). MODIS Snow and Ice product ATBD. https://modis.gsfc.nasa.gov/data/atbd/atbd_mod10.pdf last access November 19, 2020.
- Haas, C., Hendricks, S., Eicken, H., and Herber, A. (2010). Synoptic airborne thickness surveys reveal state of Arctic sea ice cover. *Geophysical Research Letters*, 37(9).
- Haas, C. and Jochmann, P. (2003). Continuous EM and ULS thickness profiling in support of ice force measurements. In *Loeset, S., Bonnemaire, B., Bjerkas, M. (Eds.), Proceedings of the 17th International Conference on Port and Ocean Engineering under Arctic Conditions, POAC 2003, Trondheim, Norway. Department of Civil and Transport Engineering, Norwegian University of Sci*, volume 2, pages 849–856.
- Haas, C., Lobach, J., Hendricks, S., Rabenstein, L., and Pfaffling, A. (2009). Helicopter-borne measurements of sea ice thickness, using a small and lightweight, digital EM system. *Journal of Applied Geophysics*, 67(3):234 – 241. Airborne Geophysics.
- Hall, D. K., Key, J. R., Casey, K. A., Riggs, G. A., and Cavalieri, D. J. (2004). Sea ice surface temperature product from MODIS. *IEEE Transactions on Geoscience and Remote Sensing*, 42(5):1076–1087.
- Hall, D. K. and Riggs, G. A. (2015). MODIS/Terra Sea Ice Extent 5-Min L2 Swath 1km, Version 6. [Apr 2015].
- Heygster, G., Huntemann, M., Ivanova, N., Saldo, R., and Pedersen, L. T. (2014). Response of passive microwave sea ice concentration algorithms to thin ice. In *International Geoscience and Remote Sensing Symposium (IGARSS)*, pages 3618–3621. IEEE.
- Huntemann, M., Heygster, G., Kaleschke, L., Krumpen, T., Mäkynen, M., and Drusch, M. (2014). Empirical sea ice thickness retrieval during the freeze-up period from SMOS high incident angle observations. *The Cryosphere*, 8(2):439–451.
- Istomina, L., Heygster, G., Huntemann, M., Marks, H., Melsheimer, C., Zege, E., Malinka, A., Prikhach, A., and Katsev, I. (2015a). Melt pond fraction and spectral sea ice albedo retrieval from MERIS data - Part 2: Case studies and trends of sea ice albedo and melt ponds in the Arctic for years 2002-2011. *Cryosphere*, 9(4):1567–1578.
- Istomina, L., Heygster, G., Huntemann, M., Schwarz, P., Birnbaum, G., Scharien, R., Polashenski, C., Perovich, D., Zege, E., Malinka, A., Prikhach, A., and Katsev, I. (2015b). Melt pond fraction and spectral sea ice albedo retrieval from MERIS data -

- Part 1: Validation against in situ, aerial, and ship cruise data. *Cryosphere*, 9(4):1551–1566.
- Ivanova, N., Johannessen, O. M., Pedersen, L. T., and Tonboe, R. T. (2014). Retrieval of arctic sea ice parameters by satellite passive microwave sensors: A comparison of eleven sea ice concentration algorithms. *IEEE Transactions on Geoscience and Remote Sensing*, 52(11):7233–7246.
- Ivanova, N., Pedersen, L. T., Tonboe, R. T., Kern, S., Heygster, G., Lavergne, T., Sørensen, A., Saldo, R., Dybkjær, G., Brucker, L., and Shokr, M. (2015). Inter-comparison and evaluation of sea ice algorithms: Towards further identification of challenges and optimal approach using passive microwave observations. *Cryosphere*, 9(5):1797–1817.
- JAXA (2020). AMSR2 homepage. https://suzaku.eorc.jaxa.jp/GCOM_W/w_amsr2/whats_amsr2.html, last access November 19, 2020.
- Jin, D., Chung, S.-R., Lee, K.-S., Seo, M., Choi, S., Seong, N.-H., Jung, D., Sim, S., Kim, J., and Han, K.-S. (2020). Development of Geo-KOMPSAT-2A Algorithm for Sea-Ice Detection Using Himawari-8/AHI Data. *Remote Sensing*, 12(14):2262.
- Kaleschke, L., Lüpkes, C., Vihma, T., Haarpaintner, J., Bochert, A., Hartmann, J., and Heygster, G. (2001). SSM/I Sea Ice Remote Sensing for Mesoscale Ocean-Atmosphere Interaction Analysis. *Canadian Journal of Remote Sensing*, 27(5):526–537.
- Kauker, F., Gerdes, R., Karcher, M., Köberle, C., and Lieser, J. (2003). Variability of Arctic and North Atlantic sea ice: A combined analysis of model results and observations from 1978 to 2001. *Journal of Geophysical Research Oceans*, 108(C6):3182.
- Kern, S., Lavergne, T., Notz, D., Pedersen, L. T., and Tonboe, R. (2020). Satellite passive microwave sea-ice concentration data set inter-comparison for arctic summer conditions. *The Cryosphere*, 14(7):2469–2493.
- Kern, S., Lavergne, T., Notz, D., Pedersen, L. T., Tonboe, R. T., Saldo, R., and Sørensen, A. M. (2019). Satellite passive microwave sea-ice concentration data set intercomparison: closed ice and ship-based observations. *The Cryosphere*, 13(12):3261–3307.
- Kovacs, K. M., Lydersen, C., Overland, J. E., and Moore, S. E. (2011). Impacts of changing sea-ice conditions on Arctic marine mammals. *Marine Biodiversity*, 41(1):181–194.
- Kwok, R., Spreen, G., and Pang, S. (2013). Arctic sea ice circulation and drift speed: Decadal trends and ocean currents. *Journal of Geophysical Research: Oceans*, 118(5):2408–2425.

- LAADS (2020a). MODIS cloud mask download. https://ladsweb.modaps.eosdis.nasa.gov/archive/allData/61/MYD35_L2/, last access November 19, 2020.
- LAADS (2020b). MODIS geolocation download. <https://ladsweb.modaps.eosdis.nasa.gov/archive/allData/61/MYD03/>, last access November 19, 2020.
- Lainema, M. and Nurminen, J. (2009). *A history of Arctic exploration : discovery, adventure and endurance at the top of the world*. Conway, London. 349 S. ; 35 cm : Ill., Kt.
- Lam, H. M., Spreen, G., Heygster, G., Melsheimer, C., and Young, N. W. (2018). Erroneous sea-ice concentration retrieval in the East Antarctic. *Annals of Glaciology*, 59(76pt2):201212.
- Lavergne, T., Eastwood, S., Teffah, Z., Schyberg, H., and Breivik, L.-A. (2010). Sea ice motion from low-resolution satellite sensors: An alternative method and its validation in the Arctic. *Journal of Geophysical Research: Oceans*, 115(C10).
- Lavergne, T., Macdonald Sørensen, A., Kern, S., Tonboe, R., Notz, D., Aaboe, S., Bell, L., Dybkjær, G., Eastwood, S., Gabarro, C., Heygster, G., Anne Killie, M., Brandt Kreiner, M., Lavelle, J., Saldo, R., Sandven, S., and Pedersen, L. T. (2019). Version 2 of the EUMETSAT OSI SAF and ESA CCI sea-ice concentration climate data records. *Cryosphere*, 13(1):49–78.
- Lebedev, V. (1938). Rost l'da v arkticheskikh rekakh i moriakh v zavisimosti ot otritsatel'nykh temperatur vozdukha. *Problemy arktiki*, 5-6:9–25.
- Li, Z., Zhao, J., Su, J., Li, C., Cheng, B., Hui, F., Yang, Q., and Shi, L. (2020). Spatial and Temporal Variations in the Extent and Thickness of Arctic Landfast Ice. *Remote Sensing*, 12(1):64.
- Lindsay, R. and Rothrock, D. (1994). Arctic sea ice albedo from AVHRR. *Journal of Climate*, 7(11):1737–1749.
- Lindsay, R. W. and Rothrock, D. A. (1995). Arctic sea ice leads from advanced very high resolution radiometer images. *Journal of Geophysical Research*, 100(C3):4533–4544.
- Lu, J., Heygster, G., and Spreen, G. (2018). Atmospheric Correction of Sea Ice Concentration Retrieval for 89 GHz AMSR-E Observations. *IEEE Journal of Selected Topics in Applied Earth Observations and Remote Sensing*, PP:1–16.
- Ludwig, V. and Spreen, G. (2018). Sea-ice concentration observed by different remote sensing methods. https://figshare.com/articles/figure/Sea_ice_concentration_observed_by_different_remote_sensing_methods/6275807, last access November 19, 2020.

- Ludwig, V., Spreen, G., Haas, C., Istomina, L., Kauker, F., and Murashkin, D. (2019). The 2018 North Greenland polynya observed by a newly introduced merged optical and passive microwave sea-ice concentration dataset. *The Cryosphere*, 13(7):2051–2073.
- Ludwig, V., Spreen, G., and Pedersen, L. T. (2020). Evaluation of a new merged sea-ice concentration dataset at 1 km resolution from thermal infrared and passive microwave satellite data in the arctic. *Remote Sensing*, 12(19):3183.
- Marcq, S. and Weiss, J. (2012). Influence of sea ice lead-width distribution on turbulent heat transfer between the ocean and the atmosphere. *The Cryosphere*, 6(1):143–156.
- Maslanik, J. and Stroeve, J. (1999). *Near-Real-Time DMSP SSMIS Daily Polar Gridded Sea Ice Concentrations, Version 1*. [2015-2020]. Boulder, Colorado USA. NASA National Snow and Ice Data Center Distributed Active Archive Center. <https://nsidc.org/data/nsidc-0051>, last access November 19, 2020.
- Masuoka, E., Fleig, A., Wolfe, R. E., and Patt, F. (1998). Key characteristics of MODIS data products. *IEEE Transactions on Geoscience and Remote Sensing*, 36(4):1313–1323.
- Melia, N., Haines, K., and Hawkins, E. (2016). Sea ice decline and 21st century trans-Arctic shipping routes. *Geophysical Research Letters*, 43(18):9720–9728.
- Mewes, D. and Jacobi, C. (2018). Heat Transport Pathways into the Arctic and their Connections to Surface Air Temperatures. *Atmospheric Chemistry and Physics Discussions*, 2018:1–14.
- Millero, F. and Leung, W. (1976). Thermodynamics of seawater at one atmosphere. *American Journal of Science*, 276(9):1035–1077.
- Moore, G. W. (2016). The December 2015 North Pole Warming Event and the Increasing Occurrence of Such Events. *Scientific Reports*, 6.
- Moore, G. W. K., Schweiger, A., Zhang, J., and Steele, M. (2018). What Caused the Remarkable February 2018 North Greenland Polynya? *Geophysical Research Letters*, 0(0).
- Morales-Maqueda, M. A., Willmott, A. J., and Biggs, N. R. T. (2004). Polynya Dynamics: a Review of Observations and Modeling. *Reviews of Geophysics*, 42(1).
- Murashkin, D., Spreen, G., Huntemann, M., and Dierking, W. (2018). Method for detection of leads from Sentinel-1 SAR images. *Annals of Glaciology*, page 113.
- Nansen, F. (1902). Oceanography of the North Polar Basin. In *Scientific Results*, volume 3, page 427. Christiania : J. Dybwad; London, New York, Bombay: Longmans, Green, and Co.; Leipzig: F. A. Brockhaus.

- NASA (2020). A-Train homepage. <https://atrain.nasa.gov/>, last access November 19, 2020.
- Notz, D. and Worster, M. G. (2009). Desalination processes of sea ice revisited. *Journal of Geophysical Research: Oceans*, 114(5):C05006.
- NSIDC (2020a). MODIS ice-surface temperature download. <https://n5eil01u.ecs.nsidc.org/MOSA/MYD29.006/> last access November 19, 2020.
- NSIDC (2020b). MODIS ice-surface temperature homepage. <https://nsidc.org/data/MYD29> last access November 19, 2020.
- NSIDC (2020c). NASA Team SIC. <https://nsidc.org/data/nsidc-0051> last access November 19, 2020.
- NSIDC (2020d). NSIDC grid. https://nsidc.org/data/polar-stereo/ps_grids.html, last access November 19, 2020.
- Onstott, R. G., Grenfell, T. C., Matzler, C., Luther, C. A., and Svendsen, E. A. (1987). Evolution of microwave sea ice signatures during early summer and midsummer in the marginal ice zone. *Journal of Geophysical Research*, 92(C7):6825–6835.
- OSI SAF (2020a). Global Sea Ice Concentration Climate Data Record Product User Manual. http://osisaf.met.no/docs/osisaf_cdop3_ss2_pum_sea-ice-conc-climate-data-record_v2p0.pdf.
- OSI SAF (2020b). OSI-405 low-resolution sea-ice drift product. http://osisaf.met.no/p/ice/lr_ice_drift.html, last access November 19, 2020.
- OSI SAF (2020c). OSI-430 sea-ice concentration product. http://osisaf.met.no/p/ice/ice_conc_cdr_v2.html, last access November 19, 2020.
- OSI SAF (2020d). OSI-450 sea-ice concentration climatology. <http://osisaf.met.no/p/ice/>, last access November 19, 2020.
- Patilea, C., Heygster, G., Huntemann, M., and Spreen, G. (2019). Combined SMAP-SMOS thin sea ice thickness retrieval. *Cryosphere*, 13(2):675–691.
- Pongracz, J. D., Paetkau, D., Branigan, M., and Richardson, E. (2017). Recent Hybridization between a Polar Bear and Grizzly Bears in the Canadian Arctic. *Arctic*, 70(2):151–160.
- Preußer, A., Heinemann, G., Willmes, S., and Paul, S. (2016). Circumpolar polynya regions and ice production in the Arctic: results from MODIS thermal infrared imagery from 2002/2003 to 2014/2015 with a regional focus on the Laptev Sea. *The Cryosphere*, 10(6):3021–3042.

- Rösel, A., Kaleschke, L., and Birnbaum, G. (2012). Melt ponds on Arctic sea ice determined from MODIS satellite data using an artificial neural network. *Cryosphere*, 6(2):431–446.
- Rostosky, P., Spreen, G., Farrell, S. L., Frost, T., Heygster, G., and Melsheimer, C. (2018). Snow Depth Retrieval on Arctic Sea Ice From Passive Microwave Radiometers—Improvements and Extensions to Multiyear Ice Using Lower Frequencies. *Journal of Geophysical Research: Oceans*, 123(10):7120–7138.
- Saha, S., Moorthi, S., Pan, H. L., Wu, X., Wang, J., Nadiga, S., Tripp, P., Kistler, R., Woollen, J., Behringer, D., Liu, H., Stokes, D., Grumbine, R., Gayno, G., Wang, J., Hou, Y. T., Chuang, H. Y., Juang, H. M. H., Sela, J., Iredell, M., Treadon, R., Kleist, D., Van Delst, P., Keyser, D., Derber, J., Ek, M., Meng, J., Wei, H., Yang, R., Lord, S., Van Den Dool, H., Kumar, A., Wang, W., Long, C., Chelliah, M., Xue, Y., Huang, B., Schemm, J. K., Ebisuzaki, W., Lin, R., Xie, P., Chen, M., Zhou, S., Higgins, W., Zou, C. Z., Liu, Q., Chen, Y., Han, Y., Cucurull, L., Reynolds, R. W., Rutledge, G., and Goldberg, M. (2010). The NCEP climate forecast system reanalysis. *Bulletin of the American Meteorological Society*, 91(8):1015–1057.
- Saha, S., Moorthi, S., Wu, X., Wang, J., Nadiga, S., Tripp, P., Behringer, D., Hou, Y. T., Chuang, H. Y., Iredell, M., Ek, M., Meng, J., Yang, R., Mendez, M. P., Van Den Dool, H., Zhang, Q., Wang, W., Chen, M., and Becker, E. (2014). The NCEP climate forecast system version 2. *Journal of Climate*, 27(6):2185–2208.
- Schledermann, P. (1980). Polynyas and Prehistoric Settlement Patterns. *Arctic*, 33(2):292–302.
- Shokr, M. and Kaleschke, L. (2012). Impact of surface conditions on thin sea ice concentration estimate from passive microwave observations. *Remote Sensing of Environment*, 121:36–50.
- Shokr, M., Lambe, A., and Agnew, T. (2008). A new algorithm (ECICE) to estimate ice concentration from remote sensing observations: An application to 85-GHz passive microwave data. *IEEE Transactions on Geoscience and Remote Sensing*, 46(12):4104–4121.
- Shokr, M. and Sinha, N. (2015). *Sea Ice: Physics and Remote Sensing*, volume 209 of *Geophysical Monograph Series*. American Geophysical Union and John Wiley & Sons, Inc.
- Smith, W. H. and Wessel, P. (1990). Gridding with continuous curvature splines in tension. *Geophysics*, 55(3):293–305.
- Spreen, G., Kaleschke, L., and Heygster, G. (2008). Sea ice remote sensing using AMSR-E 89-GHz channels. *Journal of Geophysical Research: Oceans*, 113(2):1–14.

- Sumata, H., Kauker, F., Karcher, M., and Gerdes, R. (2019a). Covariance of optimal parameters of an arctic sea ice-ocean model. *Monthly Weather Review*, 147(7):2579–2602.
- Sumata, H., Kauker, F., Karcher, M., and Gerdes, R. (2019b). Simultaneous parameter optimization of an arctic sea-ice-ocean model by a genetic algorithm. *Monthly Weather Review*, under review.
- Tamura, T. and Ohshima, K. I. (2011). Mapping of sea ice production in the Arctic coastal polynyas. *Journal of Geophysical Research: Oceans*, 116(C7).
- Taylor, P. C., Boeke, R. C., Li, Y., and Thompson, W. J. (2019). Arctic cloud annual cycle biases in climate models. *Atmospheric Chemistry and Physics*, 19(13):8759–8782.
- Temimi, M., Romanov, P., Ghedira, H., Khanbilvardi, R., and Smith, K. (2011). Sea-ice monitoring over the caspian sea using geostationary satellite data. *International Journal of Remote Sensing*, 32(6):1575–1593.
- TU Denmark (2020). Download of Sentinel-1 mosaics. <http://www.seaice.dk> last access November 19, 2020.
- Ulaby, F. T., Long, D. G., Blackwell, W. J., Elachi, C., Fung, A. K., Ruf, C., Sarabandi, K., Zebker, H. A., and Van Zyl, J. (2014). *Microwave Radar and Radiometric Remote Sensing*, volume 4. University of Michigan Press Ann Arbor.
- University of Bremen (2020). Homepage providing AMSR2 SIC. <https://seaice.uni-bremen.de>, last access November 19 2020.
- Vaughan, D. G., Comiso, J. C., Allison, I., Carrasco, J., Kaser, G., Kwok, R., Mote, P., Murray, T., Paul, F., Ren, J., Rignot, E., Solomina, O., Steffen, K., and Zhang, T. (2013). Observations: Cryosphere. In Stocker, T. F., Qin, D., Plattner, G.-K., Tignor, M., Allen, S. K., Boschung, J., Nauels, A., Xia, Y., Bex, V., and Midgley, P. M., editors, *Climate Change 2013: The Physical Science Basis. Contribution of Working Group I to the Fifth Assessment Report of the Intergovernmental Panel on Climate Change (IPCC)*, chapter 4, pages 317–382. Cambridge University Press, Cambridge, United Kingdom and New York, NY, USA.
- Vavrus, S. J. (2018). The Influence of Arctic Amplification on Mid-latitude Weather and Climate. *Current Climate Change Reports*, 4(3):238–249.
- Vuorinen, I., Hänninen, J., Rajasilta, M., Laine, P., Eklund, J., Montesino-Pouzols, F., Corona, F., Junker, K., Meier, H., and Dippner, J. W. (2015). Scenario simulations of future salinity and ecological consequences in the Baltic Sea and adjacent North Sea areasimplications for environmental monitoring. *Ecological Indicators*, 50:196 – 205.

- Wiebe, H., Heygster, G., and Markus, T. (2009). Comparison of the ASI Ice Concentration Algorithm With Landsat.7 ETM+ and SAR Imagery. *IEEE Transactions on Geoscience and Remote Sensing*, 47(9):3008–3015.
- Wiedemeier, J. and Ludwig, V. (2017). An investigation of anomalies in the Artist Sea Ice concentration algorithm. Not peer-reviewed, <https://seaice.uni-bremen.de/proceedings-theses-reports/>.
- Willmes, S. and Heinemann, G. (2015). Pan-arctic lead detection from MODIS thermal infrared imagery. *Annals of Glaciology*, 56(69):29–37.
- Willmes, S. and Heinemann, G. (2016). Sea-ice wintertime lead frequencies and regional characteristics in the Arctic, 2003-2015. *Remote Sensing*, 8(1):4.
- Woods, C. and Caballero, R. (2016). The Role of Moist Intrusions in Winter Arctic Warming and Sea Ice Decline. *Journal of Climate*, 29(12):4473–4485.
- World Meteorological Organisation (1970). WMO sea-ice nomenclature: Terminology, codes and illustrated glossary. Technical report, Geneva: Secretariat of the World Meteorological Organization.
- Ye, Y., Heygster, G., and Shokr, M. (2016a). Improving Multiyear Ice Concentration Estimates with Reanalysis Air Temperatures. *IEEE Transactions on Geoscience and Remote Sensing*, 54(5):2602–2614.
- Ye, Y., Shokr, M., Heygster, G., and Spreen, G. (2016b). Improving Multiyear Sea Ice Concentration Estimates with Sea Ice Drift. *Remote Sensing*, 8(5):2602–2614.
- Yu, Y., Taylor, P. C., and Cai, M. (2019). Seasonal Variations of Arctic Low-Level Clouds and Its Linkage to Sea Ice Seasonal Variations. *Journal of Geophysical Research: Atmospheres*, 124(22):12206–12226.
- Zatsepin, A., Zavialov, P., Kremenetskiy, V., Poyarkov, S., and Soloviev, D. (2010). The upper desalinated layer in the Kara Sea. *Oceanology*, 50(5):657–667.
- Zhang, J., Thomas, D. R., Rothrock, D. A., Lindsay, R. W., Yu, Y., and Kwok, R. (2003). Assimilation of ice motion observations and comparisons with submarine ice thickness data. *Journal of Geophysical Research C: Oceans*, 108(6):1–1.

Acknowledgements

A long journey comes to an end and while naming all the inspiring people I met on the way would require a chapter of its own, I take pleasure in acknowledging those who were most prominently at my side these past years.

This thesis would be 141 pages shorter without the support and advice of my supervisor Dr. Gunnar Spreen. I do not remember how often I knocked on the door of office N3330, but I do remember that I was not turned down a single time, and always left with more than I brought. Thanks, Gunnar, for accompanying me from day 1 to day 1693, for making me feel that you believe in me without needing to say so, and for enabling me to make this thing happen.

I am very grateful to Dr. Leif Toudal Pedersen for sharing his immense experience on everything which can possibly be related to ice in the Arctic, for the constructive feedback for my work in innumerable e-mail and Skype conversations and for examining my thesis as second reviewer.

My thesis committee was completed by Dr. Larysa Istomina and Dr. Frank Kauker. Larysa, thanks for sharing your knowledge on all the dos and don'ts when it comes to using visible and thermal infrared wavelengths. Frank, thanks for a modeler's view on remote sensing data and for the support during the publication of the polynya paper. I want to thank Prof. Dr. Monika Rhein, Prof. Dr. Claus Lämmerzahl, Dr. Christian Melsheimer and Malte Gerken for being part of my examination committee, and hope that you enjoyed the talk and the colloquium.

I would like to thank Dr. Thorsten Markus for having me as guest researcher at NASA's Goddard Space Flight Center, for the interest he showed in my work and for giving me a sneak preview on ICESat-2, and Dr. George Riggs for answering each and every one of my MODIS- and VIIRS-related questions.

The scientific, personal and emotional support of my „Remote Sensing of the Polar Regions“ colleagues is a supporting pillar in the building which I now call dissertation. Special thanks goes out to Dr. Christian Melsheimer for patiently answering all my minor and major ASI questions, to Dr. Marcus Huntemann for his aid in setting up the merged SIC operational processing and to my long-time office mates Philip and Dima for the nice time, the jokes and the coffee. Thanks to Alex, Arantxa, Christian, Christine, Hannah, Janna, Linda, Marcus, Philip, and Raul for proof-reading parts of my thesis.

Being an Associated PhD student at ArcTrain taught me that there are people who study the Arctic without satellites and made it possible to meet great and inspiring people on

both sides of the Atlantic. A special thanks goes out to Anouk for the nice time we had as speakers and the support in times of avalanches. For accepting me as an Associated PhD, and for the financial support for three trips to Canada and one to the AGU in New Orleans, I would like to thank the speaker's board, especially Prof. Dr. Michal Kucera. This research has been supported by a Junior Research Group in the framework of the Institutional Strategy of the University of Bremen (funded by the German Excellence Initiative) and by the Deutsche Forschungsgemeinschaft (grant no. GRK1904/ArcTrain), to both of whom I am grateful for the funding. The data provision by NSIDC, LAADS DAAC, JAXA, ECMWF, DMI, TU Denmark and OSI SAF is highly appreciated. The University of Michigan Press Ann Arbor and the American Geophysical Union and John Wiley & Sons, Inc. are gratefully acknowledged for granting me permission to use the Figures 2.2 and 2.3, respectively.

Furthermore, I would like to thank Peter Grupe, Malte Gerken and the IUP admins for keeping the soft- and hardware running smoothly and all the other technical support. Also, I am indebted to the anonymous crowd online. I never asked a question in any forum, but the only reason is that I always found the answer before.

Last, but certainly not least, I would like to thank my parents and family for making me who I am, Hannes, Yannick and the other wonderful friends I made since October 14, 1990 for the small and big things in life and Caro, for more than words can possibly say.